POLITECNICO DI MILANO

School of Industrial and Information Engineering

Master of Science in Space Engineering

DEVELOPMENT OF A COMPACT, LOW POWER TRAVELING MAGNETIC FIELD PLASMA ACCELERATOR

SUPERVISOR: Prof. Luigi De Luca (Politecnico di Milano)
EXTERNAL SUPERVISOR: Prof. Mark A. Cappelli (Stanford University)

Master Thesis of:
Simone FERABOLI 799146

Academic year 2014-2015

*It [the rocket] will free man from his remaining chains, the
chains of gravity which still tie him to this planet.
It will open to him the gates of heaven.*

Wernher von Braun, 'The Jupiter People', 1958.

Contents

CONTENTS

CONTENTS

List of Figures

List of Tables

LIST OF TABLES

Abstract

Abstract in Lingua Italiana

La propulsione al plasma senza elettrodi rappresenta uno tra i più promettenti sviluppi nel campo della propulsione elettrica, in quanto permettono di oltrepassare le limitazioni sulla vita operativa dei sistemi classici grazie al non utilizzo di componenti ad alto grado di usura quali sono gli elettrodi e griglie di accelerazione. Questo documento presenta il lavoro svolto per progettare e sviluppare un modello di prova di un sistema basato su un campo magnetico traslante, utilizzabile come stadio di accelerazione di un sistema propulsivo a doppio stadio se accoppiato a una sorgente di plasma. La teoria su cui tale sistema si basa viene mostrata tramite equazioni classiche, unite a una visione più recente per quanto riguarda l'interazione tra campo mangetico in movimento e plasma supportata da simulazioni numeriche. La fase di progetto mette in luce aspetti positivi e negativi delle diverse tecniche prese in considerazione per la generazione di un campo magnetico traslante, e presenta quale soluzione è statta considerata migliore per il nostro esperimento. Successivamente tale sistema è stato realizzato, e viene così presentata una descrizione dei vari componenti nonchè del principio di funzionamento. Sono state eseguite misurazioni con sonde di corrente e di campo magnetico per confermare che il sistema funzionasse correttamente e che generasse un campo magnetico in accordo con quanto previsto; sono poi seguite misure con sonde immerse in plasma per valutare la presenza di un'interazione tra il campo magnetico prodotto e il flusso di plasma. I risultati di tali test sono presentati e discussi. Abbiamo mostrato un accoppiamento tra plasma e campo magnetico, ma purtroppo non siamo stati in grado di confermare che tale fenomeno abbia l'effetto di un pistone magnetico, poichè misure di velocità si sono rivelate in disaccordo con quanto previsto e non affidabili. Sviluppi futuri dovrebbero interessare le tecniche di misurazione, in quanto sistemi di

ABSTRACT

test più avanzati e precisi potrebbero chiarire definitivamente tutti gli aspetti legati a questa nuova e promettente tecnologia di propulsione.

Parole chiave:
Plasma, Propulsione, Campo Magnetico Traslante, Impulso di Corrente, Stadio di Accelerazione

English Abstract

Electrodeless plasma propulsion devices represent a promising advancement in the field of electric propulsion, as they allow to overcome the main lifetime limitations of current technology by not implementing components heavily affected by erosion such as electrodes or acceleration grids. This report presents the work done to develop a proof-of-concept device based on traveling magnetic field, usable as acceleration stage of a dual-stage electrodeless propulsion system if coupled with a plasma source. The interaction between plasma and a traveling magnetic field is explained from a theoretical point of view, both thanks to a classical approach and both thanks to more recent theories supported by particle simulation results. The design phase is then presented, with a discussion of all the benefits and problems of different strategies studied to generate a traveling magnetic field. A proof-of-concept based on the selected technology has been built and a description of its characteristics has been presented, along with an explanation of how the system operated. Measurements with different probes in different operative conditions have then been performed. Current and magnetic field measurements were needed to determine the correct functioning of the accelerator, followed by Faraday probe and time-of-flight measurements to detect any interaction between plasma and magnetic field, and possibly to understand if such effect accelerated plasma. Results of all those tests have been presented and discussed. We have been able to determine that the traveling magnetic field generated coupled with the plasma flow, however we were not able to detect any acceleration phenomenon in accordance with our predictions. Implementation of different type of measurements could prove useful to provide a final assessment on this new and promising propulsion technique.

Keywords:
Plasma, Propulsion, Traveling Magnetic Field, Current Pulse, Acceleration Stage

ABSTRACT

Estratto della Tesi

Introduzione

Un importante ramo della propulsione spaziale è rappresentato dai sistemi di propulsione al plasma. Tali sistemi si basano sull'accelerazione di gas ionizato (plasma) per ottenere spinta.

I sistemi di propulsione al plasma presentano tipicamente una fonte di plasma, che permette la ionizzazione del propellente, e un sistema di accelerazione. Dato l'elevato I_{sp} che tali tecnologie riescono a raggiungere, la quantità di propellente impiegato è generalmente molto contenuta, e ciò garantisce un grande risparmio in termini di massa a bordo si sistemi spaziali; per questo motivo la propulsione al plasma è una tecnologia promettente (e in alcuni casi già utilizzata) in tutti quegli ambiti che richiedono una lunga vita operativa. In contrasto, tali sistemi non sono in grado di produrre livelli di spinta elevati, perciò il loro impiego è perlopiù confinato al controllo d'assetto.

Nonostante l'elevata longevità dei propulsori al plasma dal punto di vista del propellente, ci sono fattori molto più limitanti, quali l'erosione di elettrodi/-griglie di accelerazione e del canale di accelerazione; tali problematiche sono dovute alle collisioni tra particelle energetiche (sia ionizzate che neutre) e le pareti dei vari componenti, nonchè alle elevate temperature in gioco.

La volontà di aumentare ulteriormente la longevità dei propulsori e ridurre l'usura comporta che buona parte della ricerca sia volta allo sviluppo di sistemi di propulsione al plasma senza elettrodi; un ulteriore vantaggio di questo tipo di tecnologia, oltre all'aumento di longevità, è quello di poter eliminare un altro componente piuttosto problematico, il neutralizzatore (il catodo, nel caso degli Hall Thrusters), in quanto il propellente espulso è di persè neutro.

Varie tecnologie sono state studiate e proposte; un esempio è il Pulsed Inductive Thruster (PIT) [26]. Esso consiste in una bobina piana in cui scorre della corrente pulsata, ottenuta dalla scarica di condensatori; il gas viene

iniettato alla stessa frequenza degli impulsi di corrente e ionizato da un forte campo elettrico azimutale, mentre la formazione di una corrente azimutale nel plasma opposta a quella che scorre nella spirale contribuisce ad espellere il propellente. Altri sistemi più esotici sono stati proposti, ad esempio sistemi di propulsione basati su campo elettrico rotante [35]. In questo caso, il propellente viene accelerato dalla combinazione di un campo magnetico e un campo elettrico rotante.

Infine, un altra tecnica è stata studiata: l'accelerazione di plasma tramite campo magnetico traslante [31, 23, 37, 29, 28, 15]. Essa consiste in una serie di bobine in cui la corrente scorre con sfasamento progressivo in modo da produrre l'effetto di traslazione del campo magnetico. Vari sistemi sono stati studiati negli anni '60 e '70, ma tutti si basavano su acceleratori di grandi dimensioni e/o potenze in gioco molto elevate (centinaia di kW o addirittura MW).

L'obbiettivo di questo lavoro è quello di sviluppare un acceleratore di plasma basato sulla tecnologia del campo magnetico traslante che sia in grado di operare a bassa potenza e che abbia dimensioni contenute per ridurre al minimo le perdite dovute al contatto tra plasma e pareti dell'acceleratore.

In questa relazione viene dapprima proposta una base teorica riguardante l'interazione tra plasma e campo magnetico traslante, seguita da una breve descrizione della progettazione del sistema, e una descrizione del prototipo costruito noncè dei risultati ottenuti.

Teoria del Campo Magnetico Traslante

Al fine di descrivere le interazioni tra plasma e campo magnetico traslante possiamo considerare un modello 2D dell'acceleratore senza perdere di generalità. Nonostante alla base del nostro sistema c'è un campo magnetico assiale che tralsa, per l'illustrazione dei principi teorici possiamo considerare un sistema con campo magnetico radiale in movimento, in quanto le basi teoriche sono le stesse. La teoria qui di seguito descritta è stata elaborata da R.G. Jahn e riportata in un suo libro sulla fisica dei sistemi di propulsione elettrica [27].

Assumiamo la direzione z essere quella assiale (direzione di propagazione) e la direzione y quella radiale; consideriamo inoltre trascurabile il campo magnetico indotto nel plasma, e consideriamo costanti tutte le proprietà lungo la direzione x, perpendicolare alla direzione del campo magnetico e alla direzione di propagazione.

In tali condizioni il campo magnetico presenta solamente componenti lungo z e y , e deve soddisfare le equazioni:

$$\vec{\nabla} \times \vec{B} = 0 \tag{1}$$

$$\vec{\nabla} \cdot \vec{B} = 0 \tag{2}$$

Le condizioni al contorno di tale sistema derivano dalla simmetria lungo l'asse dell'acceleratore e dal fatto che stiamo considerando un campo sinusoidale; esse possono essere espresse come:

$$B_z(0, z, t) = 0 \tag{3}$$

$$B_y(0, z, t) = B_0 cos \frac{2\pi}{\lambda}(z - v_p t) \tag{4}$$

Al fine di semplificare le successive equazioni è possibile passare a un sistema di coordinate fisso semplicemente sostituendo la velocità di fase v_p con l'espressione:

$$v_r = v_p - u(z) \tag{5}$$

dove $u(z)$ è la velocità del flusso di plasma. Da ciò segue che le componenti del campo magnetico possono essere espresse come:

$$B_z = -B_0 sinh \frac{2\pi y}{\lambda} sin \frac{2\pi}{\lambda}(z - v_r t) \tag{6}$$

$$B_y = B_0 cosh \frac{2\pi y}{\lambda} cos \frac{2\pi}{\lambda}(z - v_r t) \tag{7}$$

Il campo elettrico indotto deve soddisfare l'equazione:

$$\vec{\nabla} \times \vec{E} = -\frac{\partial \vec{B}}{\partial t} \tag{8}$$

e nel nostro caso risulta essere:

$$E_z = E_y = 0 \tag{9}$$

$$E_x = B_0 v_r \cosh \frac{2\pi y}{\lambda} \cos \frac{2\pi}{\lambda}(z - v_r t) \tag{10}$$

La forza per unità di volume agente sul plasma è data da

$$\vec{f} = \vec{j} \times \vec{B} \tag{11}$$

ed essendo j nel nostro sistema di riferimento:

$$\vec{j} = \sigma \vec{E} \tag{12}$$

le componenti di tale forza risultano essere:

$$f_z = \sigma E_x B_y = \sigma B_0^2 v_r \cosh^2 \frac{2\pi y}{\lambda} \cos^2 \left[\frac{2\pi}{\lambda}(z - v_r t) \right] \tag{13}$$

$$f_y = -\sigma E_x B_z = \frac{\sigma B_0^2 v_r}{4} \sinh \frac{4\pi y}{\lambda} \sin \left[\frac{4\pi}{\lambda}(z - v_r t) \right] \tag{14}$$

È interessante notare come la forza assiale risulta essere sempre positiva; ciò deriva dal fatto che nonostante il campo magnetico cambi direzione, altrettanto fa la corrente azimutale e quindi l'azione è sempre quella di spingere il plasma verso l'uscita dell'acceleratore. Inoltre questa forza presenta intensità e frequenza variabili a seconda della velocità del plasma: assumendo un flusso di plasma inizialmente in quiete, la forza assiale presenta massima intensità e frequenza doppia di quella del campo magnetico. Man mano che la velocità u del plasma aumenta, entrambi i parametri calano fino all'annullamento della forza quando il plasma e il campo magnetico si muovono ad egual velocità. Questo ci fa capire un limite importante di questo tipo di sistema, ovvero che il flusso di plasma può essere accelerato fino a raggiungere la velocità di propagazione del campo magnetico e non oltre.
A seguito di simulazioni di traiettorie di ioni ed elettroni soggetti a campo magnetico traslante siamo stati in grado inoltre di dar credito a una più moderna teoria riguardante l'interazione tra campo magnetico e plasma, proposta da Lucca Fabbris e Cappelli. In un loro articolo [31] mostrano come l'accelerazione non avviene con il plasma che si comporta come un'unica

identità, ma piuttosto ioni ed elettroni subiscono l'azione del campo in modo diverso. In particolare, si può notare come il campo magnetico traslante inizialmente ha effetto solamente sugli elettroni spingendoli in direzione del della sua propagazione, mentre gli ioni rimangono imperturbati dato che la loro risposta cinetica è molto più lenta a causa della massa di svariati ordini di grandezza maggiore. Tale moto di elettroni crea una separazione di carica direttamente in fronte al campo magnetico, a cui si associa un campo elettrico che agisce in modo da rallentare gli elettroni ed accelerare gli ioni.

Progettazione e Realizzazione del Sistema di Accelerazione

Al fine di ottenere un campo magnetico in movimento possono essere impiegate diverse tecniche; una di queste si basa sull'utilizzo di una linea di trasmissione.

La linea di trasmissione può essere realizzata tramite una serie di induttori intervallati da condensatori in parallelo (seguendo lo schema a parametri concentrati), in modo da ottenere una corrente che viene progressivamente sfasata; progettando opportunamente questa variazione di fase è possibile ottenere complessivamente una traslazione del campo magnetico.

La progettazione di un tale sistema si basa sulla definizione e calcolo di alcuni parametri fondamentali, quali velocità di fase, frequenza del segnale, lunghezza d'onda, induttanza, capacità e impedenza. Equazioni che mettono in relazione tali parametri possono essere ricavate dalle equazioni d'onda della linea di trasmissione.

Possiamo esprimere la velocità di fase (ovvero la velocità di propagazione del campo magnetico) come:

$$v_p = \frac{1}{\sqrt{L'C'}} \tag{15}$$

Dove L' e C' sono l'induttanza e capacità per unità di lunghezza. Abbiamo poi la lunghezza d'onda, dipendente da velocità di fase e frequenza secondo la relazione

$$\lambda = \frac{v_p}{f} \tag{16}$$

Infine, l'impedenza caratteristica della linea può essere definita come:

$$Z_0 = \sqrt{\frac{L'}{C'}} \qquad (17)$$

Durante la progettazione alcuni parametri vanno imposti in modo da poter calcolare i restanti, e tale processo viene ripetuto più volte per ottenere una combinazione ottimale di valori.

Generalmente ci sono una serie di vincoli da dover rispettare e una serie di requisiti che si vogliono soddisfare nel limite del possibile. Ad esempio, la frequenza del segnale è solitamente imposta dal tipo di sorgente disponibile, quindi difficilmente si può giocare su tale valore. Inoltre, al fine di avere una linea di trasmissione adattata è necessario chiuderla con un'impedenza di valore pari all'impedenza caratteristica della linea, la quale dovrebbe essere il più possibile vicina al valore dell'impedenza dell'alimentatore in modo da evitarne una rottura dovuta a potenza riflessa. C'è poi il requisito sula geometria da rispettare (vorremmo che il rapporto tra lunghezza e diametro dell'acceleratore fosse contenuto), che si traduce nella necessità di utilizzare induttori multistrato, con le problematiche di induttanza reciproca da tenere sotto controllo.

In generale possiamo dire che questo sistema nonostante concettualmente sia semplice comporta una serie di complessità nella fase di progettazione dovuta all'accoppiamento dei vari parametri. Dopo numerosi tentativi atti a raggiungere un risultato ottimale è stato deciso di abbandonare tale sistema per via delle limitazioni che presenta; in particolare la problematica principale è relativa al basso livello di campo magnetico che può essere ottenuto in modalità continua (con una sorgente che opera in continuo). Infatti come detto in precedenza è necessario adattare l'impedenza della linea con quella dell'alimentatore, e ciò può essere ottenuto in due modi: imporre l'impedenza caratteristica uguale a quella dell'alimentatore o utilizzare un sistema di accoppiamento dell'impedenza. Nel primo caso, dato che l'impedenza della sorgente è tipicamente piuttosto alta (intorno a 50 Ω), la corrente che si è in grado di far scorrere nella linea è bassa ai livelli di potenza che l'alimentatore può fornire, e quindi si riesce ottenere un campo magnetico di soli pochi Gauss; nel secondo caso si potrebbe avere una linea con bassa impedenza dato che viene utilizzato un adattatore, ma per avere ciò bisognerebbe utilizzare induttori con bassa induttanza dato che l'impedenza dipende dal rapporto L/C, e quindi anche ad alta corrente il campo magnetico generato rimarrebbe basso.

Per questi motivi abbiamo cercato un sistema diverso di ottenere un campo magnetico traslante; una possibilità è quella di utilizzare una serie di circuiti RLC indipendenti, ciascuno alimentato da un proprio generatore. Così come per la linea di trasmissione anche in questo caso il sistema può operare in continuo o in modo pulsato, ma nel primo caso sarebbe necessario progettare dei generatori specifici per questo sistema (che devono produrre correnti con precise differenze di fase tra loro), cosa troppo complessa per i nostri scopi. Per questo motivo ci siamo concentrati su un sistema che opera con impulsi di corrente prodotti dalla scarica di condensatori.

I circuiti sono stati opportunamente progettati per ottenere un impulso di corrente, tramite le seguenti equazioni:

$$2\pi f = \frac{1}{\sqrt{LC}} \tag{18}$$

$$\zeta = \frac{R}{2}\sqrt{\frac{C}{L}} \tag{19}$$

Al termine di una serie di simulazioni eseguite con Matlab e Simulink siamo giunti alla seguente definizione dei parametri:

- L=0.6 µH

- f=1 MHz

- ζ=0.68

- C=0.0423 µF

- R=5 Ω

- V_{ch}=800 V

- f_{rep}=5 Hz

L'induttanza è stata ottenuta tramite l'avvolgimento di un filo magnetico di rame da 2 mm di diametro su due strati da due spire ciascuno, in modo da mantenere le dimensioni contenute. Il diametro interno è di 1 " e quello esterno di 1.18 ". Per quanto riguarda i condensatori abbiamo utilizzato due condensatori da 0.022 µF in parallelo per ciascun circuito; il voltaggio a cui sono caricati è stato scelto in quanto massimo valore che rispettasse i limiti dei

componenti più sensibili (con un certo margine di sicurezza). Le operazioni seguite per ottenere l'impulso di corrente sono le seguenti: i condensatori vengono caricati al voltaggio prestabilito, e una volta completamente carichi vengono staccati dal generatore aprendo dei relay montati ad ogni circuito. Non appena il generatore è stato staccato, degli interruttori vengono chiusi per ottenere la scarica. Gli interruttori utilizzati per questo scopo sono dei MOSFET, veloci e capaci di far scorrere l'elevata corrente prodotta. Essi vengono controllati da dei generatori d'impulso, grazie ai quali siamo in grado di stabilire il ritardo temporale tra due scariche successive e ottenere così la velocità di campo magnetico desiderata.

Essendo il sistema sviluppato un acceleratore di plasma, è necessario accoppiarlo a una sorgente di plasma al fine di poterlo sfruttare come sistema propulsivo. Per poter testare quanto sviluppato sono stati utilizzati due diversi tipi di sorgente di plasma: un propulsore helicon e una cavità risonante a microonde. Ciò è stato fatto per poter valutare eventuali differenze di prestazioni e differenze di interazione del campo magnetico traslante con plasma di diverse densità.

Per quanto riguarda i sistemi di misurazione, sono state utilizzate diverse sonde sia per poter valutare l'effettivo funzionamento del nostro sistema di circuiti sia per valutarne l'efficacia come acceleratore di plasma. Sono state utilizzate sonde di corrente, sonde di campo magnetico, e sonde di corrente di plasma.

Risultati

Per prima cosa si è rivelato necessario testare il corretto funzionamento dei circuiti sia singolarmente che assemblati nella configurazione finale. A tal fine abbiamo applicato sonde di corrente ai circuiti per valutare che l'impulso di corrente generato dalla scarica dei condensatori rispecchiasse quanto progettato. Da questo tipo di test abbiamo potuto valutare come l'impulso che i circuiti generano presenti le caratteristiche volute, anche se il picco di corrente risulta essere inferiore mentre l'ampiezza risulta maggiore rispetto a quella progettata. Il motivo di tali differenze è semplice: la fase di progettazione è stata effettuata in ambito ideale, in quanto non era possibile avere tutte le informazioni dei componenti reali. L'elemento importante è che qualitativamente l'impulso reale e quello ideale progettato differiscono minimamente, e questo dà la garanzia del corretto funzionamento del sistema; la riduzione di "prestazioni" era prevista già in fase di progetto. È stata in seguito verificata

la capacità di ottenere impulsi di corrente con qualsivoglia ritardo temporale, al fine di poter ottenere un ampio range di velocità di campo magnetico.

Successivamente abbiamo dovuto controllare che l'acceleratore producesse effettivamente un campo magnetico traslante. Per questo, abbiamo utilizzato le sonde di campo magnetico precedentemente realizzate. Abbiamo ricostruito il profilo spaziale del campo magnetico generato a diversi istanti di tempo e lo abbiamo paragonato a simulazioni precedentemente effettuate; in questo modo siamo stati in grado di verificare non solo che il campo effettivamente traslasse, ma anche che il suo profilo fosse in accordo con quanto ci si potesse aspettare.

Sono stati poi effettuati una serie di test con campo magnetico a diverse velocità, in modo da verificare che la velocità effettiva del campo magnetico fosse pari a quella calcolabile dal ritardo di tempo impostato tramite i generatori di impulsi.

Tutte le precedenti misure sono state effettuate senza flusso di plasma. Essendo sicuri che l'acceleratore funzionasse come previsto, siamo quindi passati ad effettuare test in presenza di plasma.

Abbiamo subito potuto notare come ogni qualvolta l'acceleratore venisse acceso in presenza di plasma quest'ultimo iniziasse a pulsare, con istanti di maggior intensità alternati ad istanti di affievolimento. Essendoci sembrato piuttosto interessante ne abbiamo catturato un video e abbiamo valutato i singoli fotogrammi, da cui si è rivelato come queste pulsazioni del flusso di plasma avessero frequenza pari a quella operativa dell'acceleratore. Tale risultato, anche se promettente, non ci permette minimamente di stabilire se l'effetto osservato fosse o meno quello di un pistone magnetico in quanto puramente qualitativo.

Per ottenere misure quantitative abbiamo innanzitutto valutato la corrente di plasma tramite misure con una Faraday probe. Tali misure sono state effettuate sia su lungo periodo (20 s) che su breve periodo (nell'ordine di ms). Nel primo caso, abbiamo cercato la presenza di frequenze riconducibili alla frequenza di ripetizione delle scariche dell'acceleratore tramite trasformata di Fourier del segnale. Abbiamo così potuto osservare come soltanto quando il campo magnetico viene prodotto in presenza di plasma tali frequenze compongono il segnale proveniente dalla sonda. Grazie ad acquisizioni su corto periodo siamo stati in grado di osservare un'interazione tra plasma e campo magnetico ma alcune problematiche non hanno permesso di valutare la velocità del flusso di plasma a seguito di tale fenomeno.

Abbiamo così cercato di ovviare a tali problematiche effettuando misure con una sonda in grado di misurare il tempo di volo del plasma. Abbiamo applicato questa tecnica in diverse condizioni operative; in particolare, abbiamo effettuato misure con entrambe le sorgenti di plasma, a diverse portate di

massa di propellente, a diversi voltaggi a cui i condensatori sono caricati, a diversi livelli di potenza delle sorgenti, e a diverse velocità di campo magnetico.

Il cambiamento di sorgente di plasma non ha grandi effetti sulle misurazioni del tempo di volo, sennonchè il propulsore helicon genera una maggior quantità di rumore per via del sistema di generazione di potenza ad esso associato. Sia al variare di potenza della sorgente di plasma che al variare del voltaggio a cui i condensatori vengono caricati l'effetto principale è quelli di un semplice cambiamento dell'intensità del segnale prodotto dalla sonda; ciò è spiegabile col fatto che tali parametri regolano l'intensità del plasma o del campo magnetico, perciò variando uno dei due si modifica il livello di corrente indotto negli elettrodi che compongono la sonda. Una peculiarità delle misure effettuate è la presenza di due picchi di corrente, il primo dei quali presenta una più elevata componente di rumore elettromagnetico (nel caso delle misure con propulsore a helicon il primo picco risulta del tutto dovuto a rumore elettromagnetico). È interessante notare come al variare della portata massica di propellente la distanza temporale tra tali picchi cambia, e in particolare riducendo la portata massica i picchi si avvicinano fino ad unirsi in un unico picco per valori sufficientemente bassi di flusso di propellente.

La variazione di velocità del campo magnetico invece agisce su un picco di corrente modificandone l'ampiezza, che aumenta al diminuire della velocità, in accordo col fatto che il tempo necessario ad ottenere una scarica completa aumenta e quindi l'interazione potrebbe avvenire con una maggior quantità di plasma dato che esso scorre continuamente.

Da notare inoltre come tutti questi effetti sono presenti solamente nel caso in cui l'acceleratore operi in presenza di plasma; ciò è molto importante, in quanto ci permette di stabilire che quanto osservato non è semplicemente dovuto a interferenza elettromagnetica.

Purtroppo, nonostante siamo riusciti ad osservare un'interazione tra plasma e campo magnetico traslante, le misure a nostra disposizione non hanno reso possibile determinare quale tipo di interazione essa sia; più precisamente, non siamo stati in grado di stabilire se il campo magnetico agisse effettivamente come un pistone in grado di accelerare il plasma, poichè le misure di velocità del flusso di plasma non si sono rivelate sufficientemente accurate. Problematiche relative a effetti capacitivi dei cavi di collegamento tra strumentazione e oscilloscopio potrebbero aver causato misurazioni non accurate per quanto riguarda la scala temporale (il tempo di risposta del sistema di misurazione potrebbe essere stato troppo lungo per misurare fenomeni così veloci come quelli ottenuti col nostro esperimento).

Conclusioni

In questo report è stato presentato il lavoro svolto al fine di progettare e realizzare un sistema di propulsione al plasma basato su campo magnetico traslante. Siamo stati in grado di soddisfare i vincoli riguardanti le dimensioni dell'acceleratore (3.5 cm di lunghezza e 2.54 cm di diametro interno) e la potenza richiesta per il funzionamento (circa 1 W a una frequenza di ripetizione di 10 Hz). Abbiamo inoltre osservato un'interazione tra il flusso di plasma e il campo magnetico generato, ma come accennato non è stato possibile determinare se tale interazione producesse effettivamente un effetto di pistone magnetico, fenomeno sul quale teoricamente si basa il funzionamento del sistema. Per questo motivo eventuali sviluppi futuri dovrebbero essere basati sull'impiego di diverse tecniche di misura (come LIF, analizzatori di energia, o sonde di campo magnetico immerse nel plasma) per cercare di caratterizzare completamente il fenomeno osservato.

Acknowledgments
Ringraziamenti

Eccomi qui, al termine di questa esperienza universitaria, a fare il punto della situazione.
È stato un lungo percorso, e le persone a cui devo dei ringraziamenti sono tante.

Il primo va certamente ai miei genitori, Enrica e Doriano. Siete sempre stati al mio fianco, supportando ogni mia decisione e aiutandomi in ogni modo. Tutte le esperienze che ho fatto sono state possibili grazie al vostro appoggio, grazie al quale mi sono sentito sicuro in ogni situazione. Forse un semplice grazie non è sufficiente, ma non trovo altre parole per descrivere quanto fondamentali siete stati in questi anni.
Un altro ringraziamento va ai miei nonni, che mi hanno aiutato a crescere e a modellare la persona che sono oggi.
Un grazie anche a tutti i miei altri parenti, zii e cugini, senza i quali la famiglia non sarebbe completa.
Sicuramente un ringraziamento va anche ai nuovi membri della famiglia, i miei "cognati" Sara ed Enris, con i quali da ormai tre anni adoro trascorrere del tempo; i miei "suoceri" Angela e Franco, e tutte le splendide persone che ho avuto il piacere di conoscere in questi anni. Avervi al mio fianco rende tutto ancora più straordinario.

Altri sentiti ringraziamenti vanno ai miei amici, e in particolare a due di questi: Andrea e Fabio. Pensare di conoscere una persona i primi giorni di asilo e creare un legame di amicizia così forte da mantenersi intatto per oltre 20 anni può sembrare assurdo, eppure avere un amico come Andrea ha fatto

si che tutto questo tempo sia passato nel migliore dei modi. Per non parlare di Fabio, una delle persone più allegre e solari che io abbia mai conosciuto. È stato fantastico aver condiviso moltissime esperienze con voi.

Ci sono poi tutti i miei compagni e amici del Politecnico, a partire da quelli storici come Marco, Andrea ed Ezio, conosciuti i primi giorni del primo anno e rimasti insieme fino all'ultimo giorno del quinto, e tutti quelli aggiuntisi col passare del tempo. Abbiamo condiviso gioie e dolori di questi anni, e avendo reso le giornate piene di lezioni pesantissime molto più sopportabili mi avete aiutato ad arrivare in fondo a questo percorso con tranquillità.

A special thank you goes to all the people I've met during my experiences abroad. Thanks to all the people I met at the University of Minnesota, who made that year unforgettable. Thanks also to everyone from Stanford University, to my labmates in particular, always willing to help when I asked.
Un profondo ringraziamento va ad Andrea (si, un altro), fonte di grande esperienza e conoscenza, grazie al quale sono riuscito a portare a termine il lavoro a Stanford, e con cui spendere ore in laboratorio, e non solo, è stato un piacere.

Un sentito ringraziamento va al Professor De Luca, per avermi seguito come relatore e per avermi dato la possibilità di vivere questa esperienza di tesi in un'università estera.
I also want to deeply thank Professor Mark Cappelli for the opportunity he gave me to work in one of the most prestigious university in the world, and for being a great guide and a great person.

L'ultimo ringraziamento va alla persona più speciale di tutte: la mia ragazza, Veronica. Grazie, perchè sei sempre al mio fianco e perchè mi supporti sempre nelle mie decisioni, anche quelle più difficili. Avere una persona con cui condividere la propria vita non fa altro che renderla migliore. Non ho idea di cosa aspettarmi dal futuro, ma mi conforta sapere di condividerlo con te.

<div align="right">

Simone Feraboli
Luglio 2015

</div>

xxx

Chapter 1

Introduction

1.1 Background

Electric propulsion is a field of Space Propulsion that is based on transfering energy to an expellant in ways that are related to electrical power. The big advantage of this kind of technology is the high specific impulse that can be achieved, resulting in a drastic reduction of propellant mass that has to be carried on board of a spacecraft; the downside however, is that electric propulsion systems are not able to generate high thrust levels, which means they are typically implemented in missions that require low thrust for long periods of time, such as drag compensation, station keeping, etc.

One family of electric propulsion devices is represented by Plasma Propulsion Systems. Those systems use ionized gas (i.e. plasma) as the propellant that is accelerated to produce thrust. Some plasma thrusters provide both ionization and acceleration of propellant with a single system, while others consist in a plasma source, where a gas is injected and ionized to produce plasma, and an acceleration stage, which is designed to accelerate the plasma coming from the source.

As said before, the standard electric propulsion systems (Hall thrusters or gridded ion thrusters for example) require little amounts of propellant to operate, meaning that they are the preferred propulsion technology when it comes to long time operations.

1.2   Motivation

The lifetime of electric propulsion systems does not only depend on the propellant consumption, but also from a much more limiting factor, that is the erosion of electrodes, plasma channel, and acceleration grids (if present). That phenomenon is mainly due to the interaction between energetic particles (ions) and the walls of the thruster and the high temperature to which the thruster materials are subject to.

That is the main reason why a lot of emphasis has been put in developing electrodeless propulsion systems. Not relying on electrodes to accelerate the propellant can boost significantly the lifetime of a thruster; an added bonus to this technology is that the flow of propellant expelled is neutral, so no neutralizer is required, thus meaning another problematic component can be neglected (typically the cathode is one of the most critical components in Hall thrusters).

One example of electrodeless thruster is the Pulsed Inductive Thruster (PIT). It mainly consists of a flat spiral coil, with pulsed current flowing through it; the current is typically generated by discharging a bank of capacitors. Gas is injected in the thruster in pulses at the same time that the current pulse flows in the coil. The increasing current generates a strong azimuthal electric field that ionizes the gas and induces an azimuthal current in the plasma itself. The current in the plasma and the one in the coil flow in opposite direction, creating a repulsive force that blows the plasma out of the thruster. Specific impulses of over 2000s and efficiencies around 50% have been obtained with this kind of thruster [26].

Other more exotic solutions have been proposed, such as and electrodeless thruster based on a rotating electric field [35]. In this case the superposition of a rotating electric field and a magnetic field (both axial and radial) is exploited to accelerate the propellant. Plasma produced in a source stage is injected into the thruster and gets an induced rotational motion due to the rotating electric field and the axial magnetic field applied; this rotating motion generates an azimuthal current in the plasma, which interacts with the radial component of the magnetic field to push the propellant flow downstream.

There is then another concept that has been proposed, and that is an electrodeless thruster based on an axially traveling magnetic field. This technology is typically used to develop the acceleration stage of a plasma thruster, meaning that there is still the need for a plasma source upstream. The configuration is that of a series of coils with phase shifted current to generate a magnetic field that propagates from one end of the accelerator to the other.

The magnetic field interacts with the plasma by pushing it downstream, in the same fashion as a piston pushes a fluid out of a channel (that is why that phenomenon is often referred to as magnetic piston). Multiple studies have been carried out in the '60s and '70s about accelerating plasma with a propagating magnetic field, and it has proven to be a successful way to achieve the acceleration [31, 23, 37, 29, 28, 15]. Most studies however rely on huge amounts of power to produce high enough level of current in the coils to generate strong magnetic field in the accelerator channel. In multiple cases the efficiency was very low, negatively affected by the lossy interactions between the plasma and the channel walls.

1.3 Objectives

The objective of this work is to design a traveling magnetic field accelerator that does not require large amounts of power to be operated and with a geometry aimed at reducing the wall losses as much as possible. We then built a system with the goal of respecting those constraints, and performed multiple tests do determine whether we could achieve an interaction between the produced magnetic field and a plasma flow and to check if a magnetic piston effect could be witnessed.

1.4 Thesis Outline

This thesis is organized as follows. A theoretical background of the experiment is presented in Chapter 2; in particular, at first we look at the classical theory behind the traveling magnetic field accelerator, followed by the results of a series of numerical simulations in support to a more recently proposed theory that tries to explain the interaction between the traveling magnetic field and plasma. Then, in Chapter 3 we discuss two different paths that we took into consideration for the design of the accelerator. The design principles are described, along with benefits and drawbacks of both techniques. We also point out which of them we chose, and in Chapter 4 we discuss the result of the design phase together with a description of all the components used in building the system and all the instruments needed. The principles

of operation of the proof-of-concept are also presented. In chapter 5 we then present and discuss all the results of the test campaing performed. Finally, we draw some conclusion and we point out possible future developments.

Chapter 2

Traveling Magnetic Field Theory

2.1   Introduction

This chapter will provide a brief overview of the theory behind the interaction between a traveling magnetic field and plasma, which is the phenomenon on which Traveling Magnetic Wave Accelerators are based on. We first present a more classical theoretical analysis, as presented by Jahn in his book [27], followed by an analysis of the trajectories of charged particles, to dig deeper in the plasma-traveling magnetic field interaction.

2.2   Traveling Magnetic Field

The theory presented in this section comes from a book of R.G. Jahn on the physics of electric propulsion systems [27].
In order to describe how plasma is accelerated by a traveling magnetic field, we can assume a 2D model of the accelerator as shown in Figure 2.1.
The 2D approximation simply reduces the complexity of the mathematical expression, allowing the explanation of the basics of the phenomenon with relatively simple equations.
As from Figure 2.1, let's assume a system generating a nearly transverse
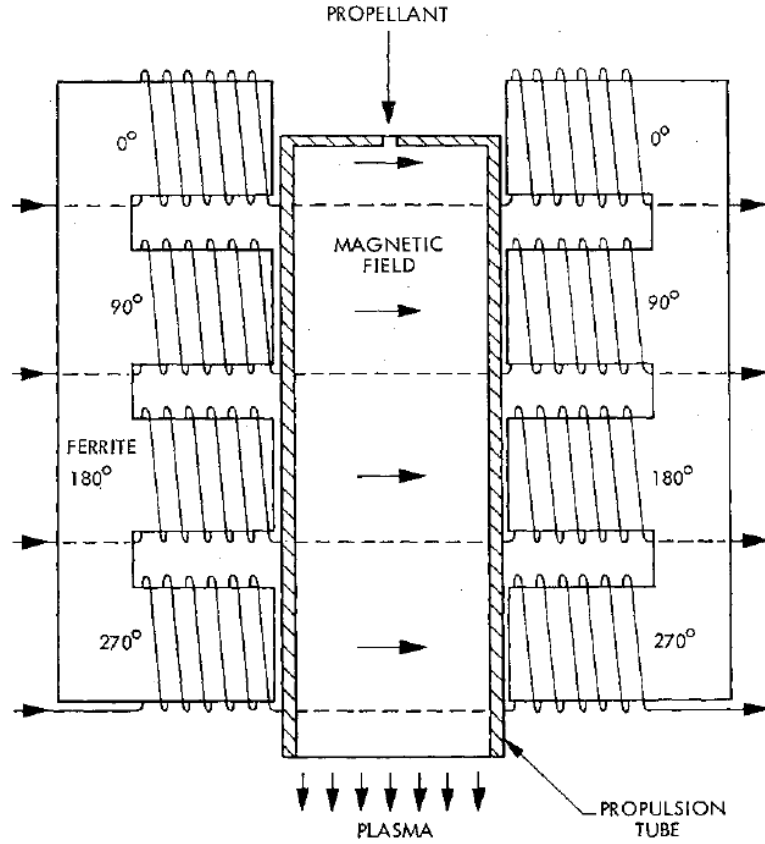
Figure 2.1: 2D Schematic of a Traveling Magnetic Field Plasma Accelerator [23]

magnetic field traveling along the axis of the channel, in the z-direction. Anoter assumption that can be made is that the gas has a uniform conductivity σ, and that it is small enough so that the induced magnetic field is negligible with respect to the applied magnetic field. Last assumption to make is to consider all the properties constant along the direction perpendicular to both magnetic field and phase velocity, the x-direction. With those assumptions in mind, the magnetic field will only have then 2 components:

$$\vec{B} = B_y(y, z, t)\hat{y} + B_z(y, z, t)\hat{z} \tag{2.1}$$

The magnetic field must satisfy the two equations:

$$\vec{\nabla} \times \vec{B} = 0 \tag{2.2}$$

$$\vec{\nabla} \cdot \vec{B} = 0 \tag{2.3}$$

Those can also be expressed, for this particular case, as:

$$\frac{\partial B_y}{\partial z} = \frac{\partial B_z}{\partial y} \tag{2.4}$$

$$\frac{\partial B_y}{\partial y} = -\frac{\partial B_z}{\partial z} \tag{2.5}$$

There are then two boundary conditions, one coming from the simmetry at the centerline and one from the fact that we are considering a sinusoidal wave, and those can be expressed as follows:

$$B_z(0, z, t) = 0 \tag{2.6}$$

$$B_y(0, z, t) = B_0 cos\frac{2\pi}{\lambda}(z - v_p t) \tag{2.7}$$

At this point, in order to keep simple expressions a common step is to move to a coordinate system fixed to the channel wall. To do that we just need to replace the phase velocity v_p with the slip velocity v_r given by:

$$v_r = v_p - u(z) \tag{2.8}$$

where $u(z)$ is the velocity of the gas flow.
That set of equations yields the following expressions for the components of the magnetic field:

$$B_z = -B_0 sinh\frac{2\pi y}{\lambda} sin\frac{2\pi}{\lambda}(z - v_r t) \tag{2.9}$$

$$B_y = B_0 cosh\frac{2\pi y}{\lambda} cos\frac{2\pi}{\lambda}(z - v_r t) \tag{2.10}$$

The induced electric field must follow the equation:

$$\vec{\nabla} \times \vec{E} = -\frac{\partial \vec{B}}{\partial t} \qquad (2.11)$$

Which for our system yields the following:

$$E_z = E_y = 0 \qquad (2.12)$$

$$E_x = B_0 v_r cosh \frac{2\pi y}{\lambda} cos \frac{2\pi}{\lambda}(z - v_r t) \qquad (2.13)$$

The force per unit volume accelerating the plasma is simply:

$$\vec{f} = \vec{j} \times \vec{B} \qquad (2.14)$$

And being j in our reference system:

$$\vec{j} = \sigma \vec{E} \qquad (2.15)$$

The result is that the components of the accelerating force per unit volume are:

$$f_z = \sigma E_x B_y = \sigma B_0{}^2 v_r cosh^2 \frac{2\pi y}{\lambda} cos^2 \left[\frac{2\pi}{\lambda}(z - v_r t)\right] \qquad (2.16)$$

$$f_y = -\sigma E_x B_z = \frac{\sigma B_0{}^2 v_r}{4} sinh \frac{4\pi y}{\lambda} sin \left[\frac{4\pi}{\lambda}(z - v_r t)\right] \qquad (2.17)$$

Those two force components have some peculiarities which can be seen from the equations themselves, however a graphical representation can show them in a more immediate way. Figure 2.2 and 2.3 show comparisons between axial and radial force components with the magnetic field. Moreover, Figure 2.4 shows the pattern of the accelerating force at different stages of the acceleration process.

What is interesting to note is that the accelerating force (the axial one) has always a positive sign, meaning it is always directed downstream, thus always accelerating the plasma and interacting with it at a frequency that is twice the one of the imposed magnetic field. This comes from the fact that
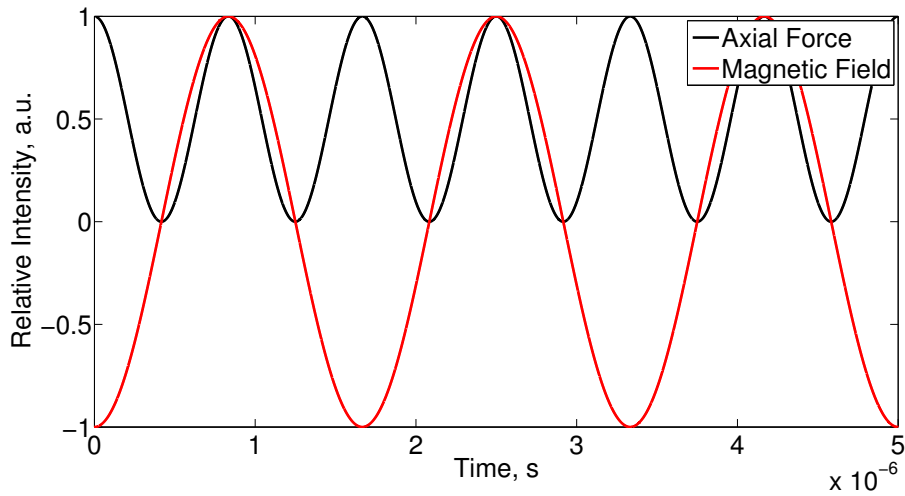
Figure 2.2: Comparison Between Axial Force and Magnetic Field
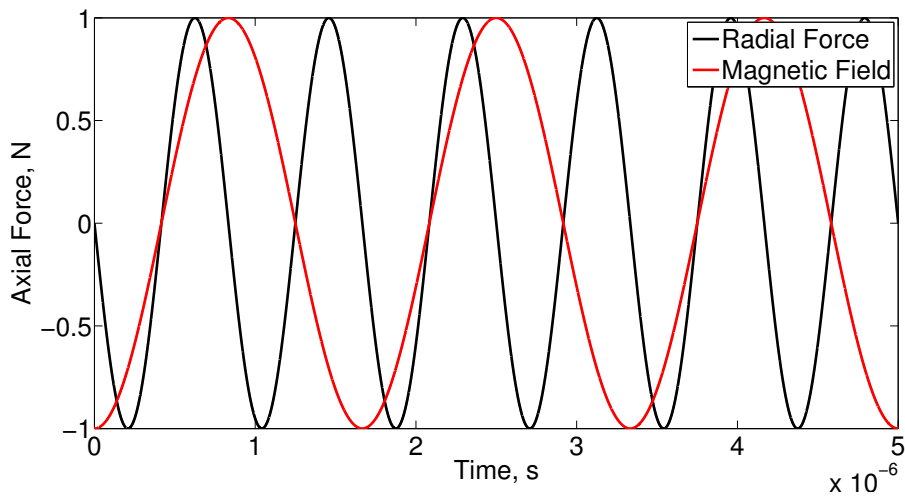
Figure 2.3: Comparison Between Radial Force and Magnetic Field

both the magnetic field generated by the system and the azimuthal current induced in the plasma change sign every half period of the magnetic field, and that results in an axial force always acting in the same direction.

Another interesting aspect of this accelerating force is that its frequency and magnitude depend on the velocity of the plasma flow: at the beginning of the acceleration stage, assuming for simplicity that the plasma is at rest, the accelerating force is at its maximum magnitude and at its highest frequency;

9
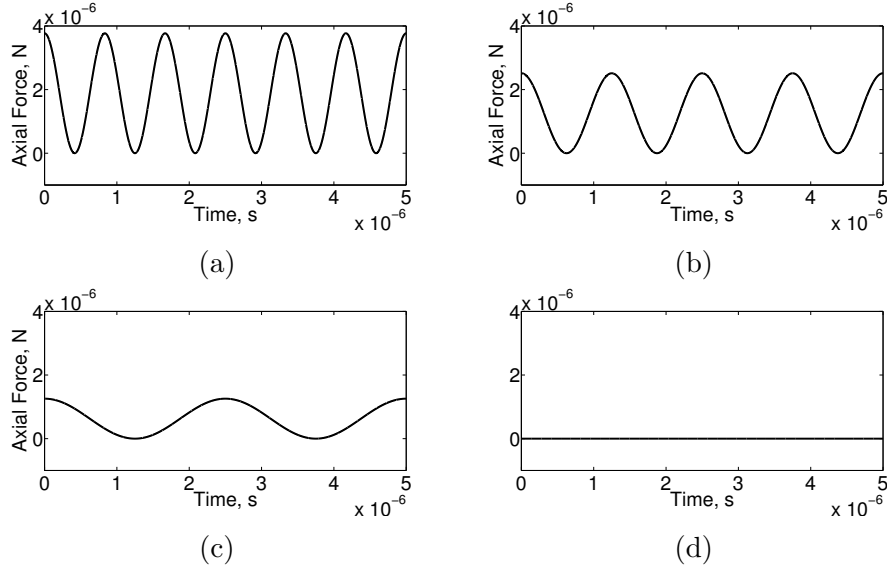
Figure 2.4: Axial force at different plasma velocities: a) u = 0 v_p, b) u = $v_p/3$, c) u = $2v_p/3$, d) u = v_p.

as the plasma is accelerated and its velocity u grows, both frequency and magnitude of the force decrease, until it vanishes once the plasma velocity equals the phase velocity and the acceleration is complete.

This tells an important thing: by setting the phase velocity of the traveling magnetic field we are setting the maximum speed that the plasma flow can reach at the exit of the accelerator.

For what concerns the radial force, it still operates at twice the frequency of the imposed magnetic field, however it changes sign, meaning that it changes between inward and outward directions.

As Jahn points out, it is not so simple to determine wheter it has positive or negative effects on the acceleration. Also, this force can have two opposite effects on the plasma flow: when it acts as an inward component it operates as a confining force, preventing the plasma to hit the accelerator walls and thus reducing the losses associated to that interaction; when insted it acts as an outward force, interaction between the plasma flow and the walls will be increased, and thus most of the energy may be lost in wall heating. In order to limit this kind of losses it would be good to reduce the total length of the accelerator, so that the surface wall that the plasma can hit is reduced.

Another important aspect is related to the efficiency of a traveling magnetic field plasma accelerator. At first let's assume a system based on a constant phase velocity and let's define the dynamical efficiency as the ratio between the kinetic energy variation of the plasma and the work performed on it:

10

$$\eta_d = \frac{\Delta T}{W} \tag{2.18}$$

The expression for the kinetic energy and the work done are as follows:

$$\Delta T = \frac{1}{2}\dot{m}\tau(u_f^2 - u_i^2) \tag{2.19}$$

$$W = \int_0^\tau F(t)v_p dt = v_p\dot{m}\tau(u_f - u_i) \tag{2.20}$$

Thus yielding:

$$\eta_d = \frac{\frac{1}{2}\dot{m}\tau(u_f^2 - u_i^2)}{v_p\dot{m}\tau(u_f - u_i)} = \frac{1 + \frac{u_i}{u_f}}{\frac{2v_p}{u_f}} \tag{2.21}$$

Looking at that expression, we can see how there is an upper bound for the efficiency: assuming a negligible initial velocity of the plasma flow the maximum attainable efficiency is 50%. The losses are mostly due to Joule heating that arise mainly due to the great difference between the flow velocity and the phase velocity at the beginning of the acceleration stage.

It is important to note that this kind of limitation comes from the assumption of constant phase velocity. One way to shift the maximum efficiency towards higher value would be to reduce the velocity mismatch at the beginning of the acceleration, which is possible in the case of a variable velocity traveling magnetic field. In this case we try to match the phase velocity with the flow velocity, thus having some sort of intermediate steps of complete acceleration, which increase the amount of energy (or work) that we can transfer to the plasma.

In this case the efficiency becomes:

$$\eta_d = \frac{1 + \frac{u_i}{u_f}}{1 + \frac{2v_p}{u_f} + \frac{u_i}{u_f}} \tag{2.22}$$

As mentioned in [27], matching field and plasma velocities to 10% of u_f throughout the channel leads to an increase in the maximum efficiency, that reaches about 80%.

2.3   Particle Motion Simulation

In order to have a better understanding of the interaction between plasma and a traveling magnetic field, simulations of the trajectories of both electrons and ions have been performed. In order to do that a code has been developed to simulate the magnetic and electric field within the accelerator, and such fields have been implemented in the equations of motion we had to solve to determine the trajectory of the particles we are interesten in. We made an assumption on the magnetic and electric field, that is to set to zero all the components negligible for this analysis; from that, the fields can be expressed in cylindrical coordinates as $\vec{B} = [\, B_r \; 0 \; B_z \,]$ and $\vec{E} = [\, 0 \; E_\theta \; 0 \,]$. For what concerns the magnetic field, we used the formulation with elliptic integrals derived from [42] in order to determine all the components:

$$B_r = \frac{\mu_0 I}{2\pi r} z \sqrt{(r+a)^2 + z^2} \left(-K\left(k^2\right) + E\left(k^2\right) \frac{r^2 + a^2 + z^2}{(r-a)^2 + z^2} \right) \qquad (2.23)$$

$$B_z = \frac{\mu_0 I}{2\pi} \sqrt{(r+a)^2 + z^2} \left(K\left(k^2\right) - E\left(k^2\right) \frac{r^2 - a^2 + z^2}{(r-a)^2 + z^2} \right) \qquad (2.24)$$

$$B_\theta = 0 \qquad (2.25)$$

Where a is the radius of the loop of wire, while K(k) and E(k) are the complete elliptic integrals of the first and second kind respectively, defined as:

$$K\left(k^2\right) = \int_0^1 \left[\left(1 - t^2\right)\left(1 - k^2 t^2\right)\right]^{-\frac{1}{2}} dt \qquad (2.26)$$

$$E\left(k^2\right) = \int_0^1 \left(1 - t^2\right)^{-\frac{1}{2}} \left(1 - k^2 t^2\right)^{\frac{1}{2}} dt \qquad (2.27)$$

And the argument k^2 of such integrals is defined as:

$$k^2 = \frac{4ar}{(r+a)^2 + z^2} \qquad (2.28)$$
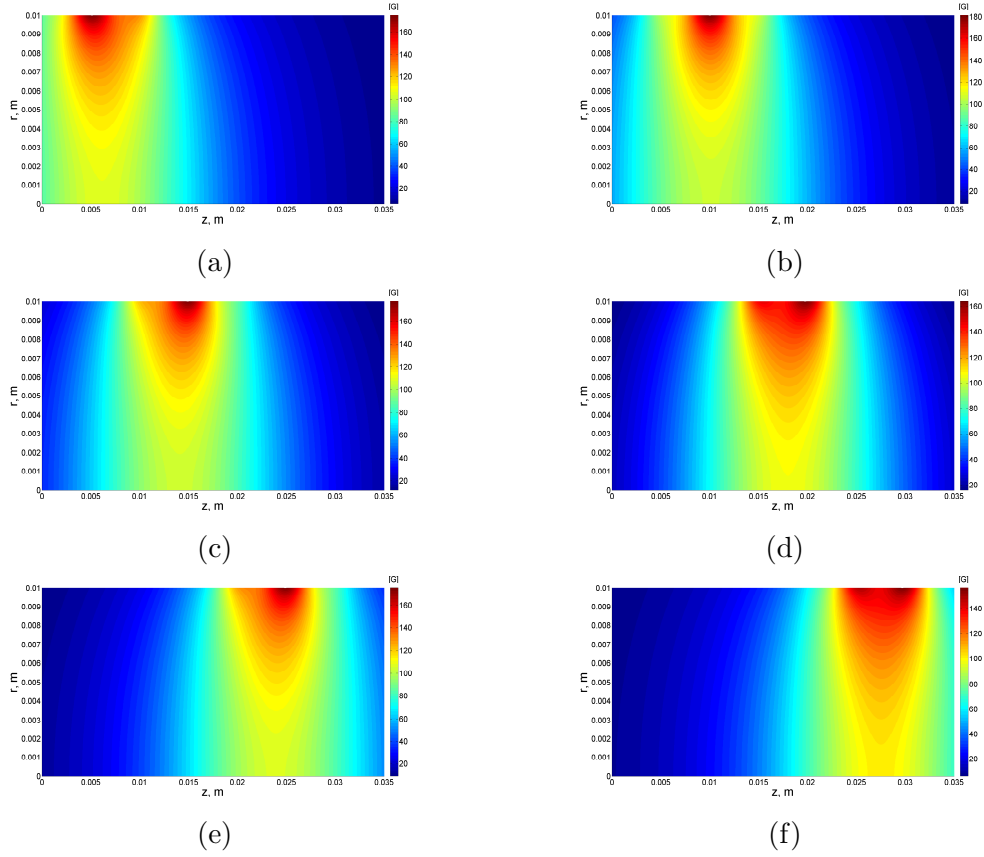
Figure 2.5: Example 2D magnetic field simulation at different time instants: a) t_0, b) $t_0 + 0.3$ µs, c) $t_0 + 0.7$ µs, d) $t_0 + 1.1$ µs, e) $t_0 + 1.6$ µs, f) $t_0 + 1.9$ µs.

The computation of the electric field comes directly after the one of the magnetic field by solving Faraday's law:

$$\vec{\nabla} \times \vec{E} = -\frac{\partial \vec{B}}{\partial t} \tag{2.29}$$

Which after our assumptions becomes just:

$$\frac{\partial E_\theta}{\partial r} = -\frac{\partial B_z}{\partial t} \tag{2.30}$$

That equation has been solved by means of a central-finite-difference method.

13
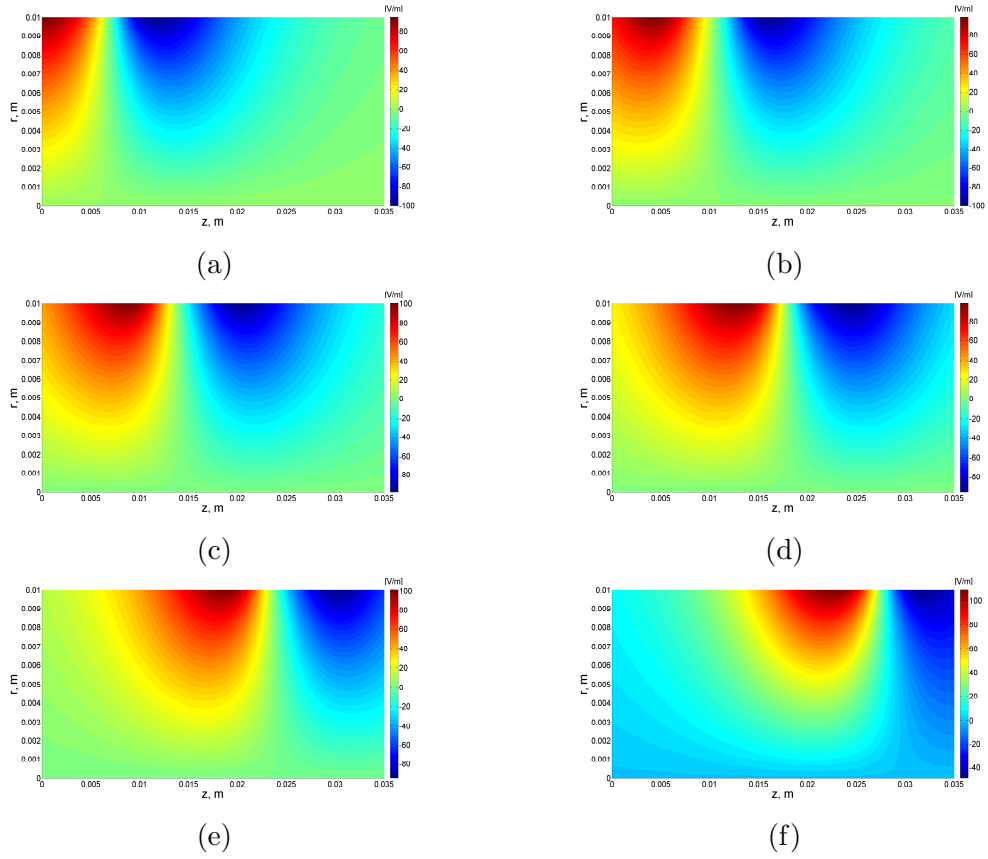
Figure 2.6: Example 2D electric field simulation at different time instants: a) t_0, b) $t_0 + 0.3$ µs, c) $t_0 + 0.7$ µs, d) $t_0 + 1.1$ µs, e) $t_0 + 1.6$ µs, f) $t_0 + 1.9$ µs.

In order to find the trajectory then we had to solve the equations of motion, coming from Lorentz law:

$$\vec{f} = q \left(\vec{E} + \vec{v} \times \vec{B} \right) \tag{2.31}$$

Which can also be written as:

$$\frac{d\vec{v}}{dt} = \frac{q}{m} \left(\vec{E} + \vec{v} \times \vec{B} \right) \tag{2.32}$$

For our system, the equations to solve are:

14

$$\frac{d^2r}{dt^2} = r\left(\frac{d\theta}{dt}\right)^2 + \frac{q}{m}\left(r\frac{d\theta}{dt}B_z\right) \tag{2.33}$$

$$r\frac{d^2\theta}{dt^2} = \frac{q}{m}\left[E_\theta + \left(\frac{dz}{dt}B_r - \frac{dr}{dt}B_z\right)\right] - 2\frac{dr}{dt}\frac{d\theta}{dt} \tag{2.34}$$

$$\frac{d^2z}{dt^2} = -\frac{q}{m}r\frac{d\theta}{dt}B_r \tag{2.35}$$

Those equations have been solved using a Runge-Kutta method. In order to determine whether our code was yielding realistic results we validated it against analytical solutions of standard single particle motions, such as the motion of a charged particle under uniform magnetic field. The resulting trajectory should be a circular motion on a plane perpendicular to the direction of the uniform magnetic field (in case the particle has a velocity component parallel to the magnetic field, that remains constant and the circular motion propagates in that direction) with a radius and frequency equal to the Larmor radius and cyclotron frequency respectively. Those quantities are defined as [12]:

$$r_L = \frac{mv_\perp}{|q|\,B} \tag{2.36}$$

$$\omega_c = \frac{|q|\,B}{m} \tag{2.37}$$

Where m is the mass of the particle, q its charge and $v_\perp$ the velocity component perpendicular to the magnetic field B. The simulation was done on an argon ion with the following parameters:

- $m = 6.64 \times 10^{-26}$ kg

- $q = 1.6 \times 10^{-19}$ C

- $B_x = 0$; $B_y = 0$; $B_z = 100$ G

- $v_x = 1$ m/s; $v_y = 0$; $v_z = 1000$ m/s

Plugging those values in equations 2.36 and 2.37 we obtain $r_L = 4.15 \times 10^{-5}$ m and $\omega_c = 24.09 \times 10^6$ rad/s. The results coming from the simulation are presented in Figures 2.7 and 2.8.
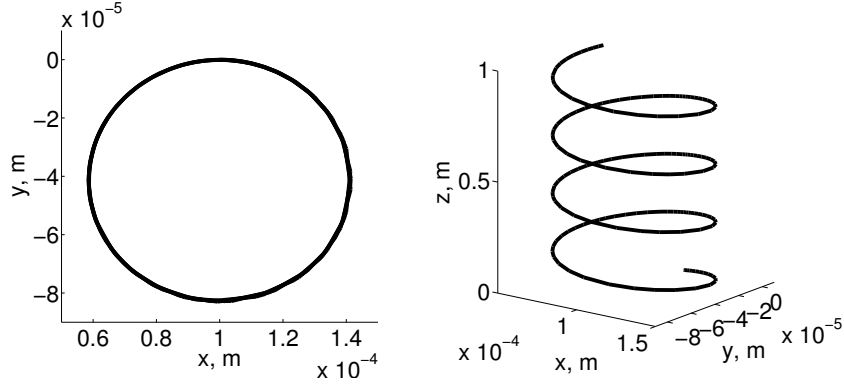
Figure 2.7: Ion trajectory under uniform magnetic field.
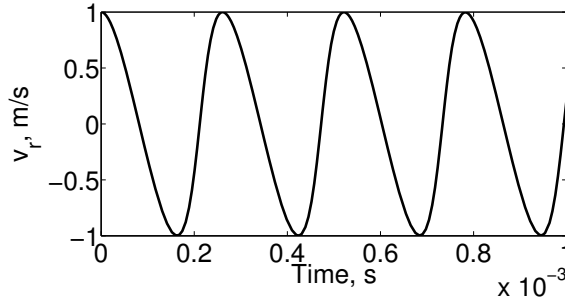
Figure 2.8: Ion radial velocity under uniform magnetic field.

Looking at the circular motion we can compute its radius, which turns out to be 4.142×10^{-5} m, whereas from the radial velocity we can compute the frequency, which is 24.08×10^6 rad/s. If we compare those values with the theoretical ones we can see how the error is well below 1%, thus we can safely assume that any other trajectory simulated will be representative of the real one.

By setting all the geometrical and electrical parameters equal to the ones of our system we were able to simulate the trajectories of charged particles subject to the traveling magnetic field our accelerator produces. For both electron and ion trajectories we looked at different initial conditions, in particular we simulated particles entering the accelerator close to its center or more towards its sides, as well as particles with low initial velocity (in the

16

order of 1000 m/s) or particles with initial velocity close to the one of the traveling magnetic field.

Figure 2.9: Trajectory of electron entering the accelerator at its center (a,b) and close to its side (c,d) with $v_0 = 1000$ m/s.

Looking at the results of the simulations we see that some key aspects emerge. First of all, the position of the particle gives rise to different trajectories and velocity profiles; this has to do with the fact that close to the edge of the accelerator the electromagnetic field is stronger (the particles are closer to the wires of the coils) and thus the effect of the traveling field on charged particles gets magnified with respect to a more central position. In particular we see how extremely light particles like electrons that populate the regions close to the edge, fail to reach the end of the accelerator and hit its walls; this is definitely a negative effect since we lose the energy contribution of such particles.

We can also detect a great difference between what happens to electrons subject to a traveling magnetic field and ions subject to the same conditions. While electrons are very easily affected by the magnetic field, due to their low
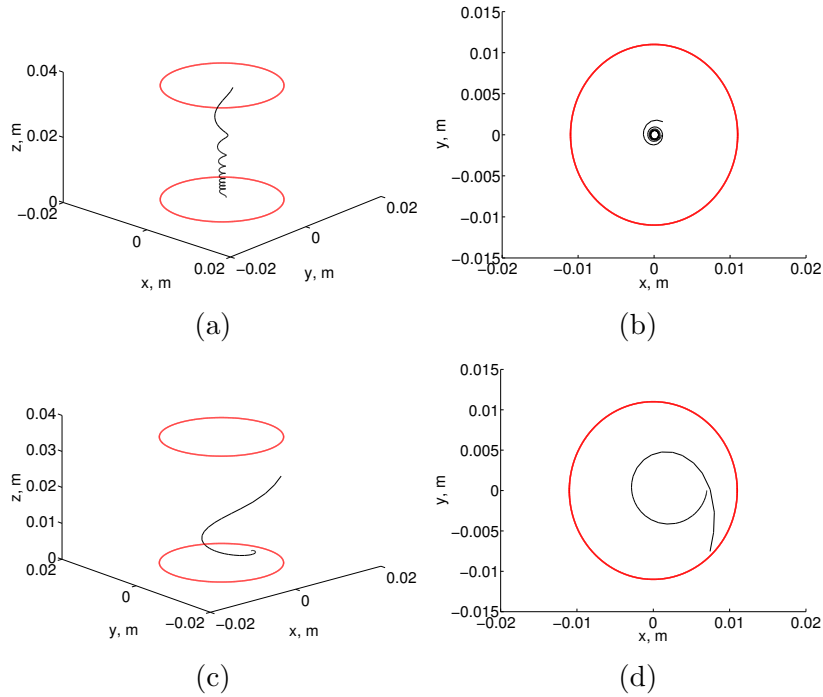
Figure 2.10: Trajectory of electron entering the accelerator at its center (a,b) and close to its side (c,d) with $v_0 = 9000$ m/s.

Figure 2.11: Axial velocity of electron entering the accelerator at its center (a) and close to its side (b) with $v_0 = 1000$ m/s.

mass, and reach extremely high velocities, argon ions (that are 5 orders of magnitude more massive) seem to have their motion only slightly perturbed; we can see how ions with a velocity much smaller than the one of the traveling magnetic field cannot even reach the end of the accelerator by the time the magnetic pulse traveled all the way, whereas ions with a velocity close to the one of the magnetic pulse show an interaction which only increases their velocity by less than 0.1 %, so an amount that is negligible.

That disparity has to do, as mentioned, by the great difference in mass be-

(a)
(b)
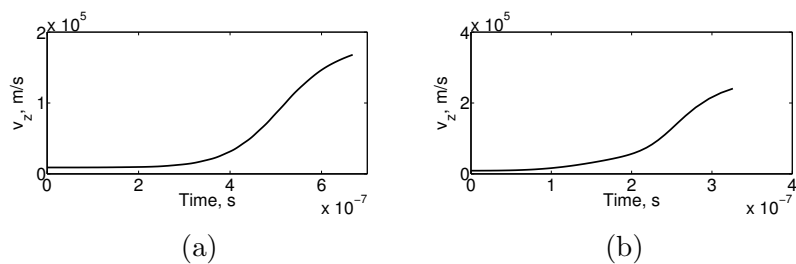
Figure 2.12: Axial velocity of electron entering the accelerator at its center (a) and close to its side (b) with $v_0 = 9000$ m/s.

(a)
(b)

(c)
(d)
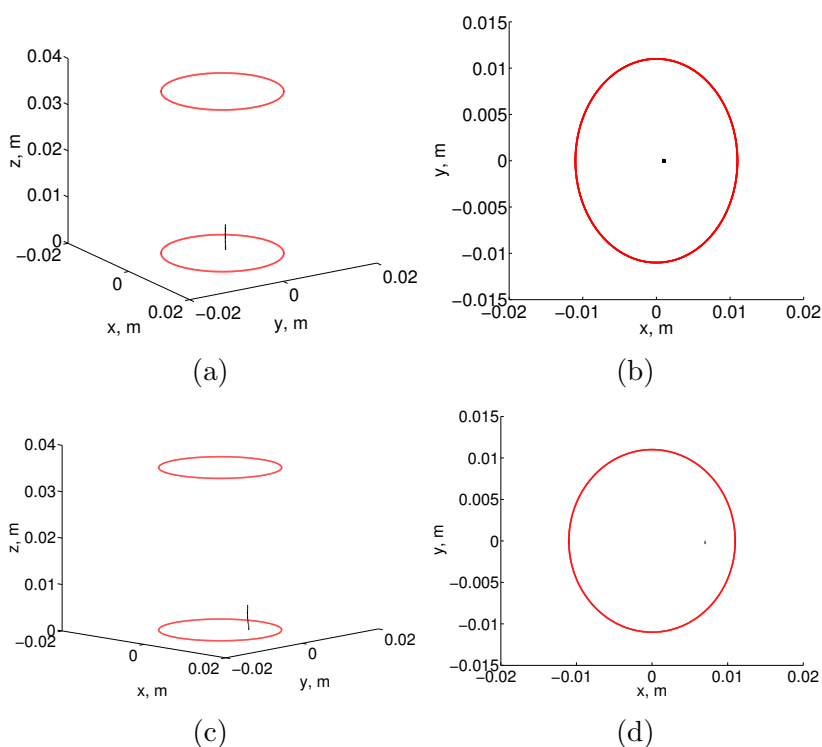
Figure 2.13: Trajectory of argon ion entering the accelerator at its center (a,b) and close to its side (c,d) with $v_0 = 1000$ m/s.

tween ions and electrons. Moreover, we have to specify that the strength of the magnetic field plays an important role in all this: the small interaction between the traveling magnetic field and argon ions is also due to the relatively low strength of such field (which has a peak of 100 G), however as previously stated our simulation parameters are taken directly from our real system, which has some constraints that do not allow to produce a very strong magnetic field.
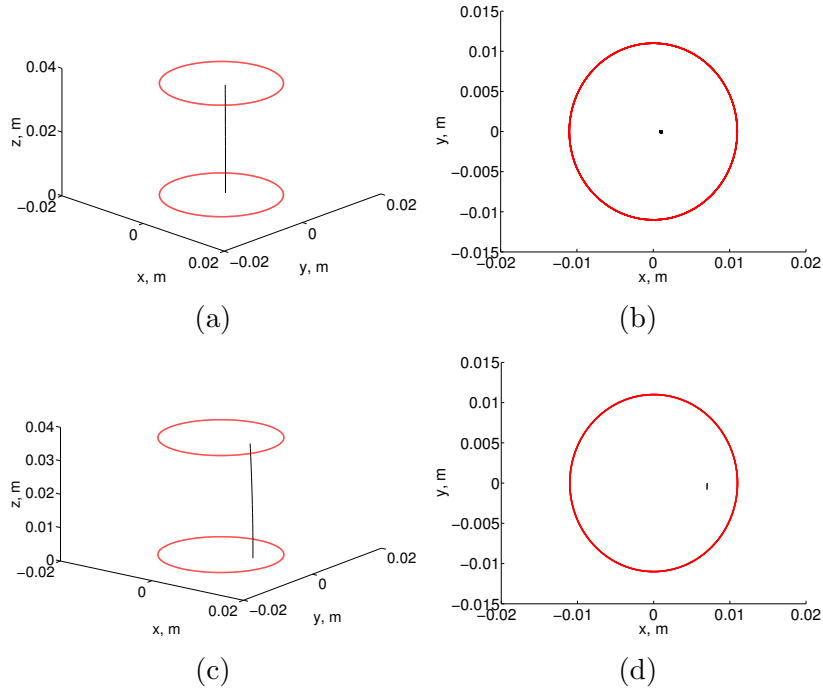
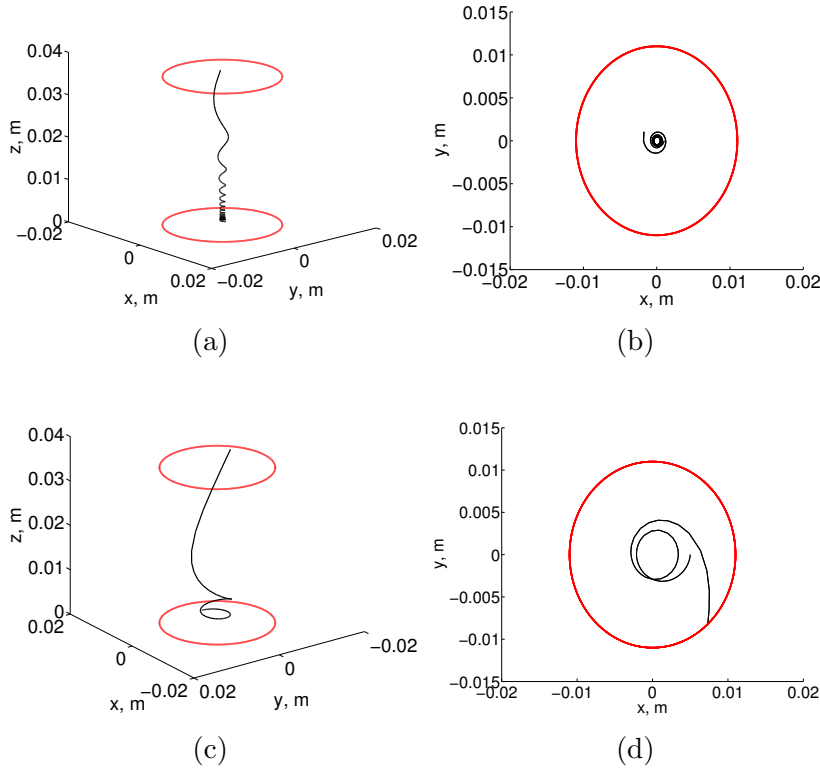Figure 2.14: Trajectory of argon ion entering the accelerator at its center (a,b) and close to its side (c,d) with $v_0 = 9000$ m/s.
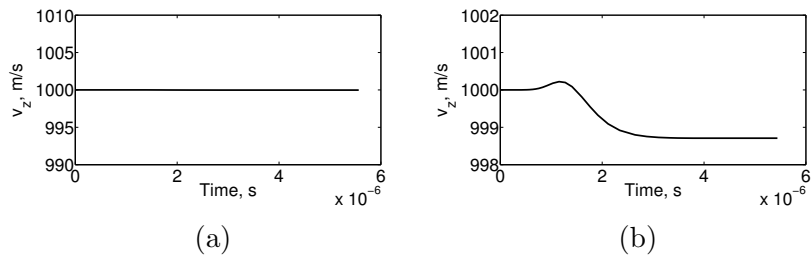
Figure 2.15: Axial velocity of ion entering the accelerator at its center (a) and close to its side (b) with $v_0 = 1000$ m/s.

The numerical results can also have another explanation, which relies on the notion that in order to understand physics of plasma we must not simply look at its components as if they were completely separate, but we need to take into account the different kind of interactions within the plasma itself (collisions, electromagnetic interactions, etc.) in order to have an understanding of how a plasma flow is affected by external phenomena. For what concerns our system, the results of our simulations give credit to what Lucca Fabris and Cappelli theorize; in their paper, they applied a PIC code to a system that is

20

(a)   (b)
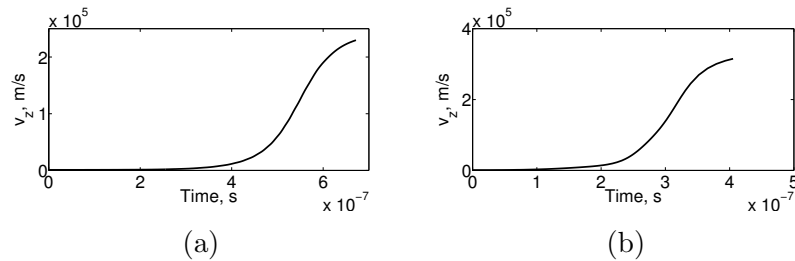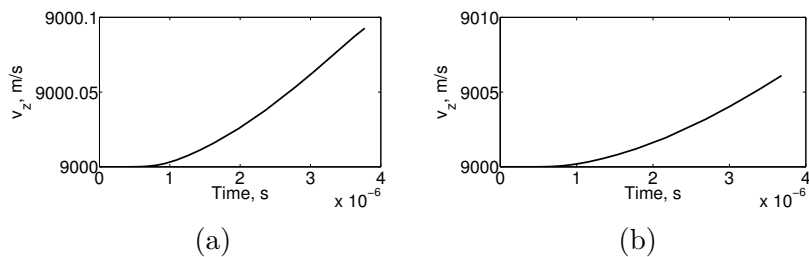
Figure 2.16: Axial velocity of ion entering the accelerator at its center (a) and close to its side (b) with $v_0 = 9000$ m/s.

conceptually the same as ours (it is a TMW accelerator with slightly different geometrical parameter and different circuit structure, but the physics behind it is the same as for our accelerator) and found how the traveling magnetic field initially affects only electrons, by pushing them downstream, while ions are left unperturbed since their kinetic response is too slow [31]. That is the same result we found with our trajectory simualtions .
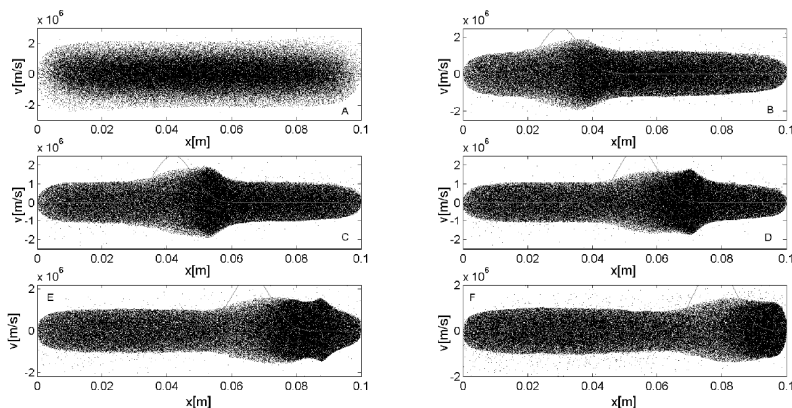
Figure 2.17: Electron phase space at different time instants [31].

They also show, however, that this motion of just electrons generates a charge separation right in front of the traveling magnetic field and thus a double layer is formed (a negatively charged region followed by a positively charged region). That charge separation gives rise to an electric field that holds electrons while accelerating ions. So, although the traveling magnetic field does not directly act to accelerate ions, it forms an electron sheath moving with itself that drags ions by means of its associated electric field. All that can bee seen in Figures 2.17, 2.18, and 2.19.
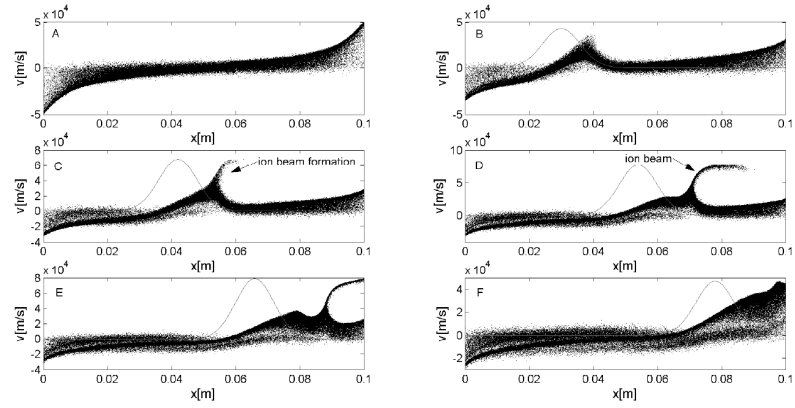
Figure 2.18: Ion phase space at different time instants [31].
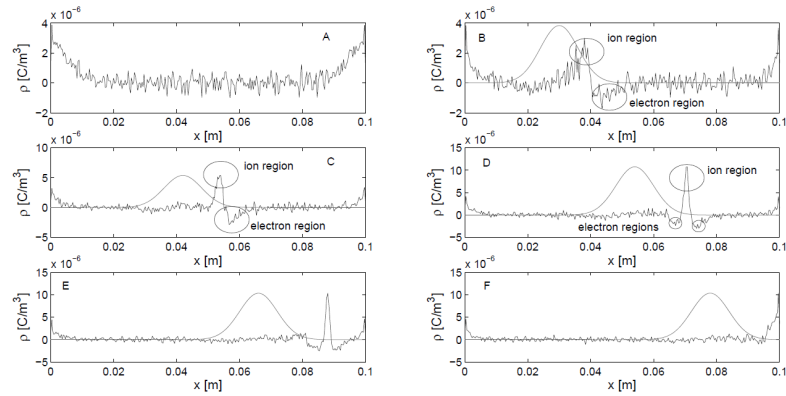
Figure 2.19: Charge density at different time instants [31].

Chapter 3

Traveling Magnetic Field Accelerator

3.1 Introduction

This section will give a description of the process followed to design the traveling magnetic field accelerator. Two different approaches are presented with an explanation of the philosophy behind them, along with benefits and downsides of both architectures. Finally we show which kind of system we thought was a better choice for our experiment.

3.2 Traveling Magnetic Field Generation

The basic concept of this kind of technology is to be able to generate a traveling magnetic field and have it interacting with a plasma flow.
The first step is to generate a magnetic field; the two simplest options are to either use a permanent magnet or to exploit the magnetic field generated by electric current flowing in a coil. The first one is not well suited for our purpose as although permanent magnets can easily give strong magnetic field, it is not possible to control it in such a way to obtain a traveling field with the desired characteristics. Exploiting current flowing in solenoids to generate magnetic field is a much better suit for our experiment since not only we can

manipulate the strength of the magnetic field generated simply by changing the current intensity but more importantly we can turn on and off the current at will, producing the magnetic field only during a set time-frame and allowing us for a more specific design of the magnetic field characteristics. The second step is to understand how to make the magnetic field move. Of course an electric current flowing in a coil generates a magnetic field, as shown in Figure 3.1, that is a static field. One idea that may come to mind in order to get the magnetic field to travel is to physically translate the coil; although this approach is correct, it has some critical problems, as first of all it would require a system to move it at velocities in the order of tens of km/s in order to achieve high enough specific impulse to make this technology worth, and second, even though we could move the coil at such speed it would not be advisable to do so as being this a technology to operate on spacecrafts, every moving part that is added can induce perturbations in its attitude and trajectory, so it would probably provide more negative effects than benefits from that point of view. Moreover, another problem that that solution has is related to how to eventually bring the coil velocity from the hypothetical velocity in the order of km/s to zero in a very small amount of time and over a small distance. All those problematics make that solution not feasible to generate a traveling magnetic field.
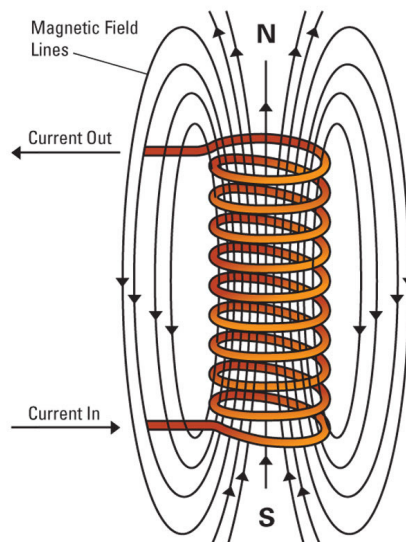
Figure 3.1: Schematic of an air core electromagnet.

There are various other ways to produce a traveling magnetic fields, mostly

relying on controlling electric current flowing in a set of consecutive coils. Those techniques do not need to implement moving parts, as they utilize passive components or other control systems to produce an overall effect of magnetic field translation.

3.2.1 Transmission Line

One of the simplest circuits to achieve a traveling magnetic field is that of a matched transmission line. A transmission line is an electric system that can carry electromagnetic signals from a source to a load.
In order to study transmission lines we can use a lumped parameters approach and divide it into a series of smaller sections as sown in Fig. 3.2.
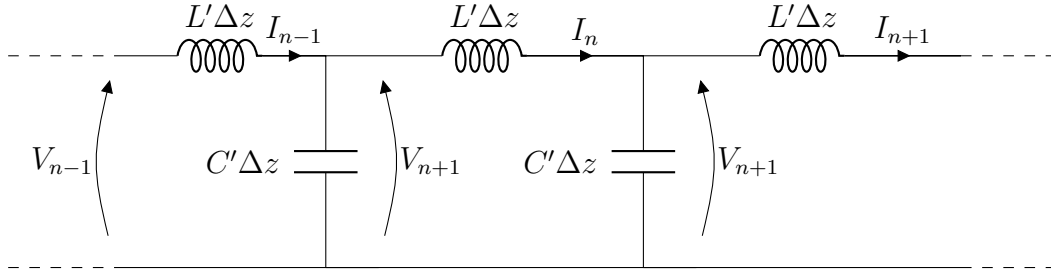
Figure 3.2: Lumped lossless transmission line model.

If we apply Kirchhoff's voltage and current laws, we can obtain expressions for voltage across n^{th} inductor and current through n^{th} capacitor:

$$\Delta L \frac{dI_n}{dt} = V_n - V_{n+1} \tag{3.1}$$

$$\Delta C \frac{dV_n}{dt} = I_{n-1} - I_n \tag{3.2}$$

Dividing by Δz both sides, we can define inductance and capacitance per unit length as: capacitor:

$$\frac{\Delta L}{\Delta z} = L' \qquad \frac{\Delta C}{\Delta z} = C' \tag{3.3}$$

So we can rewrite equations 3.1 and 3.2 as:

$$L'\frac{dI_n}{dt} = -\frac{V_{n+1} - V_n}{\Delta z} \tag{3.4}$$

$$C'\frac{dV_n}{dt} = -\frac{I_n - I_{n-1}}{\Delta z} \tag{3.5}$$

With the right hand sides that are basically spatial derivatives of current and voltage

$$\frac{\partial V(z,t)}{\partial z} = -L'\frac{\partial I(z,t)}{\partial t} \tag{3.6}$$

$$\frac{\partial I(z,t)}{\partial z} = -C'\frac{\partial V(z,t)}{\partial t} \tag{3.7}$$

Equations 3.6 and 3.7 are called transmission line equations; we can easily decouple them to obtain voltage and current wave equations along a lossless transmission line

$$\frac{\partial^2 V(z,t)}{\partial t^2} - \frac{1}{L'C'}\frac{\partial^2 V(z,t)}{\partial z^2} = 0 \tag{3.8}$$

$$\frac{\partial^2 I(z,t)}{\partial t^2} - \frac{1}{L'C'}\frac{\partial^2 I(z,t)}{\partial z^2} = 0 \tag{3.9}$$

From the solution of those equations we can determine the equations for some important parameters of a transmission line. The first one is the phase velocity, expressed as:

$$v_p = \frac{1}{\sqrt{L'C'}} \tag{3.10}$$

The second parameter is the wavelength of a sinusoidal wave in a transmission line:

$$\lambda = \frac{v_p}{f} \tag{3.11}$$

where f is the frequency of that sinusoid. Note that 3.11 can be rearranged to evaluate the phase velocity knowing wavelength and frequency.

Finally, we have the characteristic impedance of the line, defined as:

$$Z_0 = \sqrt{\frac{L'}{C'}} \tag{3.12}$$

Solving the wave equations written before leads to equations that can be interpreted as having two waves flowing in the transmission line, one moving forward (incident wave) and one being reflected. What is important is that we can define the reflection coefficient as the ratio between the intensity of the reflected wave and the incident wave, and in case of a closed transmission line it can be expressed as a function of the load impedance (Z_L) and the characteristic impedance (Z_0) as:

$$\Gamma_L = \frac{Z_L - Z_0}{Z_L + Z_0} \tag{3.13}$$

Equaution 3.13 shows how the best case scenario is when the load impedance is equal to the characteristic impedance, as in that situation the reflection coefficient is zero, meaning that all the input power is absorbed by the load and nothing gets reflected. Whenever a system with a transmission line is designed it is key to have no reflection to the power supply as that can damege it.

Due to the simplicity of this kind of circuit and its capability of working in both continuous mode with an AC power supply and in pulsed mode with a capacitor discharge as power source, the transmission line has been the system we designed as the first iteration for the traveling magnetic wave accelerator.

To design the transmission line for the accelerator we used a lossless approximation since we had no information about what kind of components we would end up using and so we had no information about their impedances. The goal is to produce a series of currents progressively phase shifted, to generate an overall magnetic field that travels along the accelerator. A simple schematic is shown in Fig. 3.3.

In order to design this kind of circuits we have to take into some key parameters, most of which are the ones previously defined:
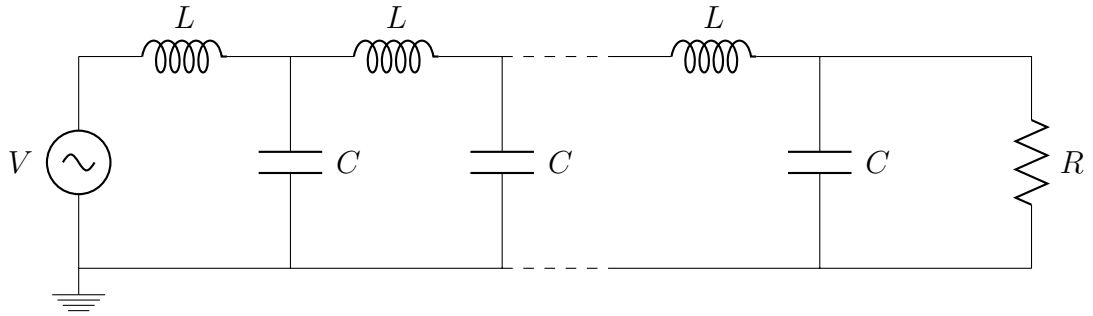
Figure 3.3: Schematic of a matched transmission line.

- Frequency of operations

- Inductance, Capacitance, and Impedance values

- Phase velocity

- Wavelength of the traveling magnetic wave

- Length of the accelerator

All those are somehow linked together in the design. Typically we impose a combination of frequency, phase velocity or wavelength to evaluate the missing parameter thanks to eq. 3.11. Phase velocity is then related to inductance and capacitance with equation 3.10.

Knowing those values we can then evaluate the characteristic impedance of the line, which we want to be equal to the load on which we close the transmission line, as previously mentioned.

While proceeding with the design, we had to consider some constraint and some nice-to-have requirements. The frequency of operation depends on the power supply used to power the transmission line, and it is typically quite hard to have a power system capable of working on a very wide range of frequency, thus leading to choose the frequency allowed by the available equipment. Then, being our goal that of keeping the size of the accelerator small, we needed to keep the length-to-diameter ratio small and that influences the shape of the coils; typically one solution is to use multilayer inductors, however it is important not to have too many layers both because the more layers a coil has the stronger the mutual inductance effect is and because many layers mean that the outer layers diameters are much bigger than the inner ones, leading to a much smaller magnetic field contribution (being the magnetic field proportional to 1/R). Finally, it would be nice to

have a characteristic impedance matching the generator inner impedance, otherwise we would need a matching box to place between the line and the source.

With those constraints the frequency (as said) is fixed, meaning we need one more parameter between capacitance or inductance to then determine the other one and to determine the characteristic impedance. What can be done is to impose the capacitance value, since the capacitors are components that are typically bought and it is easy to check which values are available and which ones could be better even in terms of their geometrical factor. Other parameters that we can impose is the length of the accelerator, which as said we want to be quite small (in the order of few cm), and the wavelength of the electromagnetic wave. For the second parameter it is important to keep two things in mind: the product between wavelength and frequency gives the phase velocity, which we do not want to bee too large (a good value would up to 30,000 m/s, thus if we are bound to use a high frequency (in the MHz range) we want to set a small wavelength; however, smaller wavelength means that we need to build our accelerator with more LC subcircuits otherwise the phase shift we would obtain does not follow what we may have wanted; having many circuits could be a problem for us since due to the geometry constraints we would need to build very small circuits, something that can be extremely hard to achieve.
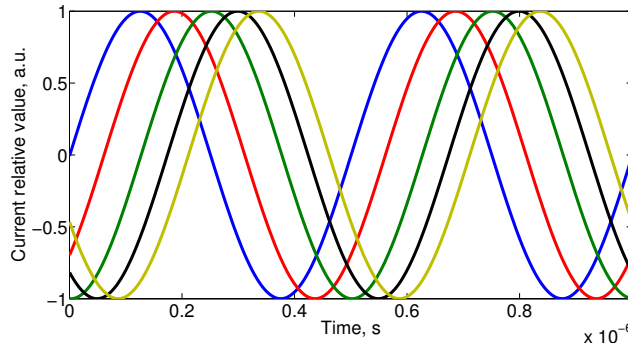
Figure 3.4: Current pattern with enough LC subcircuits per unit length

As we can see from figures 3.4 and 3.5 there is a big difference between using an appropriate number of LC subcircuits within the accelerator length and not doing so, with the second case leading to a non-uniformity of phase shift. The explanation of that behavior comes from the fact that building a transmission line with LC components means building it according to its lumped parameters representation: for an accurate lumped representation of a continuous system we need to use the appropriate number of elements,
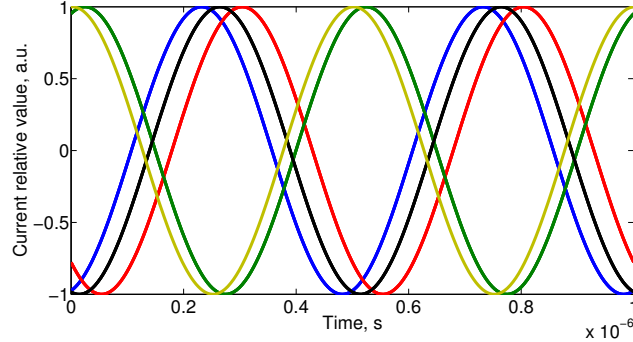
Figure 3.5: Current pattern with low number of LC subcircuits per unit length

otherwise the result one obtains does not describe the system under study. So one problem we faced is that the frequency constraint along with limitations of how small the wavelength could be led to magnetic field velocity levels that were too high for our purpose (about twice as much as our maximum goal of 30,000 m/s).

When designing the transmission line for our traveling magnetic field accelerator we tried to follow what done by others [31] by setting the number of LC circuits at around 10, with no more than 1.5 spatial wavelengths within the accelerator length. The phase shift between currents flowing through two consecutive inductors is simply determined by the number of such components and is ocmputed thanks to the following equation:

$$\Delta\phi = \frac{360°}{N_L} \tag{3.14}$$

As previously mentioned, we want our transmission line to be closed by a purely resistive impedance equal to the characteristic impedance of the line, which ideally should be matched to the power supply impedance; that is the biggest limitation of this technique. If we design all the components to get a 50 Ω characteristic impedance (that is the typical impedance of power supplies), that introduces a big limitation on the current levels we can achieve, since power supply can only provide a limited amount of power that prevents us to reach high enough voltage levels to get relevant current in our system. In fact, in this case we predicted magnetic field levels of few tens of Gauss at 1000 V input, which is over the limit the power supply can provide (at a more reasonable voltage level of 100 V we would get no more than a few Gauss, which was pretty much irrelevant). Another problem related to this

case is that with such high resistor closing the line we are actually damping huge amounts of power through it.

Another option would be to not deal with the matching with the power supply at the transmission line level and use a matching box for that purpose; in that case we can produce a line with small characteristic impedance allowing for higher current levels to flow. This however does not completely solve the problem of low magnetic field: in fact, being the square of the characteristic impedance directly dependant on the L/C ratio, to make it small we need high capacitance value and low inductance value. That however makes it so the coils may end up being simply a single loop of wire, which even with high current levels do not generate very high magnetic field (few tens of Gauss at a hundred Amps of current).

Overall we can say that although promising as a technique to generate a traveling magnetic field, for our purpose it did not turn out to be the best solution because of the frequency constraint and the problematics with generating strong enough magnetic field to affect plasma.

3.2.2 Independent Circuits

In an attempt to try to overcome all the limitations of the transmission line we decided to follow a different route for the traveling magnetic field generation. An interesting technique is based on time delaying the current flowing in a series of independent coils. That way we are no longer exploiting passive components within the system (capacitors) to phase shift the current to produce the effect of translation, instead we are acting directly on the currents from outside by controlling the timing at which they are made to flow in the circuits.

Even this technique allows us to operate either in continuous or pulsed mode, however continuous operations are not easy to achieve. In fact, to obtain that mode of operations we would need one custom made power supply for each circuits and each of them should be set to produce an AC voltage signal with a precise phase shift (or time delay) to produce an overall translation of the magnetic field; the task of building the power supplies could not be handled by us since it required much deeper understanding in the field of power electronics and a lot of resources, and with the time limitation we had it was not feasible to follow that road. Another point in favor of the pulsed mode is that if we recall the theory behind the traveling magnetic field, the axial force produced by the field is always in the same direction even for oscillating field, meaning that even in continuous operations the effect the plasma

flow is subject to is the same as that obtained with pulsed magnetic field.
For those reason we decided our system would be working in pulsed mode.
That way of operating the accelerator relies on using capacitors to produce
the current that flows in each circuit by alternating a charging phase and a
discharge phase at a set frequency.

A schematic of the basic circuit is presented in Figure 3.6
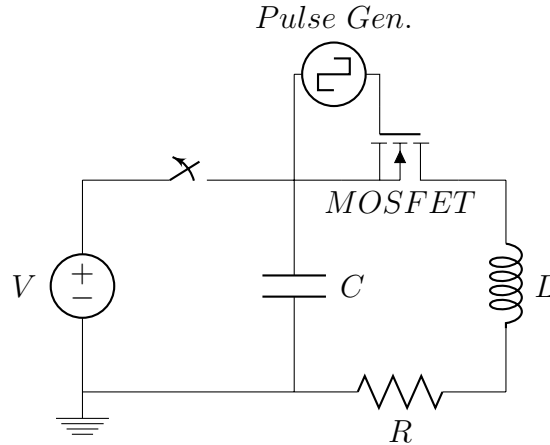
Figure 3.6: Single circuit schematic.

Thanks to pulse generators that control when the main circuits are open or
closed we can control the time delay between currents, thus controlling the
magnetic field propagation velocity.

With respect to the transmission line, this technique allows for more free-
dom in selecting the circuit's parameters, simply because some of them are
totally decoupled. One example is the phase velocity: with the transmis-
sion line it was linked to the frequency of operations, the wavelength, the
inductance value, and the capacitance value. This time however it simply
depends on the time delay between two consecutive current pulses and the
spatial distance between two consecutive coils. That lets us set the velocity
value independently from any other parameter, allowing for the possibility
of testing different field velocities without changing the components of the
accelerator. Such flexibility is of course a huge bonus that this system pro-
vides.

When designing this system we need to make sure to obtain a current pulse
from the capacitor discharge and not a current going back and forth the
circuit. Once one parameter of the RLC circuit is imposed (typically the
inductance L, as we want to make sure to keep the size of the inductors un-
der control), we can easily determine the other two thanks to the following
equations:

$$2\pi f = \frac{1}{\sqrt{LC}} \tag{3.15}$$

$$\zeta = \frac{R}{2}\sqrt{\frac{C}{L}} \tag{3.16}$$

where f is the resonant frequency and ζ is the damping coefficient.

Note that imposing L is not enough to determine the values of R and C; we also have to decide what resonant frequency and damping coefficient we want. For the first parameter, it is enough to look at how different frequencies affect the current pulse, as shown in Figure 3.7; in particular, we can note that higher frequencies lead to narrower pulses but the pulse peak is also lower, whereas smaller frequencies lead to higher current peaks but wider pulses, so it is all about finding the best trade off between those effects.

(a)

(b)
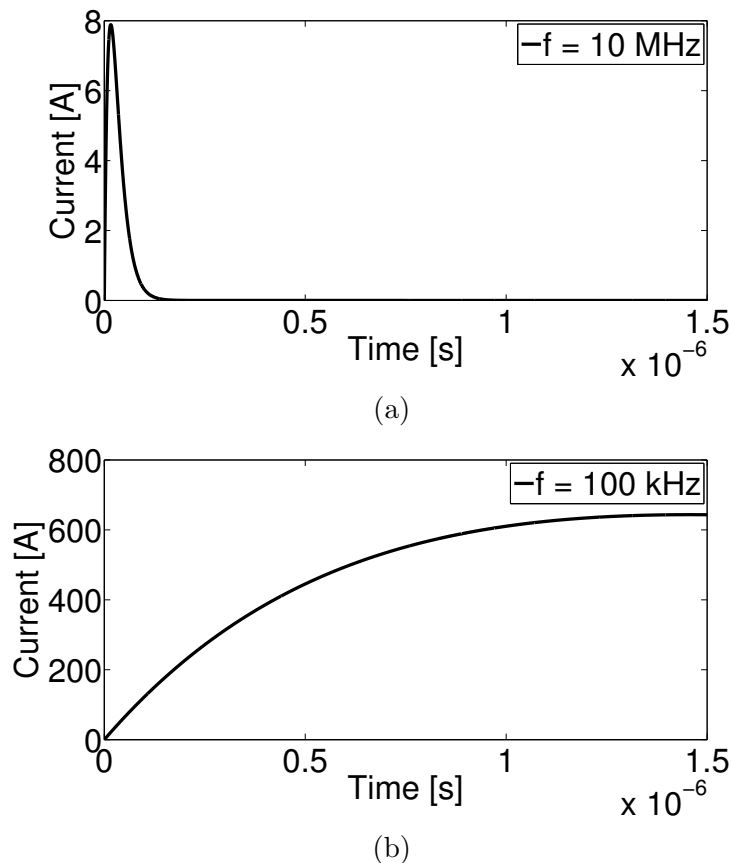
Figure 3.7: Current pulse at different frequencies: (a) high frequency, (b) low frequency.

For what concerns the damping coefficient, deciding its value is more straight-forward: we want our system to be as close as possible to the condition of critical damping $\zeta = 1$, but still be underdamped in order to achieve a small reduction of the pulse width with respect to the critically damped configuration; we definitely not want our system to be overdamped both because the pulse width would be much larger and because it would mean we need large resistors, and thus the current peak would be smaller.
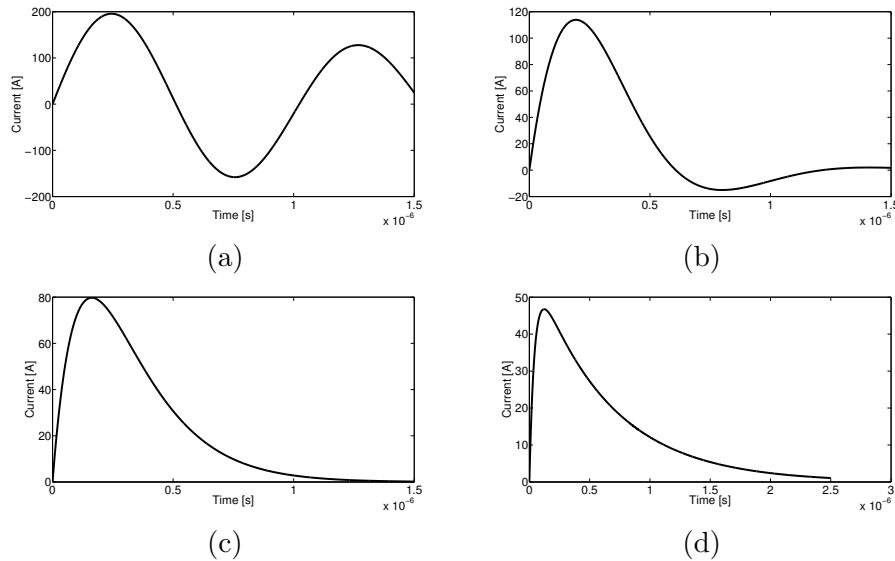
Figure 3.8: Current pulse at different damping coefficients: (a) $\zeta = 0.1$, (b) $\zeta = 0.54$, (c) $\zeta = 1$, (d) $\zeta = 2$.

With reference to Fig. 3.8, the condition we would like to achieve is that of image (b): the peak current is high yet there is very little current going backwards, and the pulse width is limited. Note that as long as the negative current peak remains in the order of less than 10% of the positive peak its presence should not have a negative impact on the accelerator performance. Another thing to consider when designing this type of system is that being all circuits independent, how many of them we use does not influence the performances or the parameters in any way. In case of malfunctioning of some components or circuits, if we do not have the possibility of substituting them we could simply change the number of circuits implemented without altering the system (except for the total length).

One of the downsides of having all independent circuits, however, is in the electrical connections: to correctly operate, each RLC circuit needs its own connections with the power supply and pulse generators, which can be tricky to fit in a confined space. Moreover, it is of fundamental importance to avoid

any electrical path that could rise from the tight packing of circuits needed to satisfy the constraint on the size of the accelerator; in fact, if conducting portions of two adjacent circuits come in contact the path the current follows may be altered, leading to system malfunction or even to the damange of the more sensitive components.

Chapter 4

Experimental Proof of Concept

4.1 Introduction

In this chapter we describe the experimental setup developed to study the feasibility of an acceleration stage of a plasma thruster based on traveling magnetic field. After presenting the objectives of our experimental work, we will describe the setup used, in terms of both the accelerator itself and all the equipment used. Then, the results of the experiment will be presented along with a discussion of them. Finally, some conclusions will be drawn and some possible future developments will be proposed.

4.2 Objectives of the Experiment

The main goal of the experimental work is to prove the interaction between a traveling magnetic field and a plasma flow, and determine its effects on the performance of a plasma thruster. Being this work at a proof-of-concept level, we do not expect to reach optimization levels or efficiency levels that would allow an implementation of this technology on current thrusters. In order to achieve that goal, the main objectives of the experiment are: to achieve a traveling magnetic pulse and to be able to control its phase velocity; to achieve a stable mode of operation; to verify the presence of an interaction between the magnetic field and the plasma flow coming from a plasma source

(or a thruster); to determine the effect of the interaction on the plasma velocity; to determine how the performance of a thruster change when this technology is applied to it.

4.3 Accelerator Setup

The accelerator is made of 7 independent basic circuits (described in Chapter 3) placed in sequence one after the other. Following the steps presented earlier, the parameters that came out of the design phase are as follows:

- L=0.6 µH

- f=1 MHz

- ζ=0.68

- C=0.0423 µF

- R=5 Ω

- V_{ch}=800 V

- f_{rep}=5 Hz (can be varied)

Inductors - The reason behind the selection of the inductance value L is simple: one of the goals we wanted to achieve with the design of the accelerator was to keep the aspect ratio as small as possible. It is true that having larger inductance value would yield stronger magnetic field, but that benefit would be balanced by the negative effect of the increase in length. That because although having coils with many multiple layers is possible, the larger the radius of a layer the weaker the magnetic field it produces is, since B is proportional to $1/r^2$; so in order to appreciate better the effect of larger inductance we would need more turns per layer instead of more layers, thus increasing the overall length of the accelerator (something we would like to avoid since as said we want a small length-to-diameter ratio). So, after evaluating some trade offs between inductance value and size, we decided the value of L=0.6 µH suited well our desing. Such coils have then been built by winding a copper magnet wire of 2 mm diameter on two layers with two windings each; the resulting coils have an inner diameter of 1" and an

external diameter of 1.18".

Frequency of oscillation and damping - As mentioned previously in Chapter 3, the resonant frequency f and the damping coefficient ζ have been chosen to shape the current pulse according to our needs, and from them we were able to determine the parameters C and R of the circuits.

Charging Voltage - For the voltage at which we wanted to charge the capacitors we opted for 800 V as maximum value to achieve high enough peak current to produce a magnetic field in the order of a hundred Gauss. To make sure our system would be able to withstand such voltage level we chose all components with slightly higher voltage rating (set at 1000 V), which is key to prevent malfunctioning especially for the most sensitive components.

Capacitors - We used two 0.022 µF metallized polypropylene capacitors connected in parallel to achieve the desired value of capacitance. The reason of this choice comes down to the fact that we wanted to obtain a capacitance value as close as possible to the one evaluated in the design phase. Moreover, we opted for those capacitors because their geometrical characteristics were perfect for our purpose, since they are small enough to allow us to satisfy our size constraints but at the same time they are big enough to allow for easy installment in the circuits. We chose them also because they satisfy the requirements in terms of maximum charging voltage and energy per pulse.

Figure 4.1: Capacitor used in our circuits.

Resistors - We connected four 20 Ω wirewound non inductive resistors in parallel in order to achieve the desired resistance value. The reason of that is because due to the large peak current expected in the circuit, we wanted to reduce the chances of breaking those resistors by splitting the current flowing

in them thanks to the parallel connection.
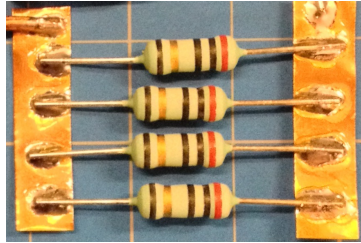
Figure 4.2: Resistors implemented in the circuit.

In order to achieve the effect of a traveling current pulse (and thus a traveling magnetic pulse) we had to time-delay the capacitors' discharges. The amount of time dt between the discharges of two consecutive circuits depends on what phase velocity we want to achieve. In case of a magnetic field traveling at 12 km/s we need a time delay of about 0.42 µs; Figure 4.3 shows the current profiles of the first three circuits of the accelerator in an ideal case:
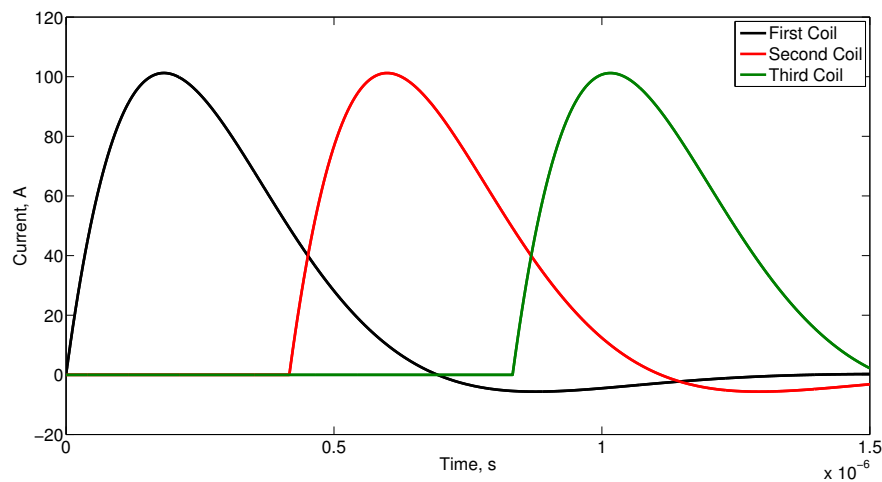
Figure 4.3: Ideal crrent profiles of three consecutive circuits.

There are a couple of interesting things to note about the current pulses shown in Figure 4.3: first, as already mentioned, they come from the simulation of ideal circuits; it is extremely hard to get all the informations needed to run a simulation with realistic components, so we thought it would be better to look at the ideal case and then expect a loss of performance due to all

the dissipation mechanisms that are present in the real case. The second important fact is that we can see how the time-delay between pulses is slightly smaller than the pulse width and we have some overlapping. Although at first it may seem like a negative aspect, it actually helps us increase the magnetic field in the accelerator without having to increase the current in each circuit; this because the magnetic fields produced by two coils close-by add up together creating a stronger overall magnetic field. This effect of course gets magnified the smaller the time delay between pulses is. The downside of that is an increase of the magnetic field pulse width, which is something we need to keep under control to avoid the generation of a magnetic pulse so wide that it acts as a static magnetic field with a translating perturbation. We need to have a distinct magnetic pulse traveling along the accelerator.

Switching Mechanism - A very important component in our design is the switch used to close the RLC circuit once the capacitors are fully charged. It is crucial to have it not only fast enough to be able to match the real current pulse with the ideal one, but also to have it capable to withstand such high current peak as the one we want. After some research we found out best option to be a Silicon Carbide Power MOSFET, able to let through 60 A of continuous current or 160 A of pulsed current. Being a solid state switch it is also very fast, with turn on time in the order of tens of nanoseconds. To drive the switch we used a pulse generator (which is described more in depth in a later paragraph), able to provide a squared pulse of tunable width in order to close and open the switch according to the desired operative phases.
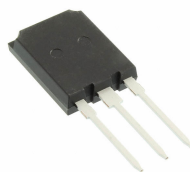
Figure 4.4: MOSFET implemented in our circuits.

One characteristic of this type of switch is the correlation between its internal resistance and the driving voltage. As from Figure 4.5, we see that the higher the driving voltage V_{GS} is, the smaller the internal resistance is.
This aspect had a huge impact on the design of the overall apparatus: since the pulse generators we used could provide about 3 V, we had to apply an amplification stage of the driving signal to avoid the region of high internal
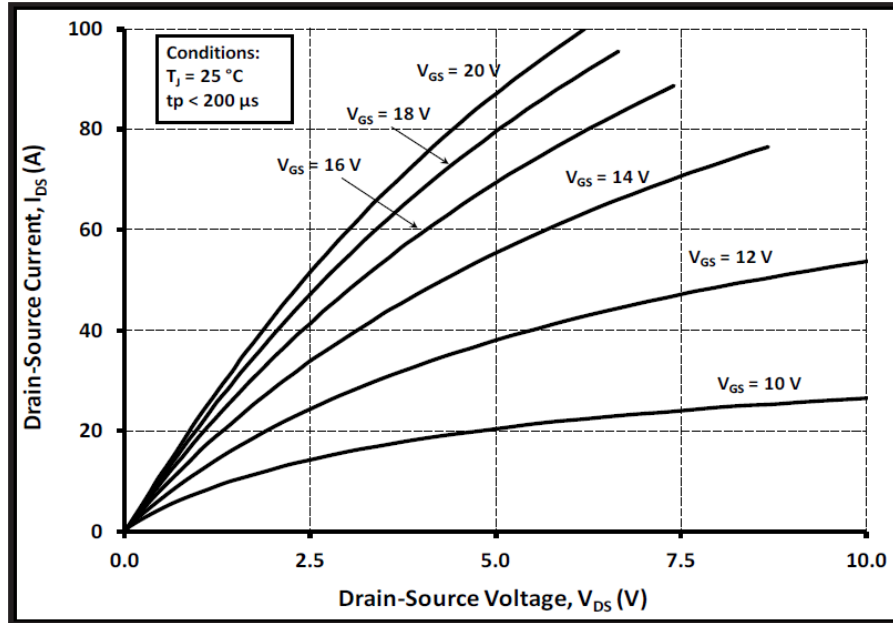
Figure 4.5: Switch output characteristics at 25° C [16]

resistance of the switch.

Amplification Stage - The amplification stage consisted in a op-amp circuit with negative feedback. The closed loop gain has been set to 5, enough to bring the input voltage from the 3 V of the pulse generator to about 15 V, needed by the MOSFET to work with a low enough internal resistance. That was done by setting the resistors R_f and R_g to 2 kΩ and 500 Ω respectively, in accordance to the expression for the closed loop gain:

$$G_{CL} = 1 + \frac{R_f}{R_g} \tag{4.1}$$

We built one amplification circuit for each MOSFET (so a total of 7) on breadboards, with multiple circuits installed on each breadboard.
We used Linear Technology LT1055 operational amplifiers powered at ±15 V; inputs and outputs were realized through BNC connectors.

Relay - To obtain capacitor discharges that are not influenced by the power supply we had to make sure we had a way to disconnect the RLC circuits from the power supply itself once the capacitors were fully charged. This
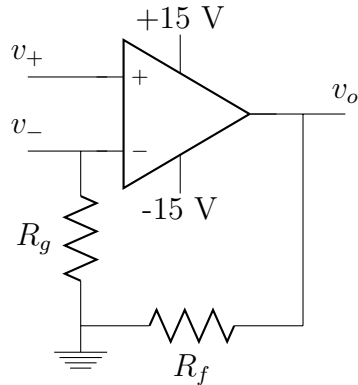
Figure 4.6: Schematic of an op-amp circuit.
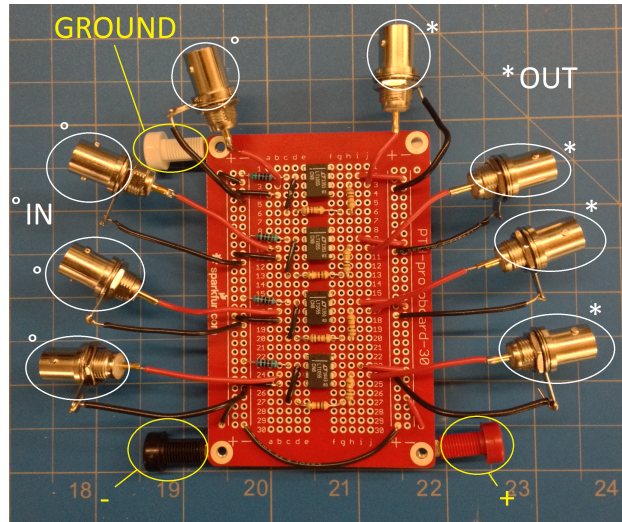
Figure 4.7: Picture of op-amp circuits.

operation has been accomplished by mounting IXYS Integrated Circuits Division CPC1981Y solid state relays on every connection going from the power supply to the capacitors. All of them were operated at the same time, so that every circuit was charged at the same time and then disconnected from the power supply at the same time.

Repetition frequency - Since the accelerator is operated in pulsed mode we had to set a repetition rate and with that determine how often we would perform the charge-discharge operations. Theoretically the maximum repe-
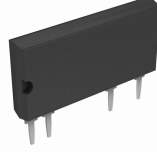
Figure 4.8: Solid state relay.

tition frequency we could obtain comes from:

$$P = n\frac{1}{2}CV^2 f_{rep} = IV \tag{4.2}$$

$$f_{rep} = \frac{2IV}{nCV^2} = 81\text{Hz} \tag{4.3}$$

Where n is the number of circuits the accelerator is made of (7 in our case), C is the capacitance, V is the charging voltage, and I is the charging current. As already mentioned the charging voltage was set at 800 V while the charging current was set at 10 mA, which is the value of current that our generator could supply during the charging phase.

That result does not take into account the time-response of the relays, which reduces the time available for charging the capacitors, and the fact that although we could get close to such frequency we would only get a partial charge thus obtaining a current peak value well below the maximum obtainable. That is due to the effect of the parasitic resistance of the circuit, which leads to a charge time constant that is too large to allow for a complete charge of the capacitors.

For those reasons, we decided to mainly set the repetition frequency at 5 Hz, with some test performed at slightly higher frequencies. The mean power at 5 Hz turns out to be about 0.5 W, which definitely satisfied the constraint of low power operations.

Pulse Generator - As mentioned, time-delay between circuits was obtained through the use of pulse generators. In particular, we used three Stanford Research System DG535 pulse generator to control all MOSFETs and relays. With reference to Fig. 4.10, we had a main pulse generator (A) set to open and close the line from the power supply to the capacitors at the chosen repetition frequency. Such pulse generator also triggered two additional pulse generators (B and C) used to operate up to four MOSFETs each; that way we made sure to discharge the capacitors only after disconnecting the power supply. All of them provided pulses at TTL voltage level before amplification. Labels A, B, and C of the pulse generators refer to Fig. 4.10.

Figure 4.9: Picture of a Stanford Research System DG535 pulse generator.

Note that the amplification stages of the signals coming from the pulse generators have not been represented in Fig. 4.10 for better clarity.
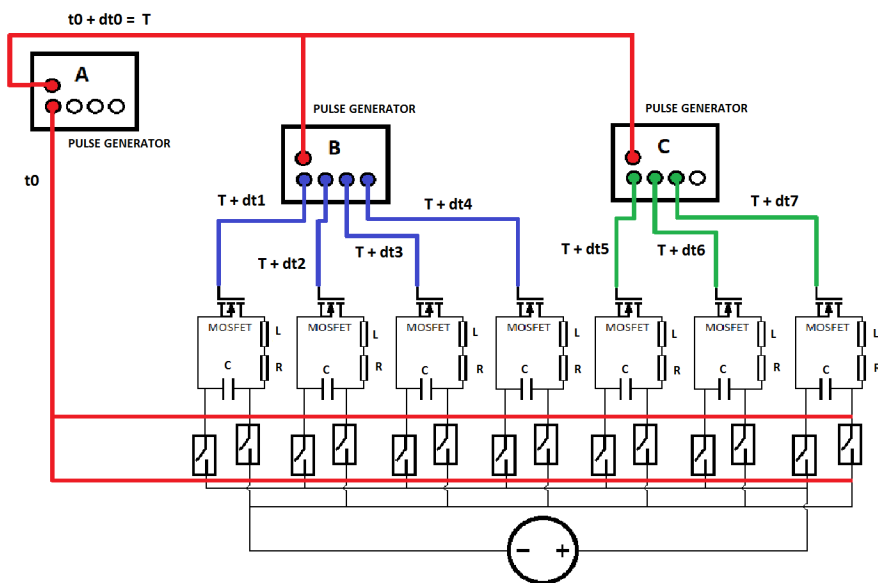
Figure 4.10: Simplified system schematic.

Figures 4.11 shows a single circuit assembled (without the relays applied), while Figures 4.12 and 4.13 show the overall system mounted on the quartz tube respectively with plasma off and plasma on.
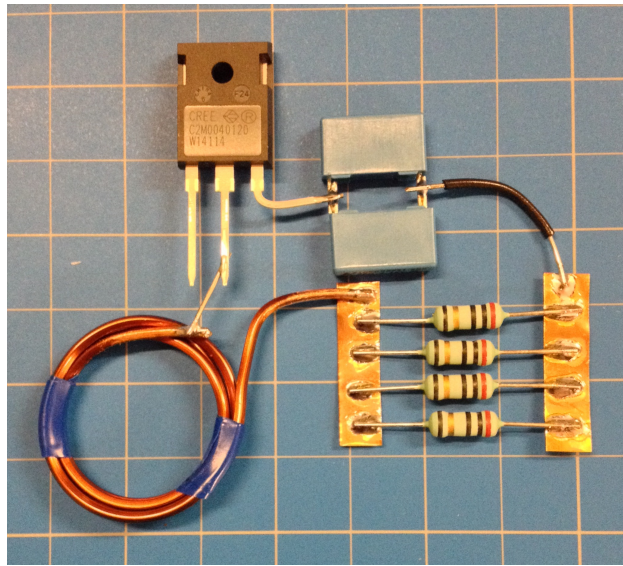
Figure 4.11: Picture of a single circuit.
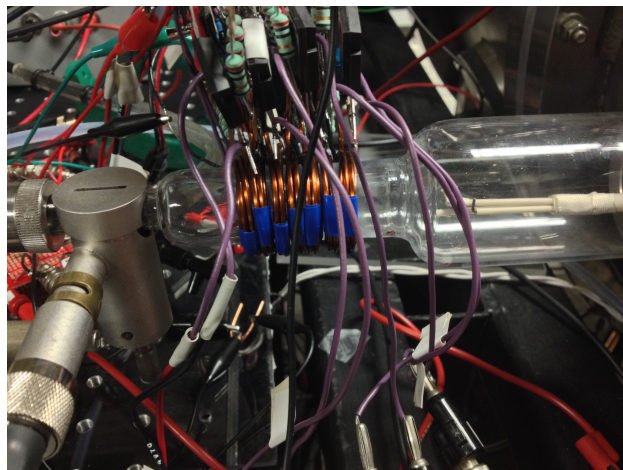
Figure 4.12: Picture of the setup without plasma.

4.4 Vacuum Chamber

The whole experiment has been carried out outside the small vacuum chamber of the Stanford Plasma Physics Lab (Figure 4.14), with the accelerator and plasma source mounted on a quartz tube placed outside the chamber and connected to it by a port present on its side. The vacuum chamber is a 0.6 m diameter, 1.2 m length stainless steel chamber, pumped down to a base
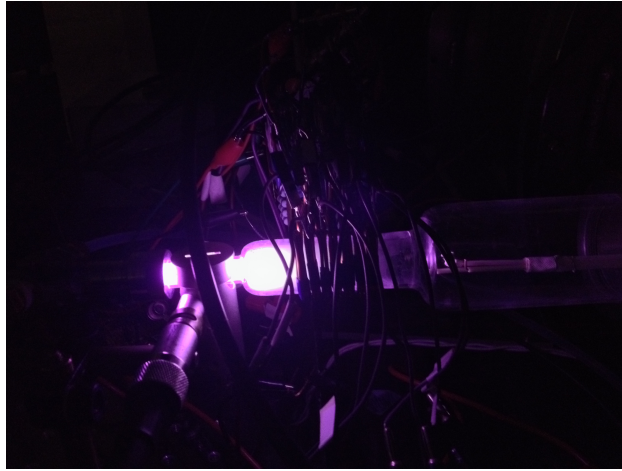
Figure 4.13: Picture of the setup with plasma.

pressure level of 10^{-6} Torr when no mass flow is injected, or 10^{-4}-10^{-5} Torr during thruster operations; rough vacuum is obtained through a mechanical pump and blower while lower pressure levels (the ones cited) are achieved by a single 50 cm diameter cryopump.
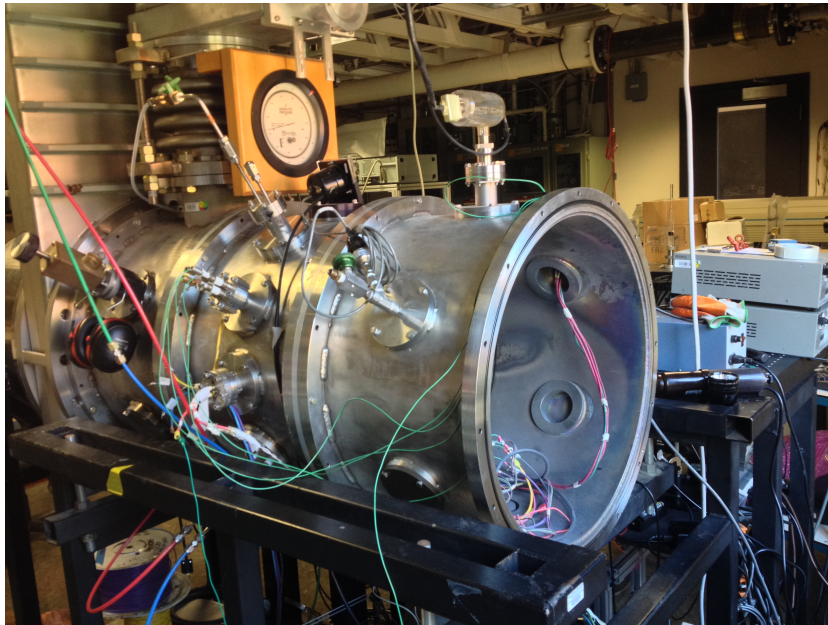
Figure 4.14: Picture of the small vacuum chamber.

4.5   Power Setup

High voltage DC power supply - To charge the capacitors we used a Power Designs 3K10B high voltage DC power supply, capable to provide up to 3 kV at 10 mA (Figure 4.15). Its voltage range allowed us to safely go up to the voltage range required by our accelerator, while its current output was enough to allow us to charge the capacitors in a limited time frame. It was able to provide DC power with both positive and negative polarization, although we only needed the positive one. It was connected to the capacitors by means of a high voltage BNC cable, with relays in between each connection, as showed in Fig. 4.10.
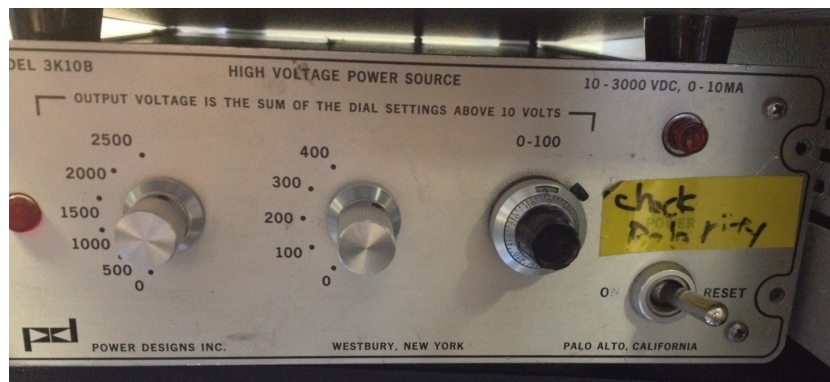
Figure 4.15: Picture of the high voltage DC power supply.

Op-amp power supply - We used a custom made DC power supply to provide the correct voltage to power the amplification circuits. In particular, such generator could output ± 15 V, in line with what suggested in the op-amp datasheet.

4.6   Plasma Source

Being the traveling magnetic wave accelerator the second stage of a dual-stage electric propulsion system we needed a source of plasma to test it with. For that we relied on two different technologies: a helicon plasma source (helicon thruster) and a microwave plasma cavity.

Helicon plasma source - A helicon plasma source relies on the formation of helicon waves to ionize a gas flow. Helicons are wave modes that propagate in a cylindrical, axially magnetized plasma column. They propagate in the plasma column and the energy associated to the wave mode is absorbed by electrons through collisions (electron heating); the heated electrons then bombard the incoming gas flow and ionize it [33]. The helicon plasma source used in our experiment was actually a helicon plasma thruster built in Stanford Plasma Physics Lab for a different work [4]. A helicon thruster consists of a feeding line for the propellant, a helicon RF plasma source, and an acceleration stage. The plasma generation system consists of an RF power amplifier, a matching network and an antenna wrapped around the quartz tube in which plasma is ignited. In particular, helicon discharge was produced using an HP 83732B signal generator and a ENI 320L RF power amplifier; the whole system operated at a frequency of 40 MHz at different power levels. A static magnetic field generated by permanent magnets or solenoids is applied to get the proper modes of propagation of the helicons in the plasma, allowing for better power deposition, to provide confinement of the plasma, reducing energy losses through wall collisions, and to get a magnetic nozzle effect.

The helicon was ignited in a 1.25 cm diameter quartz tube and then accelerated thanks to a magnetic nozzle produced by samarium-cobalt magnets, with a peak magnetic field of 2.5 kG. The magnetic nozzle simply acts to convert the plasma internal energy into kinetic energy to generate thrust.

A helicon plasma thruster has some advantages over other systems: no electrodes are necessary, no neutralized is needed since the exhaust is neutral, the erosion is reduced thanks to the plasma limited interaction with the structure, and it can produce plasma densities higher than other discharge techniques at the same power level.

Although the helicon thruster could run by itself, we would like to add an acceleration stage (like the traveling magnetic field accelerator) to increase the propulsive efficiency and to increase the I_sp. Similar configurations with helicon plasma source have been applied to other electric propulsion systems, such as the VASIMR [17, 44] or the FARAD (developed at Princeton University) [14], however they required much larger continuous power (VASIMR) or pulse energy (FARAD) to operate.

For our experiment the thruster was made to run on argon, although different propellants can be used (even water vapor for example).

Microwave discharge cavity - A discharge cavity is a system used to transfer power from a microwave source to a gas flow. The cavity itself is a resonant structure, with the purpose of increasing the electric field in the
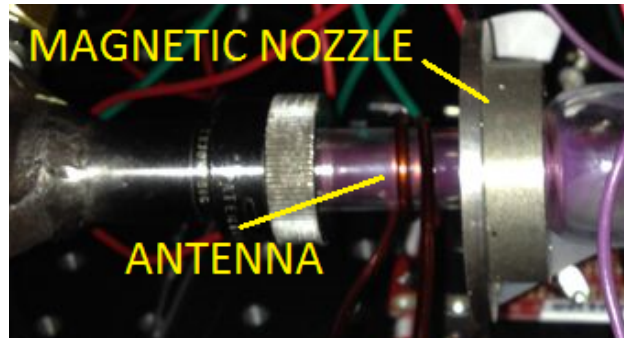
Figure 4.16: Picture of helicon thruster used.

gas. In order to transfer the maximum amount of power to the gas, some tuning has to be made by matching the impedance of the structure to that of the microwave source and by properly tuning the resonant frequency of the cavity. This type of plasma source is typically used for its high degree of ionization, no internal electrodes (and thus simplicity of mounting) and little electromagnetic interference.

For our experiment a 2.45 GHz Evenson microwave discharge cavity has been used [21]. Its resonant frequency can be tuned by a tuning stub while the coupling with the microwave source can be achieved by a coupling slider. A removable cap allows for easy mounting on the quartz tube. Due to the high temperature that can be reached in the ionization region, cooling air is made to flow thanks ot a tube positioned on the body of the cavity itself; that is needed to cool the quartz tube. A picture of the cavity used is shown in Fig. 4.18

4.7 Diagnostic

The diagnostic is composed by three different kind of probes, each one measuring one of the key quantities of the experiment: current probes, magnetic probes, ion current probe, and time-of-flight probe.

Current probe - In order to detect current pulses we used Pearson probes [46] on two of the seven circuits (typically the first and last ones); only two circuits were monitored both due to the size of those probes, which would not allow a tight packing of the circuits and being two measurements enough
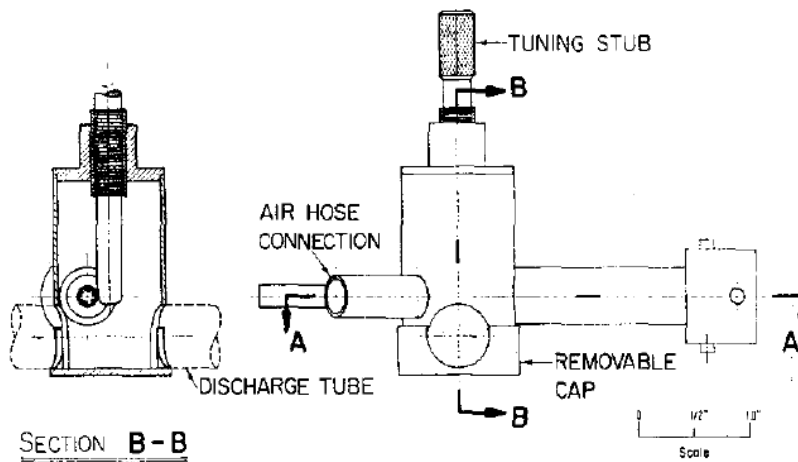
Figure 4.17: Microwave discharge cavity schematic [21].
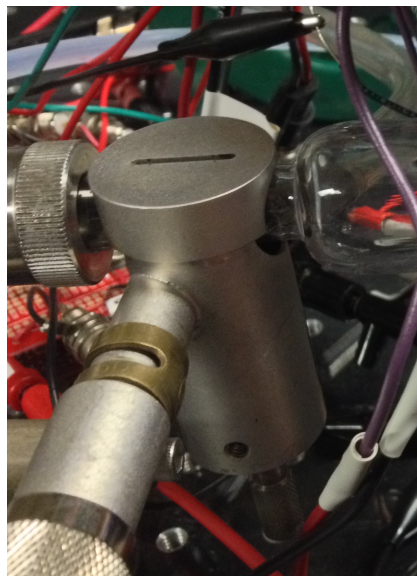
Figure 4.18: Picture of the microwave discharge cavity installed on our apparatus.

to determine if we were producing current pulses with the correct time-delay. The probes used are shown in Figure 4.19.

The probe itself is basically a coil wound arount a toroidal magnetic core, and it is positioned around the wire that carries the current we are interested in measuring. Assuming the field generated by the primary circuit (the wire

Figure 4.19: Pearson probe.
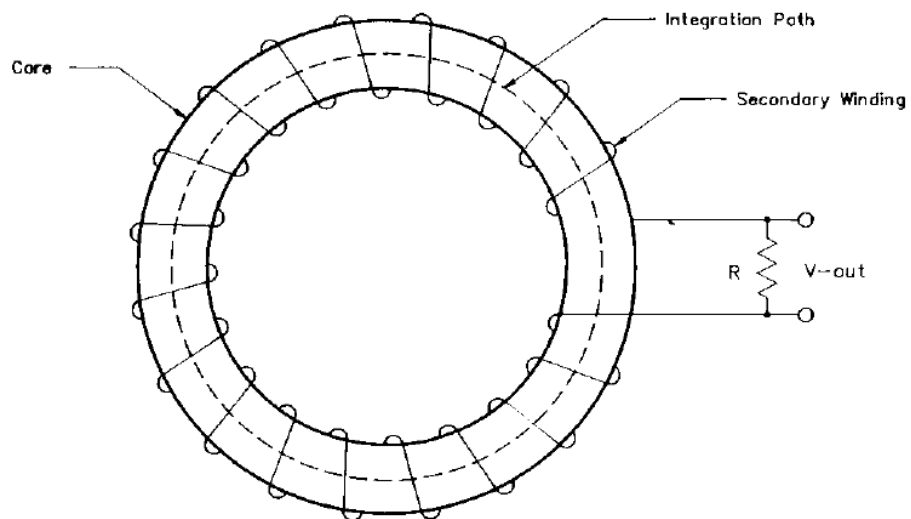
Figure 4.20: Pearson probe schematic [46].

going through the probe) nearly radially symmetrical, from Ampere's Law
we get:

52

$$B = \oint H \cdot dl = I_p - nI_s \tag{4.4}$$

With I_p and I_s being the currents in the primary and secondary circuit (the coil) respectively, and n being the number of turns of the coil. If we integrate around a closed path within the core and assuming uniform magnetic field (true if the cross-section of the core is small with respect to its radius) we obtain:

$$H = \frac{I_p - nI_s}{l} \tag{4.5}$$

Where l is the mean path length around the core. We can then introduce the magnetic permeability $\mu = B/H$, where B is the magnetic flux density inside the core of permeability μ; this allows us to express the magnetic flux ϕ in the core of effective area A as:

$$\phi = BA = \mu HA = \mu A \frac{I_p - nI_s}{l} \tag{4.6}$$

And from Faraday's Law we have:

$$V = I_s R = n\frac{d\phi}{dt} = \frac{n^2 \mu A}{l}\frac{d}{dt}\left(\frac{I_p}{n} - I_s\right) \tag{4.7}$$

What we actually measure with this device is the voltage that is induced by the current of the primary source, which is proportional to the current flowing in the primary source; the proportionality constant varies from model to model, and it depends on the geometrical characteristics of the probe itself. We used both probes with a constant of 10 (to get the current we had to multiply the output voltage of the probe by 10) and probes with a constant of 1 (output voltage of the probe equal to the current in the primary circuit).

Magnetic probe - One of the simplest techniques to obtain magnetic field measurements is to use what is called a B-dot probe. Such probe consists in a coil of wire which is inserted in the region where we want to measure the magnetic field. From Faraday's law, having a changing magnetic flux

through a closed curve craetes an electric field along that curve. In integral it is:

$$V = -\frac{d\phi_B}{dt} \tag{4.8}$$

Where ϕ_B is the magnetic flux and V is the voltage. Having a coil with N loops and radius a, we can express that equation as:

$$V = -\frac{d}{dt}\left(aNB_\perp\right) = -aN\frac{dB_\perp}{dt} \tag{4.9}$$

By measuring the voltage across the leads of the coil one can determine the time derivative of the magnetic field perpendicular to the coil's cross section. It is clear then that in order to obtain the magnetic field an integration procedure is needed, either with an analog integrator circuit or by means of a numerical integration algorithm.

For the purpose of the experiment we built ourselves two identical B-dot probes, in order to be able to detect the translation of the magnetic field. Each probe is made of a 30-turns air core coil of 32 AWG wire, wound with an inner diameter of 1.2 mm. Having such small number of turns gives the probe fast frequency response but also reduced sensitivity, so we had to check if we were able to detect the magnetic field in the accelerator.

A crucial aspect of building B-dot probes is the calibration step. We need to make sure that the readings we obtain from the probes are accurate, and to do that we need to determine the probe calibration constant, that allows us to adjust the measurements to the correct values. The most straightforward way to calibrate the probes is to use them to measure a known magnetic field. A Helmholtz coil is typically used for this purpose, as it generates a uniform magnetic field at its center; however for our case we decided to build an even simpler system, a one-layer 32 turns coil wound around a tube of polymeric material with a diameter of about 6 cm. We decided to go that route since it was much easier to buil than a Helmholtz coil and since it would yield the same type of magnetic field. For the calibration process we followed similar steps as those described in [32]:

1. Power the coil at different levels of DC current and measure the generated magnetic field with a gaussmeter
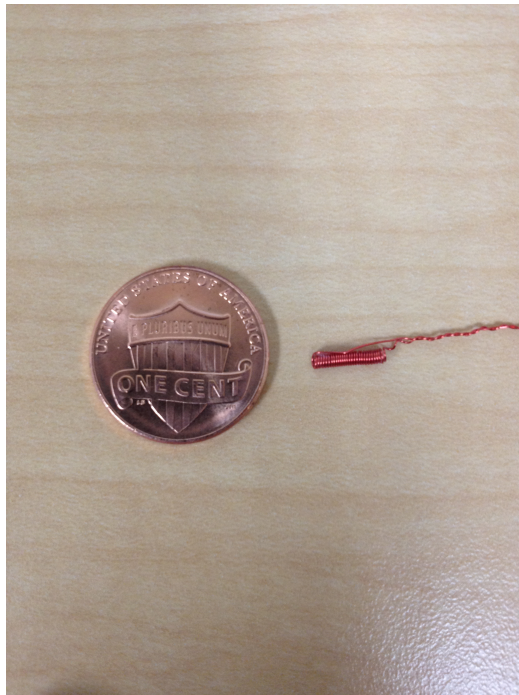
Figure 4.21: B-dot probe coil.

2. Determine the proportionality constant between magnetic field and current for that coil

3. Use the B-dot probe to measure the field generated by a capacitor discharge in the coil and determine the calibration constant by comparison with the expected magnetic field

There is one approximation made in that process: we assumed the constant relating current and magnetic field of the calibration coil to be the same both in the DC regime and in a dynamic regime. Of course that is not entirely true, but for the frequency at which we are operating we can consider that assumption to be valid.

Figure 4.22 shows the results of step 1 and 2; the DC proportionality constant that comes out is equal to 7.37×10^{-4} T/A.

Figures 4.23, 4.24, and 4.25 describe point 3. The calibrated magnetic field shown has an uncertainty of about 10%, however that is not a problem for our purpose since that is representative of a single measurement, while we performed several measurements and averaged the calibration constant values
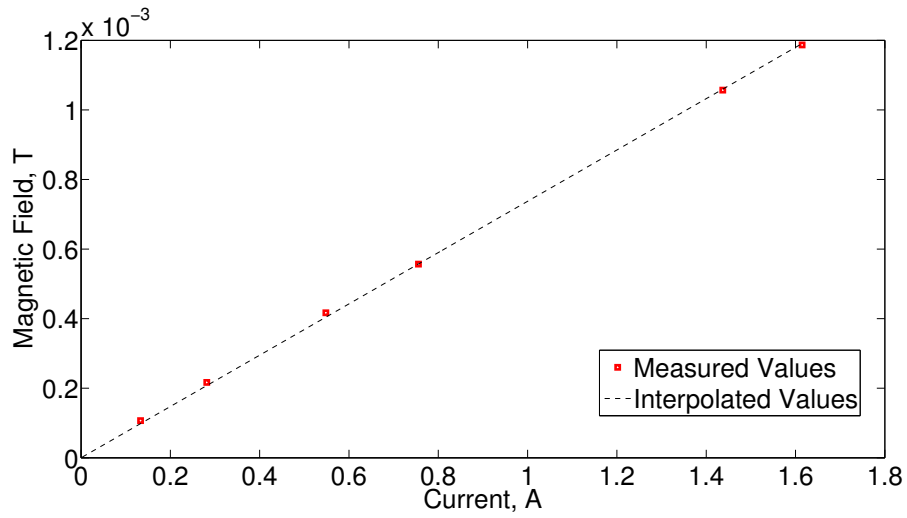
Figure 4.22: DC coil calibration.
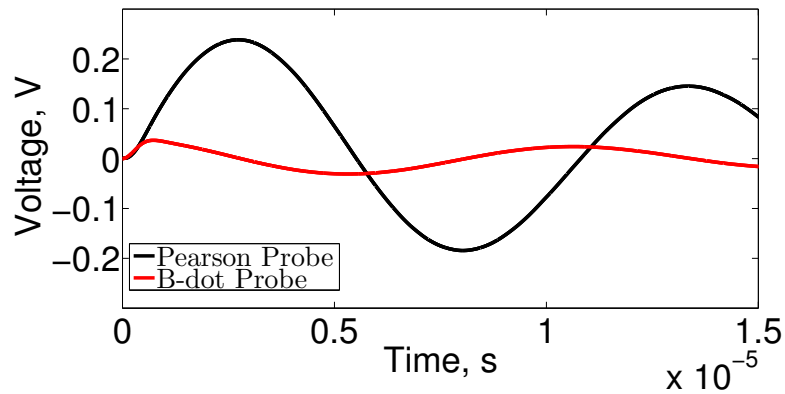
Figure 4.23: Probe voltage.

to get the final one, leading to a more precise calibration. The resulting values of the calibration constants are:

$$K_1 = 3.491 \times 10^4$$

$$K_2 = 3.097 \times 10^4$$

Having those constants, it is enough to multiply them by the magnetic field measured by the respective probe to obtain the actual value of the magnetic field.
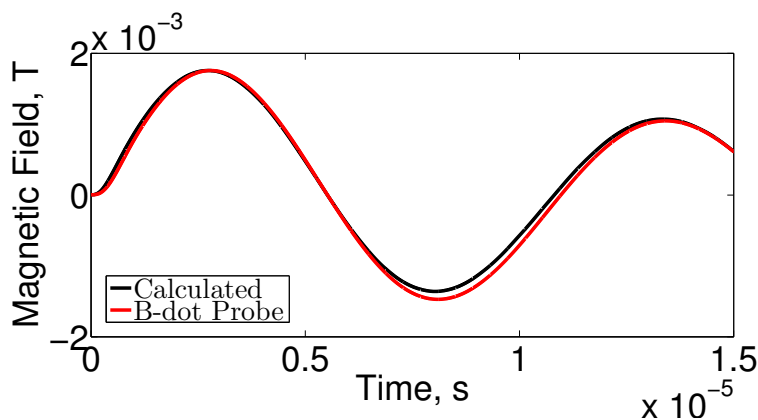
Figure 4.24: Calibrated magnetic field.
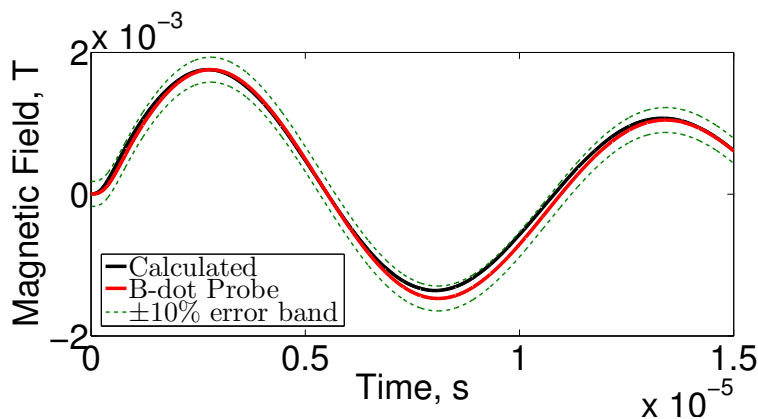
Figure 4.25: Calibrated magnetic field with error band.

Faraday probe - Faraday probes are typically used to measure the ion current density. For our experiment a guarded, planar nude faraday probe has been used. The basic principle behind this kind of probe is relatively simple: both the collector plate and the outer guard are usually biased below plasma potential to ensure electrons are repelled while ions are unaffected. As ions hit the collector, electrons are attracted to neutralize the ion concentration, and that generates a current which is made to flow through a resistor; by measuring the voltage drop across that resistor we can determine such current, thanks to Ohm's law:

$$I = \frac{\Delta V}{R} \tag{4.10}$$

From that one can determine the ion current density.

The implementation of the Faraday probe in our experiment is a bit peculiar.

57

Our purpose was not to use the Faraday probe to actually measure the ion current density, but to detect any effect that could arise from the interaction between the traveling magnetic field and the plasma flow. For that reason we did not bias the probe, instead we left it floating to detect the total plasma current density. The probe was mounted inside the vacuum chamber and pointed directly at the center of the plume; it was mounted on a plate that could be moved by a stepper motor in order to easily move it out of the plasma beam, to determine whether the signal was due to the plasma-magnetic field coupling effect or it was just an electromagnetic interference.
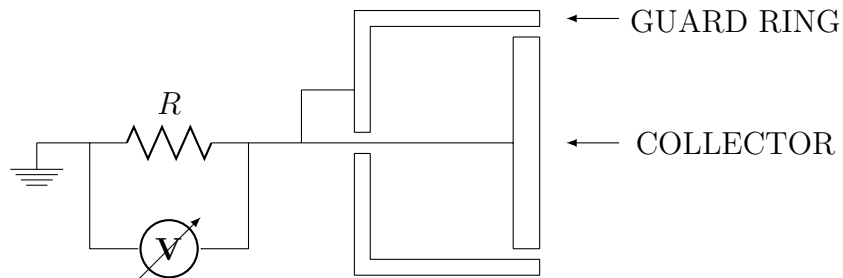
Figure 4.26: Schematic of a Faraday probe.
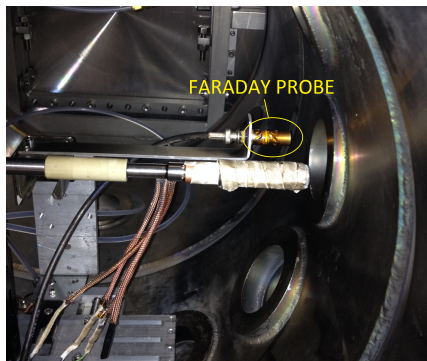
(a) Faraday probe mounted.   (b) Faraday probe.
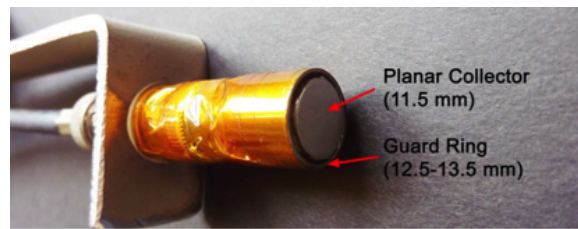
Time-of-flight probe - This probe has been installed in order to detect the velocity of the plasma sheet, allowing us to determine whether the plasma flow experienced an acceleration due to the traveling magnetic wave accelerator. Such probe consists in three copper conductors positioned at a known distance from each other. Two conductors have their tips directly exposed to the plasma flow, while the third one is encased in an allumina tube: that way a current is induced in those conductors as the plasma sheet reaches them. Being at a known distance dx and knowing the time-delay of the two

signals allow for the evaluation of the plasma velocity. The third conductor is instead completely encased in allumina; its presence is necessary to determine if the signal of the exposed conductors is actually due to the interaction with plasma or if it is a product of electromagnetic interference. Ideally the signal coming from the covered conductor should be as small as possible in corrispondence of the peaks of the two uncovered ones; that would mean the obtained signal is totally produced by the propagating plasma sheet. This
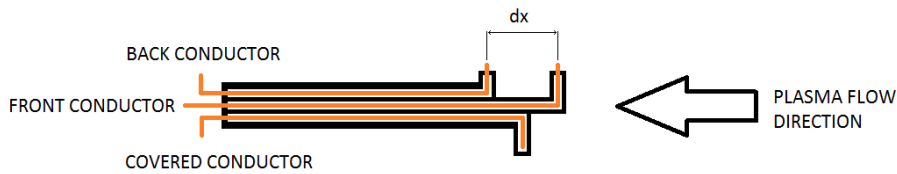
Figure 4.28: Time-of-flight probe simple schematic.

probe has been installed directly in the plume, 4 cm downstream the last coil of the accelerator.
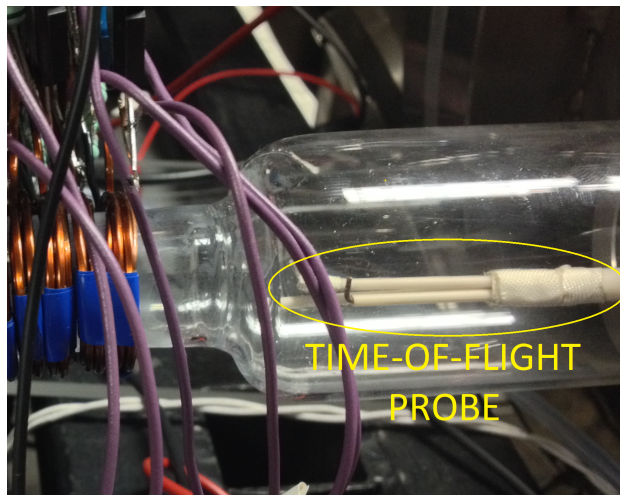
Figure 4.29: Picture of mounted time-of-flight probe.

Chapter 5

Results and Discussion

5.1 Introduction

In this section we will go over all the results that we obtained by performing different tests and measurements on the device, as well as the overall results of the experiment.

5.2 Circuit Characterization

Being the accelerator based on the concept of producing a traveling current pulse (thanks to which a traveling magnetic field is generated), the first measurements that had to be done were current measurements in order to determine if the designed RLC circuit was able to produce a current pulse. Figure 5.1 shows the current pulse that is achieved at different charging voltage. As expected, increasing the voltage at which the capacitors are charged leads to an increase in the current pulse peak; what can also be noted is how the current pulses not only reach higher peak values, but they also become wider, which is an effect that we need to take into account when defining the velocity of the traveling magnetic wave.

Now, if we compare the current pulses with the ideal ones, we can note that there is a difference: first of all, the peak value of the measured pulse is smaller than the ideal one, and the width is larger. All that was expected

(a)

(b)

(c)

(d)
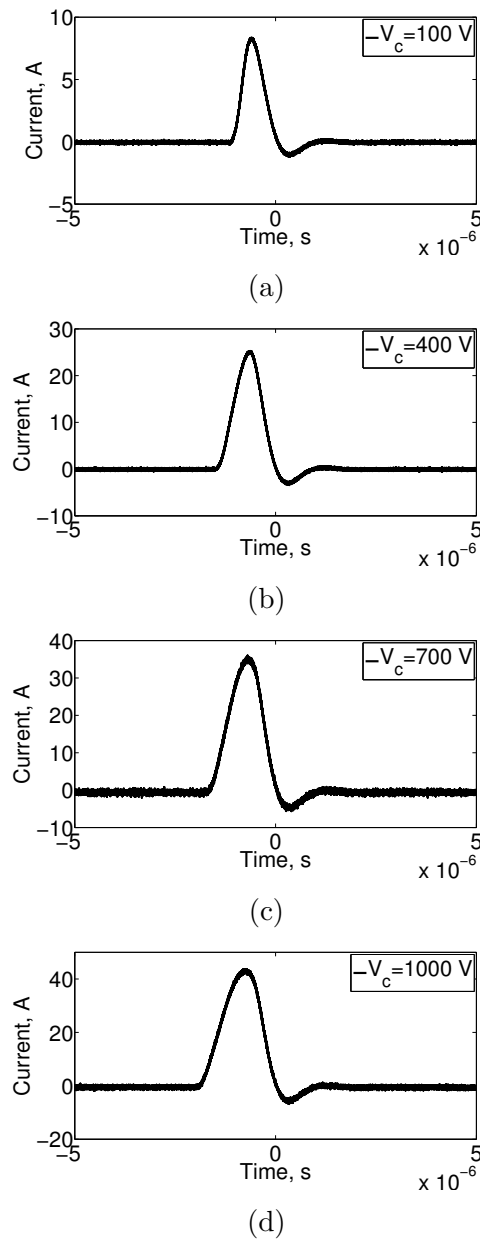
Figure 5.1: Current pulse at different charging voltages: a) 100 V, b) 400 V, c) 700 V, c) 1000 V.

and comes from the fact that in real electrical circuits there are some factors that alter the results we would obtain in the ideal case. In particular, some of those are worth noting:

Time response of components - In the ideal case, we do not take into ac-

count the time response of the components. In our specific situation however, the time scale is so small that those transient periods may not be negligible (in particular, the time it takes a switch or a relay to turn on may not be small enough not to affect the results).

Losses - Unlike ideal electrical components, real ones have some dissipation mechanisms that we cannot control. For example, every part of a circuit has its own resistance (not just the resistors themselves), thus providing some power dissipation.

From the comparison with the ideal case we can thus determine two things: we will not be able to achieve a magnetic field as strong as the one we designed and the velocity at which it travels will probably differ slightly form the designed one. Of course those are negative findings but as mentioned before, they were totally expected due to the nature of the design phase.

That type of measurement has been performed on every single circuit of the accelerator to determine if they were all working as intended.

Another key aspect of the accelerator is the fact that each circuit must generate a current pulse that is time delayed with respect the the previous one. Without that there would be no traveling magnetic field. In order to test that, we measured the current flowing in two circuits as the capacitor discharges were time-delayed by imposing a delay between the two pulses of the pulse generator. The results are shown in Figure 5.2.

Being able to achieve whatever delay we imposed on the pulse generator without it affecting somehow the performance of the circuits means that imposing the velocity of the traveling magnetic field is not a problem. Clearly, the closer the pulses are to each other the faster the magnetic field will travel, but it also means that each coil will have an effect on the system for a larger percentage of the overall traveling time. Those results also go to show how in principle it is easy to tune the delays in such a way to achieve not only a constant velocity traveling field but also an accelerating one.

One more set of current measurements have been done, and they have been carried out on the assembled accelerator. The importance of this kind of measurements is related to the fact that although every circuit is working by itself, once they are all connected together there may be some unwanted connections or unexpected current path that prevent some circuit to operate as expected.

Such measurements (of which Fig. 5.3 is an example) could be carried out with just three circuits analyzed at the same time due to the availability of only three current probes. We had to then perform multiple measurements to check every single circuit in the assembled configuration. Also, this type of measurement has been performed at low voltage (100 V) in order to avoid any possible damage to the more sensitive components (something that
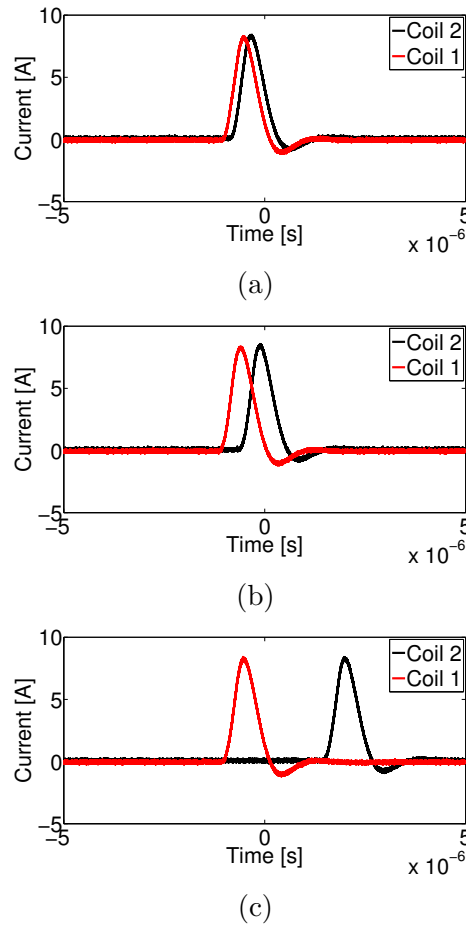
Figure 5.2: Current pulses with different time delays: a) 0.2 µs, b) 0.5 µs, c) 2.5 µs.

happened in other occasions when rising the voltage close to the prescribed limit). Even the single measurement however provided us with some important information: first of all, looking at the time delay between the current peaks we could determine whether it reflected the time delay set on the pulse generator; in the case presented we selected 0.45 µs between two consecutive circuits and we see that there is about 0.9 µs between the measured current peaks, which is exactly what we expect from currents pulses flowing in two circuits that have one circuit in between. The second information that measurement provides us is that although we did not measure currents in circuit 1, 3, and 5 (they were measured later) we are sure those circuits are also working as intended: that because if for some reason one of those circuits were not charging/discharging properly (typically a deterioration of the
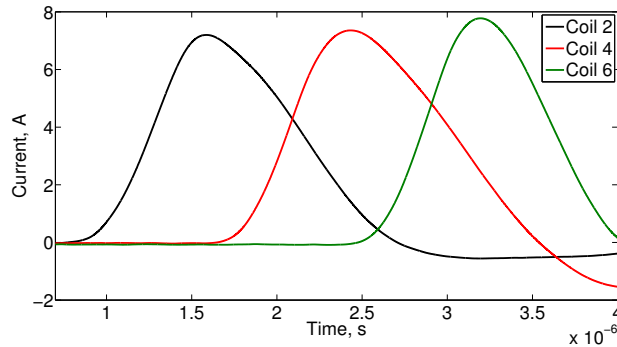
Figure 5.3: Example of current measurement on the assembled accelerator.

MOSFET was the main cause of malfunction), we would not see any current in the following circuits as all the current would flow in the broken circuit (always closed) which presents a much lower impedance than the working ones (open at the time of charging).

Finally, if we compare the current values in the assembled case with the ones of the single circuits we see how in the first case the peaks are smaller and wider with respect to the latter. That can be easily explained by mutual inductance: the magnetic field produced by one coil (A) will induce a current in the coils close to it (B) proportional to the oppposite of the rate of change of the magnetic flux; that current, as the magnetic field rises (current in coil A rising before the peak) is in contrast with the one that is produced by the discharge of the capacitors in coil B, thus leading to a decrease of the current peak. As the magnetic field decreases, instead, the induced current is in the same direction as the one produced by capacitor discharge thus leading to a slower decrease of the current pulse in coil B, yielding a wider pulse overall. Being that effect dependent on the inductance values, for our case it does not yield great changes in the current values, however it is still noticeable especially at high voltages.

5.3 Magnetic Field Characterization

The second key aspect to understand is what kind of magnetic field we can obtain with our setup. What has been done is to simulate the magnetic field generated by a sequence of current pulses derived from the measured ones. In particular, we took the measured current pulses at the operative voltage (800 V) and fit them with a Gaussian curve, which has then been given to

a MatLab script that evaluates the magnetic field with elliptic integrals, the same one used to determine trajectories of ions and electrons.

With the currents shown in Figure 5.4, the resulting magnetic field at different time steps is presented in Figure 5.5.
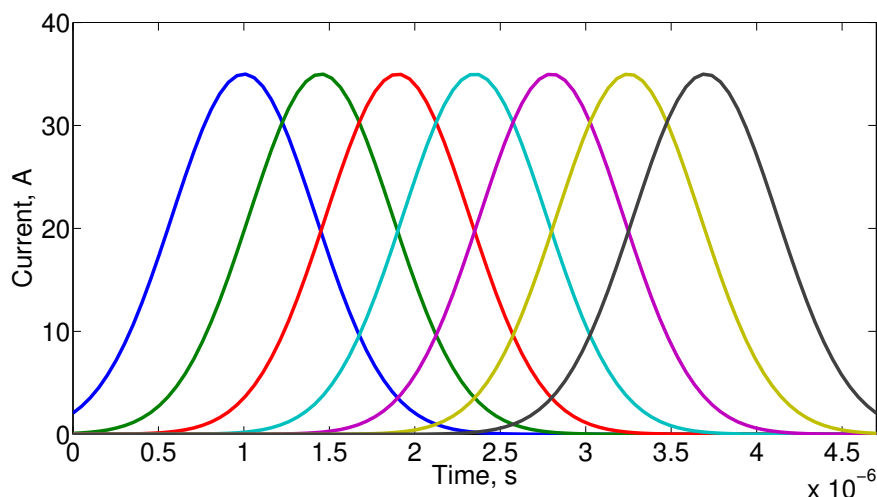
Figure 5.4: Current profiles approximated with Gaussian curves.

The next step was to actually measure the magnetic field produced by the accelerator to see if it is in accordance to what the simulation tells us. To do that we took measurements with a single B-dot probe to be able to reconstruct the spatial profile of the magnetic field. The process that has been followed had various steps. First of all we had to take B-dot probe time-resolved measurements at different positions along the axis of the accelerator; in particular, we took measurements every 3 mm to ensure a good spatial resolution, and for each position we took multiple measurements (at least 5 at every point) to check for the repetability of the phenomenon. We then took all the data and evaluated the magnetic field; that way we had the time-evolution of the magnetic field at every point of measurement. Finally, to get the spatial-evolution we simply looked at what was the value of the magnetic field at the measured points specific time instants, and from that we reconstructed a curve representing the space-profile of the magnetic field at those time instants. The result of such process is shown in Fig. 5.6.

The measurements show how indeed the system is generating a traveling magnetic field; moreover, a comparison with the results of the simulation show how the measurements are in complete accordance with what we were
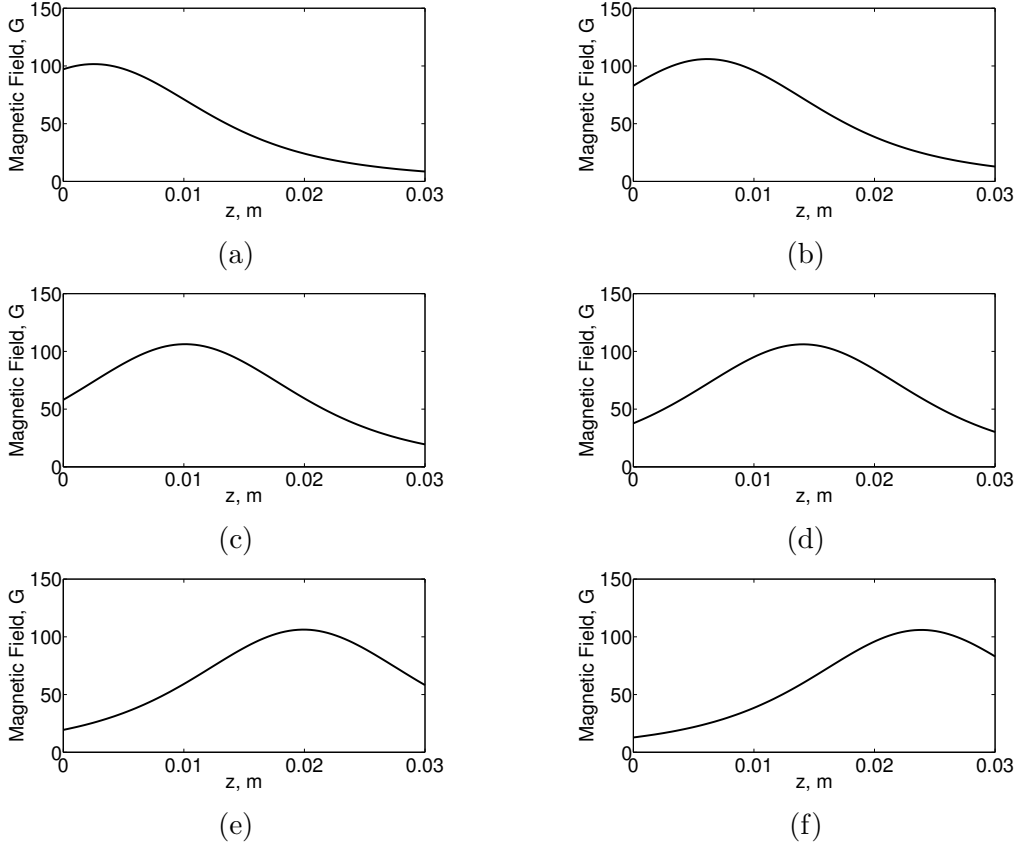
Figure 5.5: 1D magnetic field simulation at different time instants: a) t_0, b) $t_0 + 0.5$ µs, c) $t_0 + 1$ µs, d) $t_0 + 1.5$ µs, e) $t_0 + 2.2$ µs, f) $t_0 + 2.5$ µs.

expecting pretty much under any point of view (magnetic field magnitude, magnetic pulse width, and velocity).

The characterization of the magnetic field however cannot be considered completed without detecting the velocity of the said field. To do that we operated with two B-dot probes by placing them at a known distance and measuring the time-delay between magnetic the field peak at the two positions; knowing the distance between the probes and the time-delay allowed us to compute the velocity. We took measurements with probes at different distances ranging from 3 mm to 2.7 cm, however after manipulating the collected data we realized that when the probes were too close to each other (typically when the distance between them was below 1 cm) the errors in their position were too significant to yield accurate value of velocity. For that reason we only looked at velocity values coming from probes set at over 1 cm apart, which was at least one order of magnitude greater then the positioning errors.
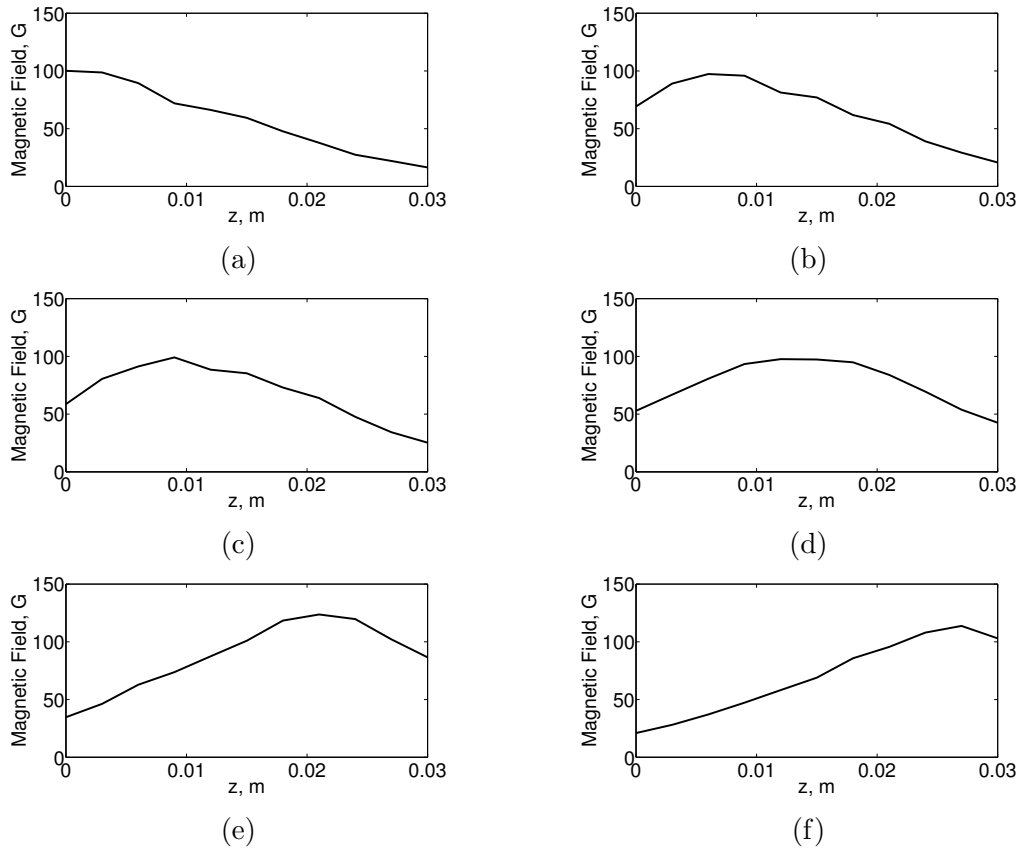
Figure 5.6: 1D magnetic field measurement at different time instants: a) t_0, b) $t_0 + 1.3$ μs, c) $t_0 + 1.5$ μs, d) $t_0 + 1.9$ μs, e) $t_0 + 2.5$ μs, f) $t_0 + 2.9$ μs.

We tested different time-delay between current pulses to determine if the velocity followed that variation as expected.

The results provided us with a clear picture: the magnetic field travels with a constant velocity that increases as the time-delay between current pulses decreses, as expected from the design phase. The measured velocities differ from the theoretical ones by less than 11%, an acceptable discrepancy for our purposes which has roots in the errors on the position of the magnetic probes as well as some fluctuations of the delay between consecutive current pulses.

Magnetic field velocity measurements			
Current time-delay [µs]	Theoretical velocity [m/s]	Measured velocity [m/s]	Percentage error
0.41	12,195	13,432	10.1 %
0.3	16,667	17,240	3.4 %
0.2	25,000	25,111	0.4 %
0.167	29,940	30,516	1.9 %

Table 5.1: Magnetic field data.
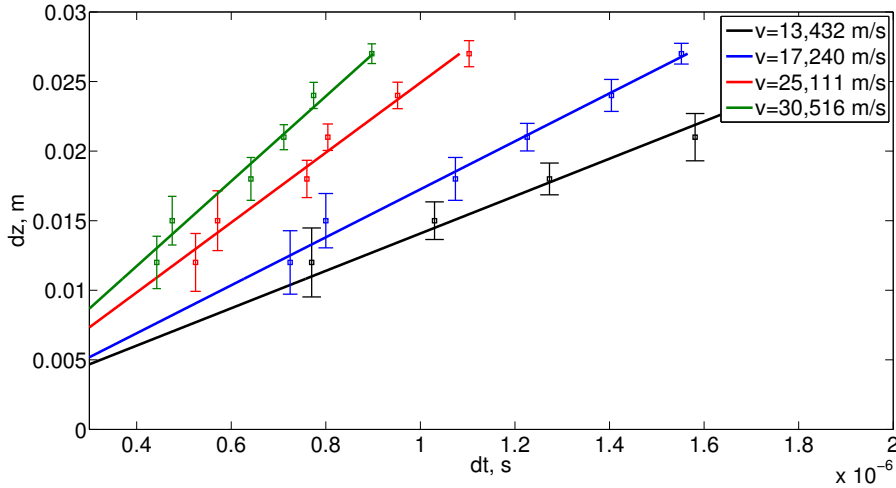
Figure 5.7: Magnetic field velocities.

5.4 Plasma Characterization

After the current and magnetic field tests we moved on to taking some measurements of the plasma flow characteristics with the goal of detecting some kind of interaction between the traveling magnetic field and plasma, and possibly determine, if such interaction is present, whether it leads to an acceleration of the plasma flow. To fulfill those objectives at first we took Faraday probe measurements with the helicon plasma source, and then we moved to the time-of-flight probe with measurements with both plasma sourced.

69

5.4.1 Visual Effect

During the experiment, an effect of the magnetic field could be witnessed visually by looking at the plasma flow, as it appeared to be pulsating as soon as the accelerator was turned on whereas it appeared quiescent when the accelerator was turned off. A video of the event has been captured and different frames have been analyzed.
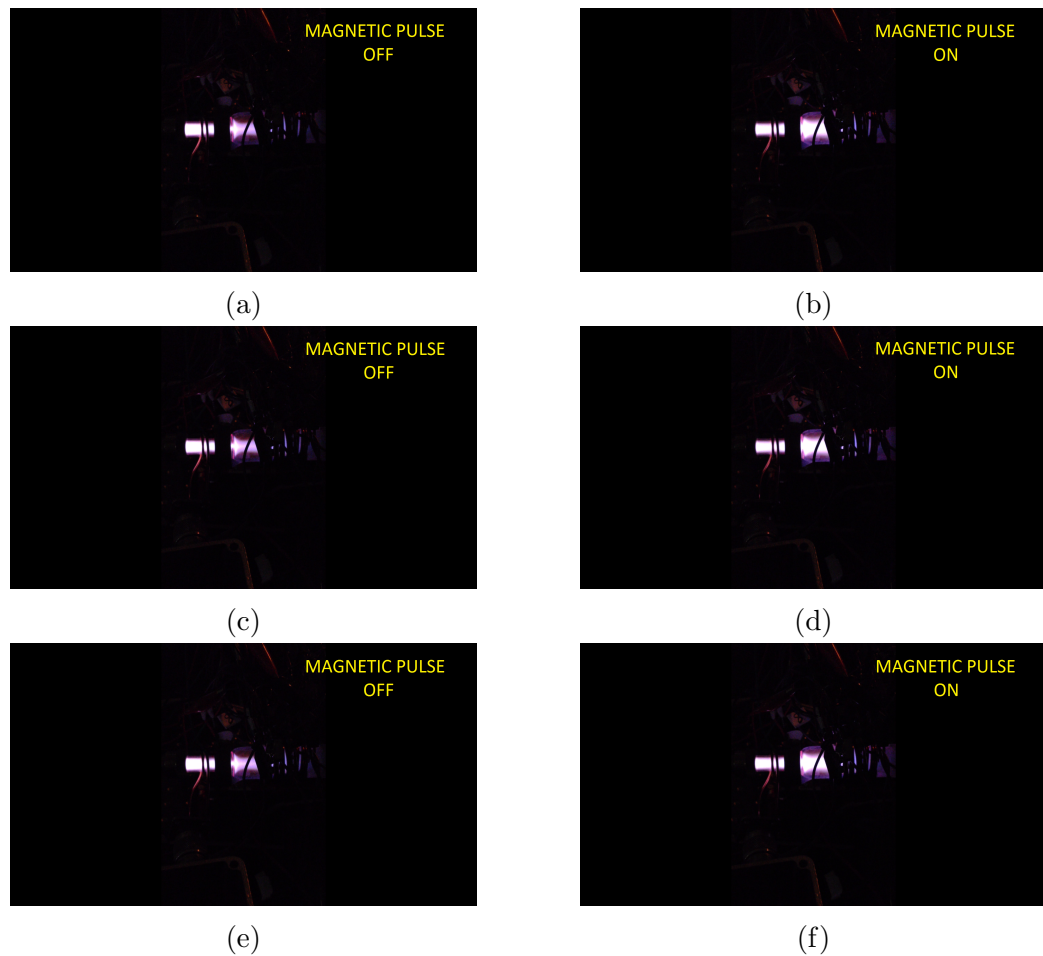
Figure 5.8: Plasma flow at different time instants: a) t_0, b) $t_0 + 0.1$ s, c) $t_0 + 0.2$ s, d) $t_0 + 0.3$ s, e) $t_0 + 0.4$ s, f) $t_0 + 0.5$ s.

It is interesting to note how bursts of more intense plasma flow alternate with less intense flow in correspondence with the discharges of the accelerator; in the example shown in Fig. 5.8 the repetition frequency was set to 5 Hz and indeed the intense plasma bursts occur every 0.2 s.
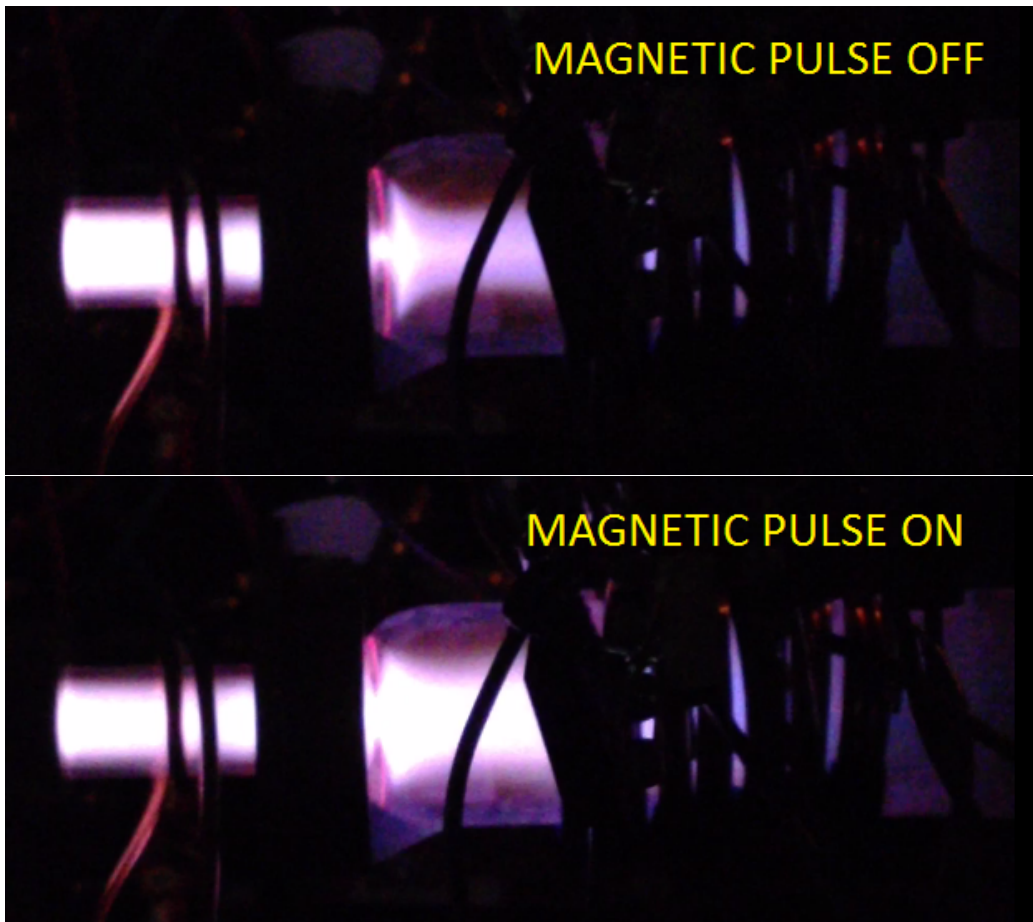
Figure 5.9: Plasma fluctuation details.

A closer look shows how not only the plasma is more intense during the accelerator discharge but also how the exhaust coming from the plasma source follows a more pronounced expansion.

Those findings are purely qualitative and we cannot assess what kind of interaction we were witnessing. The different expansion of the exhaust with and without the accelerator operating might be due to an interaction of the traveling magnetic field with the field produced by the magnetic nozzle, which if altered may lead to an increased expansion of the plasma flow. For what concerns the variation of intensity of the plasma, it may be related to an increased ionization of the propellant. That idea comes after testing the accelerator with the helicon source at different power levels, and findinig how at very low power (less than 0.5 W) having the accelerator operating allowed for a plasma flow to come out from the helicon, whereas the helicon by itself would stop ionizing the propellant at such power levels.
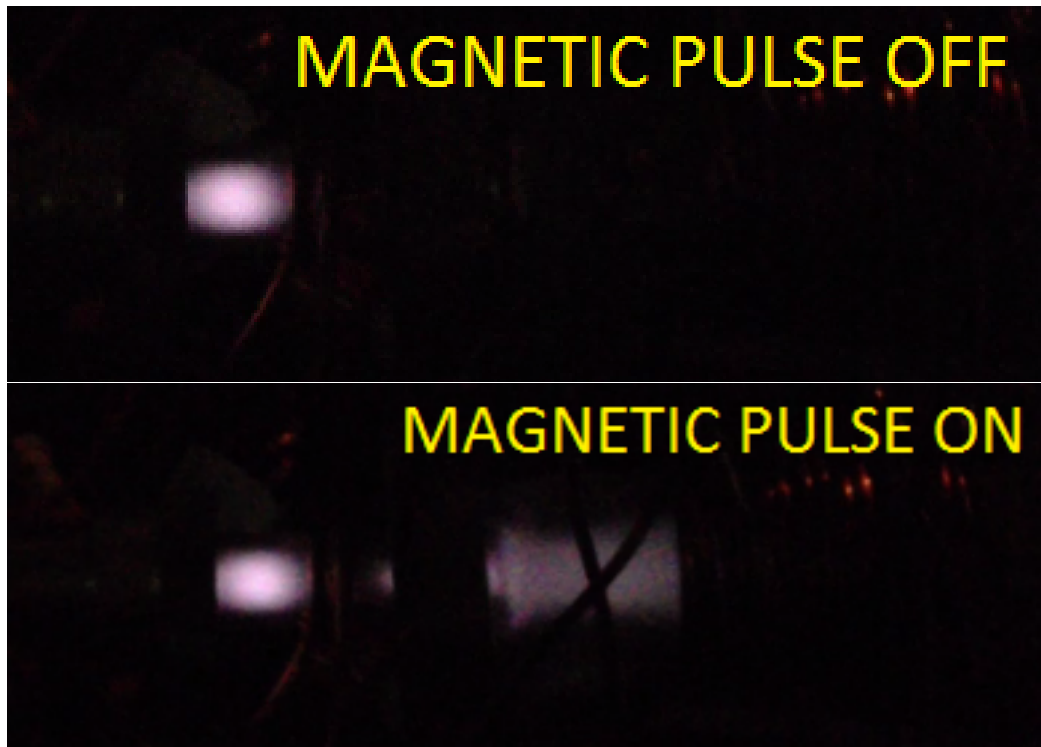
Figure 5.10: Plasma at 0.3 W helicon power.

5.4.2 Faraday probe measurements

The objective of the measurements carried out with the faraday probe was to detect the presence of the interaction between plasma and magnetic field. To do that, we aligned the Faraday probe with the center of the accelerator and placed it within the vacuum chamber, at a distance of about 20 cm from the exit of the accelerator. As previously mentioned, we had it floating to measure the total current.

One type of measurement performed was a long period current acquisition; with that we did not want to detect the single interaction, but rather we wanted to find out if in the current signal we could find the frequency component associated with the repetition frequency of the accelerator discharges. To do that we performed 20 s long acquisitions (so to have a large number of discharges during the acquisition period) at different operative frequencies: 5 Hz, 8 Hz, and 10 Hz. We then took the FFT of the acquired data and we looked for the presence of frequency lines at the previously mentioned frequencies.

We can see that whenever we are operating the accelerator to try to accel-
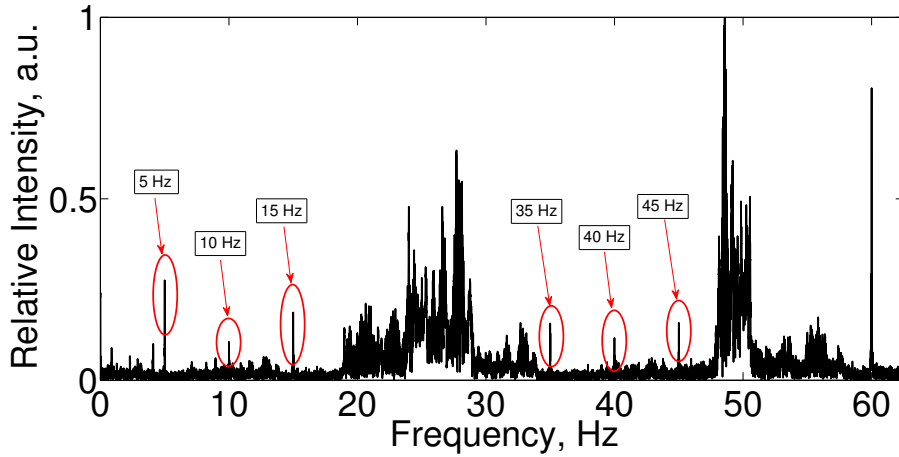
Figure 5.11: FFT of the Faraday probe signal at accelerator repetition frequency of 5 Hz.

erate plasma, the Faraday probe signal contains the repetition frequency of the accelerator, as well as its multiples. Moreover, the change in repetition frequency creates new frequency lines associated to the new frequency while the components associated to the old frequency disappear (or at least their contribution gets reduced by a significant amount). This type of information however is not enough for us, because there might still be an electromagnetic interference between the accelerator and the Faraday probe which is the main source of those frequency components. To avoid any doubt with respect to that we performed two additional acquisitions: one with plasma flowing but with the accelerator off, and the other one with only the accelerator working and no plasma. What came out of those measurements is that when there is absence of either plasma or traveling magnetic field there is no contribution of the repetition frequency to the Faraday probe signal.

So, what this frequency analysis tells us is the following: by containing frequency components associated to the repetition frequency of the accelerator, the plasma current picked up by the Faraday probes shows signs of an interaction between the plasma flow and the traveling magnetic field which has as only plausible explanation a coupling effect between the magnetic field and the ionized gas; electromagnetic interference can be discarded as explanation for the results since that effect is only visible when both plasma and accelerator are on.

In addition to the frequency analysis we took Faraday probe measurements over a smaller time scale to better understand the effect of a single burst of magnetic field. As before, we did not just take measurements with the ac-
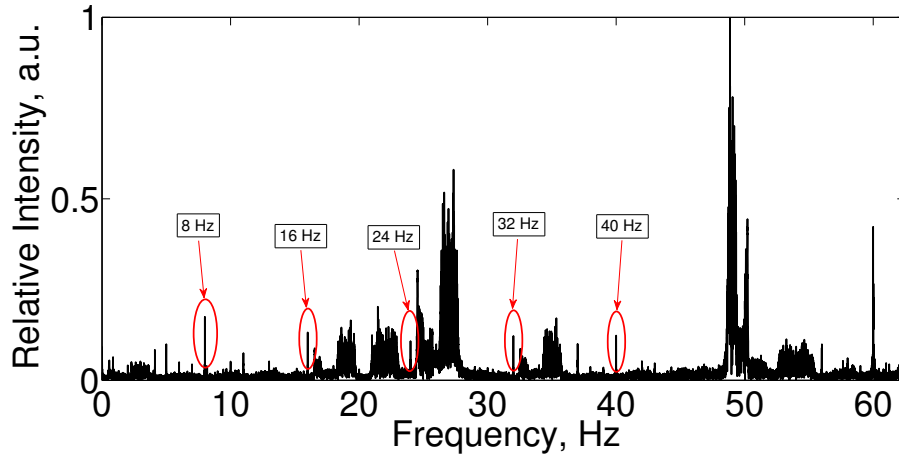
Figure 5.12: FFT of the Faraday probe signal at accelerator repetition frequency of 8 Hz.
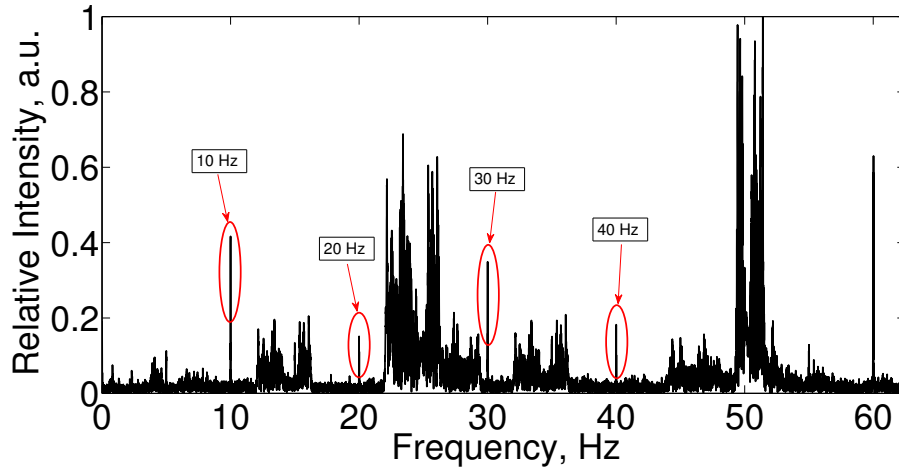
Figure 5.13: FFT of the Faraday probe signal at accelerator repetition frequency of 10 Hz.

celerator interacting with plasma, we also checked for electromagnetic noise by both looking at the signal from the probe positioned outside the plasma plume and looking at the signal with the accelerator not operating.

Although in this case we can see the presence of some electromagnetic noise, it is definitely not the reason behind the signal with both plasma and accelerator working as in that case the current spike is about 10 times greater than the interference signal. The signal with the accelerator off only shows the oscilloscope baseline, as it should be since it comes form a uniform plasma

74
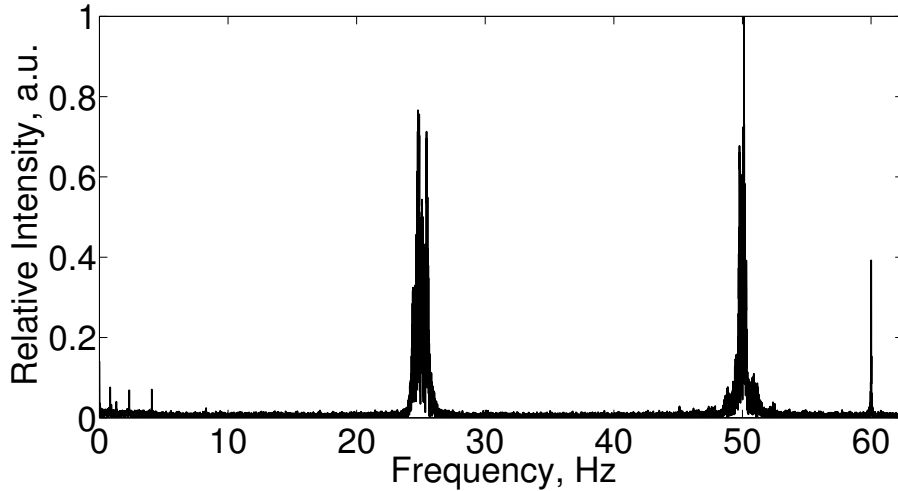
Figure 5.14: FFT of the Faraday probe signal with plasma on but accelerator off.

flow.

Again the Faraday probe measurements show how there is an interaction between the traveling magnetic field and plasma, however we did not get any information about the plasma velocity; in theory, as we know the distance from last coil and the Faraday probe, measuring the time at which the probe signal reaches its maximum should allow us to determine the plasma velocity. In our case such procedure yields velocity values that are not in accordance with the traveling magnetic field velocity. For that reason Faraday probe measurements do not provide any useful information about wheter the magnetic field acts to accelerate plasma or the interaction we see is of a different kind. One possible explanation for the velocity results lies in the time response of the probe-oscilloscope system, which could have been too large to allow detection of a phenomenon as fast as ours (the system response was in the order of 10^{-4} s while the detection should have occurred in the 10^{-5} s range). One problem we encountered while taking Faraday probe measurements with the helicon plasma source was noise; we had not only a strong 40 MHz noise, related to the RF antenna working frequency, but on longer aquisition times (in the tens of millisecond range) we had a 60 Hz noise coming directly from the power supply. To attenuate the RF noise we had to apply a low-pass filter to the measurements, and whenever the 60 Hz signal was showing we had to subtract the corresponding sinusoid to get a cleaner voltage profile.
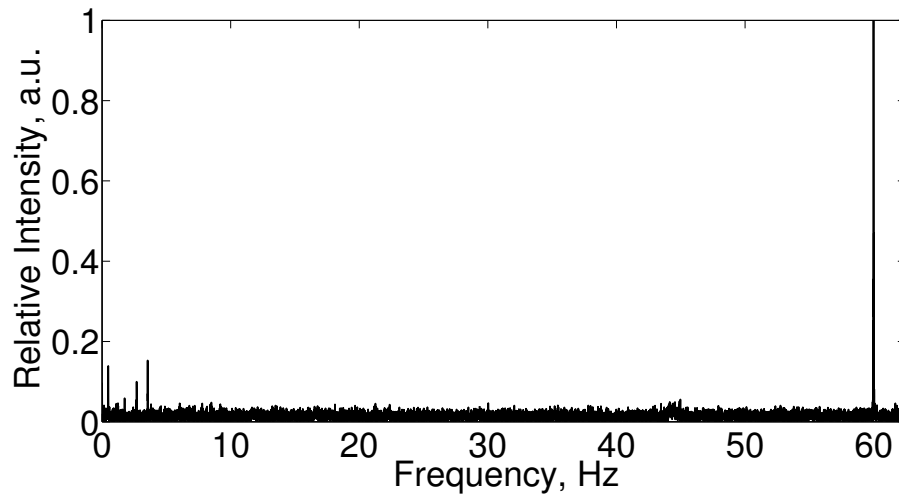
Figure 5.15: FFT of the Faraday probe signal at accelerator repetition frequency of 5 Hz but plasma off.
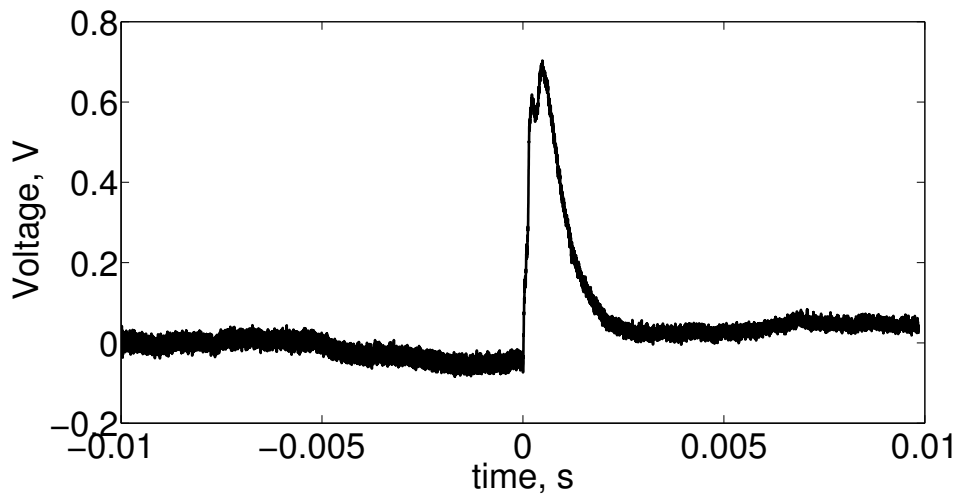
Figure 5.16: Faraday probe signal with accelerator charged at 800 V.

5.4.3 Time-of-flight measurements

In an attempt to confirm the interaction shown by the Faraday probe and to get more information about the plasma velocity we went on to take measurements with the time of flight probe. Such device has been positioned much closer to the accelerator than the Faraday probe (it has been placed at about 4 cm from the last coil, still along the axis of the accelerator) because
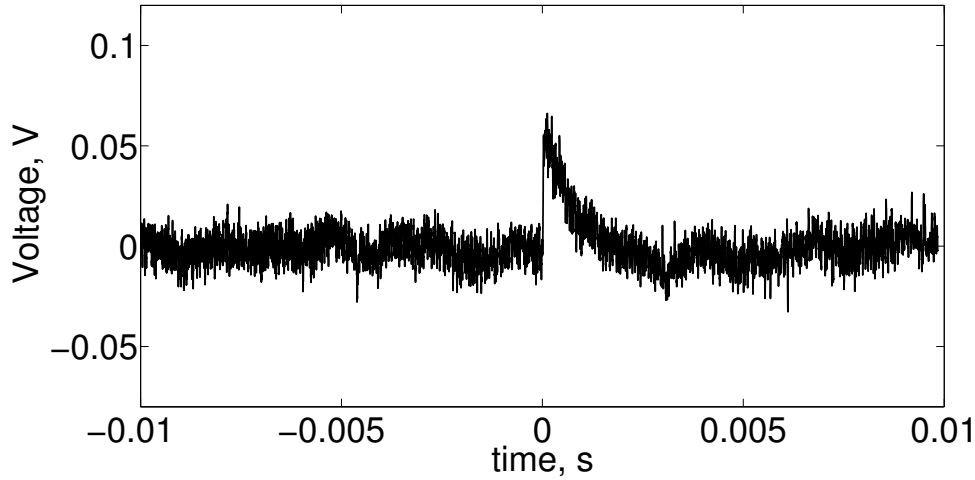
Figure 5.17: Faraday probe signal with probe outside the plume.

it needed to interact with stronger plasma flow to yield readable voltage (and thus current) levels.

Time-of-flight with helicon - We performed time-of-flight measurements with both helicon and microwave plasma sources, to check for any possible difference and because the microwave source produced cleaner results, being less noisy.

With plasma produced by the helicon thruster, we took data at different accelerator charge voltages as well as different helicon power levels to understand how those parameters influenced the interaction between plasma and the traveling magnetic field. It is interesting to note how at low helicon power regimes (5 W in our case) the time-of-flight signal shows two peaks: the first peak, although stronger in magnitude, seem to be a consequence of electromagnetic interference, as the voltage from the covered conductor peaks with a maximum value comparable with the signals from the other two conductors. The second peak however seems to be entirely a consequence of plasma interaction, as there is no current produced in the noise detecting electrode, thus meaning electromagnetic interference has no contribution to that signal peak. As expected, increasing the charging voltage yields to an increase in the maximum measured voltage values; that could simply be due to the fact that higher charging voltage means higher electromagnetic interference detected (first peak magnitude increases) and stronger magnetic field generated, which in turn should make the interaction with plasma more intense and thus a stronger second voltage peak.

The presence of the second peak is also important to determine that even
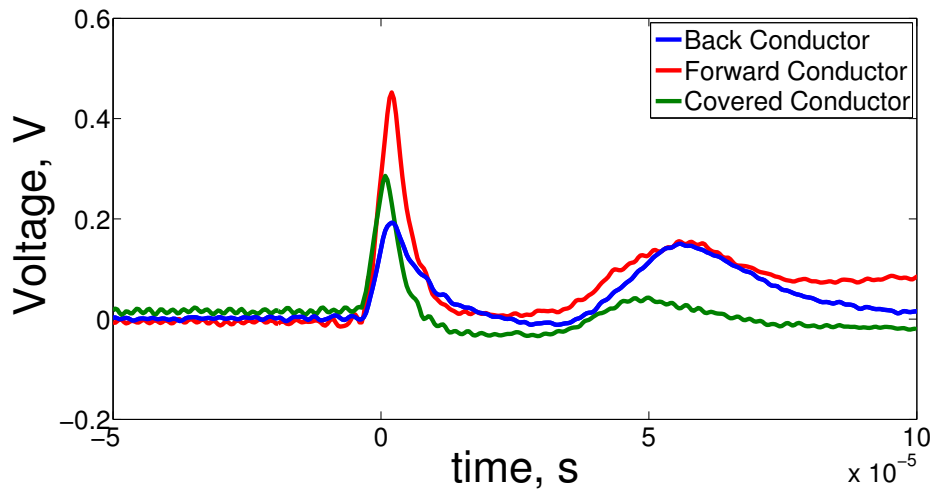
Figure 5.18: Time-of-flight measurements at accelerator charging voltage of 300 V and helicon power of 5 W.
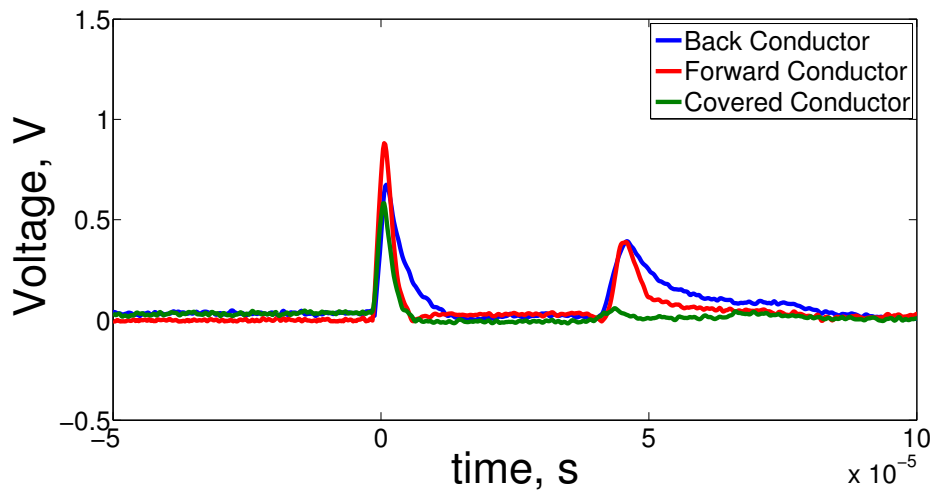
Figure 5.19: Time-of-flight measurements at accelerator charging voltage of 600 V and helicon power of 5 W.

with a type of measurement that is different from that of the Faraday probe we are still detecting an interaction that can only be explained by assuming some coupling between plasma and magnetic field generated by te acceler- ator. Unfortunately even with this kind of probe the measurements do not yield any sort of information regarding the velocity of the plasma that inter- acted with the magnetic field; in fact, the peak from the conductor closer to
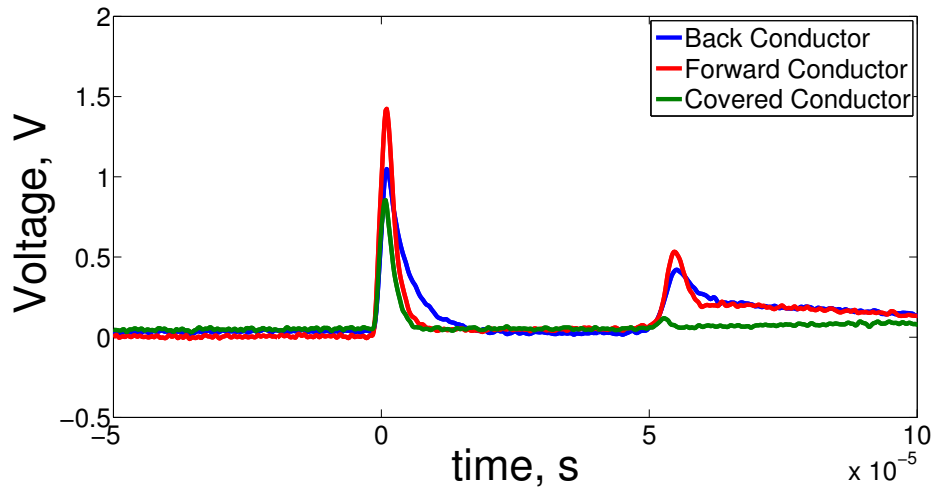
Figure 5.20: Time-of-flight measurements at accelerator charging voltage of 800 V and helicon power of 5 W.

the accelerator occurs simultaneusly with the peak from the farther conductor.
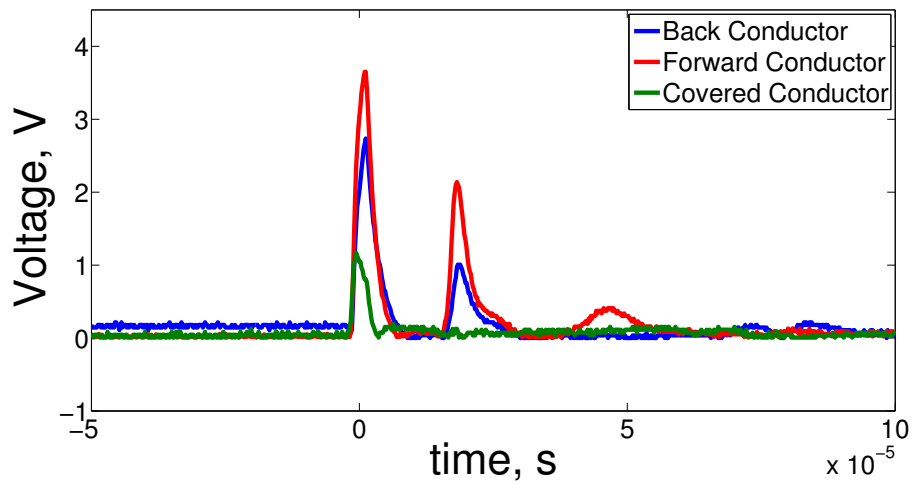
Figure 5.21: Time-of-flight measurements at accelerator charging voltage of 800 V and helicon power of 10 W.

Looking at measurements done at different helicon power levels the signals maintain the same characteristics as the ones at low power. At higher power (10, 15, and 20 W) however electromagnetic interference do not seem to play a fundamental role in the generation of the first peak; although still present,
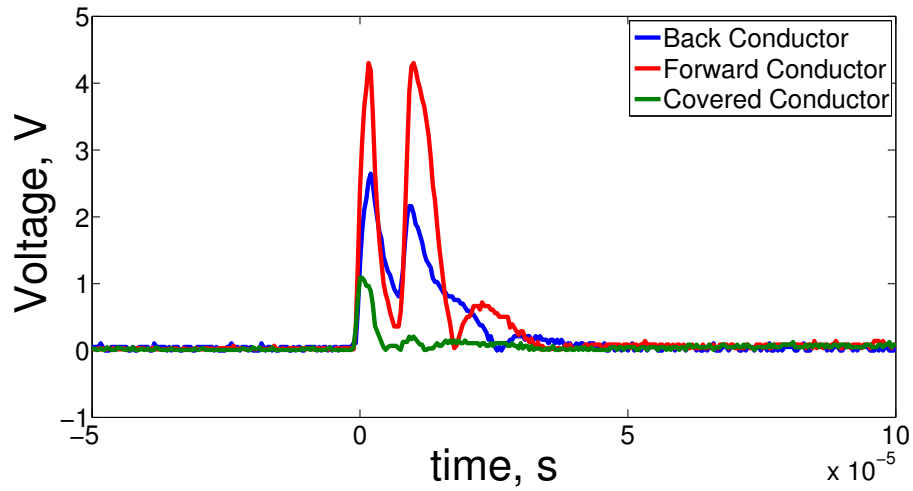
Figure 5.22: Time-of-flight measurements at accelerator charging voltage of 800 V and helicon power of 15 W.
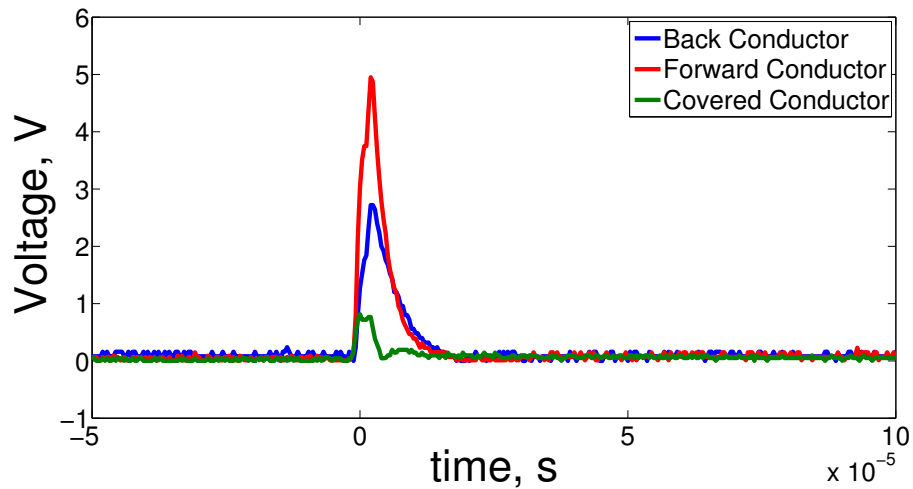
Figure 5.23: Time-of-flight measurements at accelerator charging voltage of 800 V and helicon power of 20 W.

it seems that what the probe measures is an effect that is in part due to interference and in part due to the plasma-magnetic field interaction. The second peak, when present, is noise-free as before. Another difference is in how the signals change by changing the power level with respect to how they change when changing the accelerator voltage. Again, the magnitude of the peaks increases by increasing the plasma source power (mostly due to

Time-of-flight parameters (microwave plasma source)			
Chamber pressure [Torr]	Power [W]		Magnetic field velocity tested [m/s]
	Forward	Reflected	
0.20	85	84	12,019
0.20	80	70	12,019
0.20	75	50	12,019
0.35	75	40	8,333 ; 12,019 ; 25,000
0.30	75	32	8,333 ; 12,019 ; 25,000
0.25	75	30	8,333 ; 12,019 ; 25,000
0.20	75	30	8,333 ; 12,019 ; 25,000

Table 5.2: Time-of-flight measurement parameters with microwave plasma source.

the plasma produced being more intense and thus the interaction with the magnetic field is stronger), but we also see how the second peak gets closer to the first one and eventually the two voltage peaks merge together. All those measurements have been performed at a vacuum chamber pressure of 5×10^{-5} Torr, with the base pressure (with setup not running) being 5×10^{-6} Torr.

Time-of-flight with microwave cavity - After all those measurements performed with the helicon thruster we moved to a microwave discharge cavity; that was done to check if changing plasma source would make any difference on the time-of-flight signal and to see if the more intense plasma generated by the microwave cavity (consequence of higher input power) would produce better results in terms of the possibility of detecting a plasma acceleration.

This time we did something different: again we took measurements at different plasma source power levels, but then instead of looking at how the accelerator voltage influenced the time-of-flight data we looked at how different mass flow rates and different traveling magnetic field velocities have an impact to the signal produced by the probe. All the measurements have been done at the maximum accelerator voltage of 800 V. A recap of other parameters are provided in Tab. 5.4.3.

We can see how the effect of increasing the power avilable to the microwave cavity is the same as that of increasing the helicon power: the signal from the probe increases as consequence of more intense plasma interacting with the magnetic field. Moreover, it looks like only the data coming from the measurement at 10 W microwave power could give us information on plasma
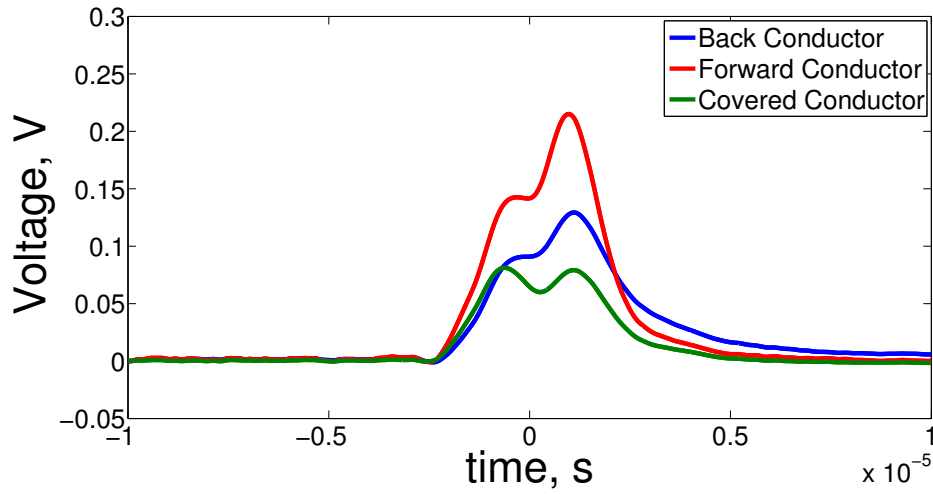
Figure 5.24: Time-of-flight measurements at microwave power of 1 W.
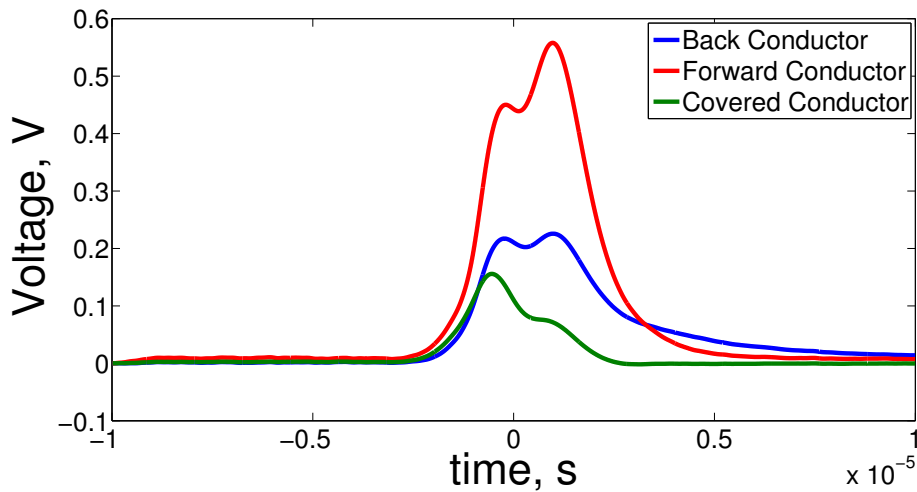
Figure 5.25: Time-of-flight measurements at microwave power of 3 W.

velocity. Looking at the time delay between the forward and back conductor peaks (1.79 µs) the resulting velocity is 8,165 m/s, which is 60% of the magnetic field velocity measured in the same accelerator configuration; that is a plausible result considering that although the plasma can accelerate from a negligible velocity to a maximum velocity equal to that of the traveling magnetic field, that does not mean a complete acceleration must be obtained. The non-repeatability of that result however does not necessarily make it reliable for determining the plasma velocity. One thing to note is the difference
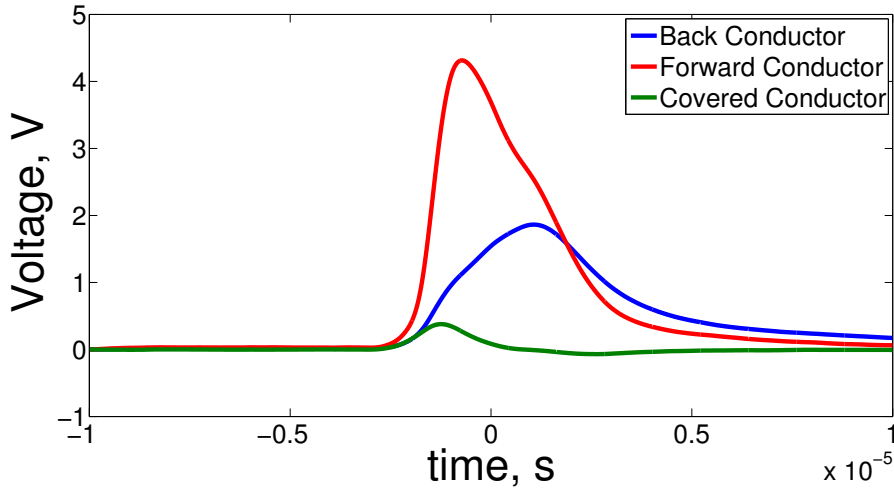
Figure 5.26: Time-of-flight measurements at microwave power of 10 W.
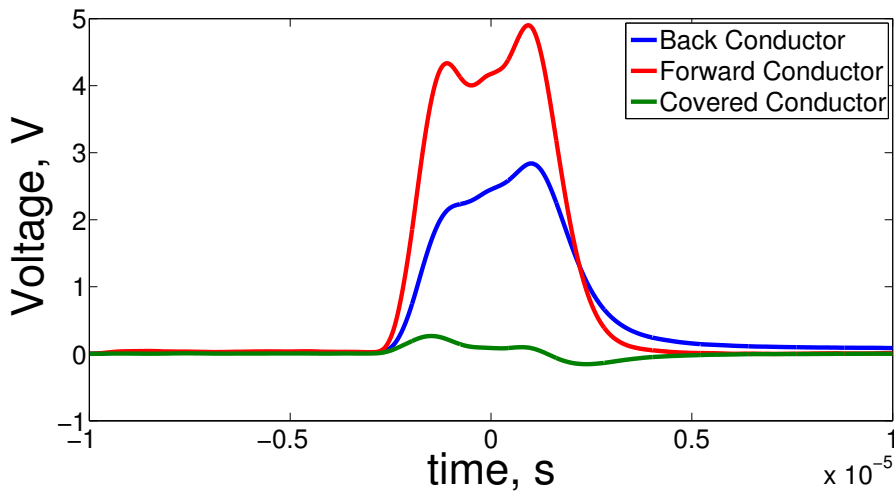
Figure 5.27: Time-of-flight measurements at microwave power of 25 W.

in magnitude of the signals coming from the non-covered conductors. The explanation of the fact that the forward conductor produces a stronger signal than the back one comes from their position: they lie on the same plane, and that may cause the conductor close to the accelerator to cast some sort of shadow on the farther one, leading to the generation of a smaller signal.

In the following analysis we report the effect of the mass flow rate on the time of flight traces. In particular, the mass flow rate affects the neutral pressure inside the plasma source, which in turn determines electron-neutral
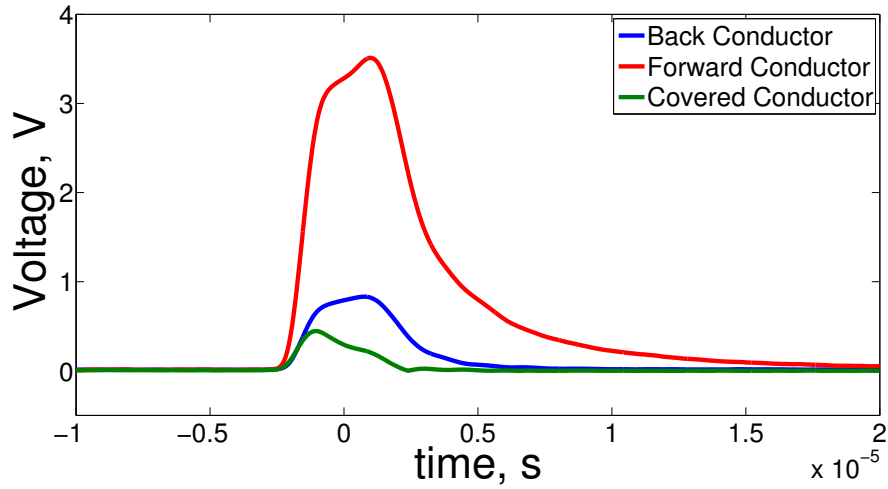
Figure 5.28: Time-of-flight measurements at traveling magnetic field velocity of 12,019 m/s and chamber pressure of 0.2 mTorr.
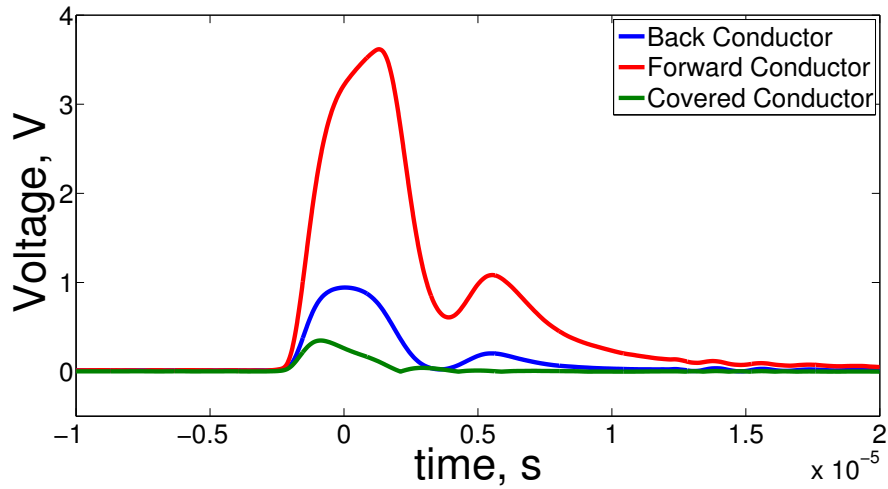
Figure 5.29: Time-of-flight measurements at traveling magnetic field velocity of 12,019 m/s and chamber pressure of 0.25 mTorr.

collisionality, ionization and excitation rates and elasic colliosional losses. In the following th text we will refer to the pressure instead of the mass flow rate.

Knowing that the base pressure achieved the day of the test was 3.5×10^{-5} Torr, the higher the pressure is with respect to that value the higher the argon mass flow rate is flowing in the system. We can see how at low mass
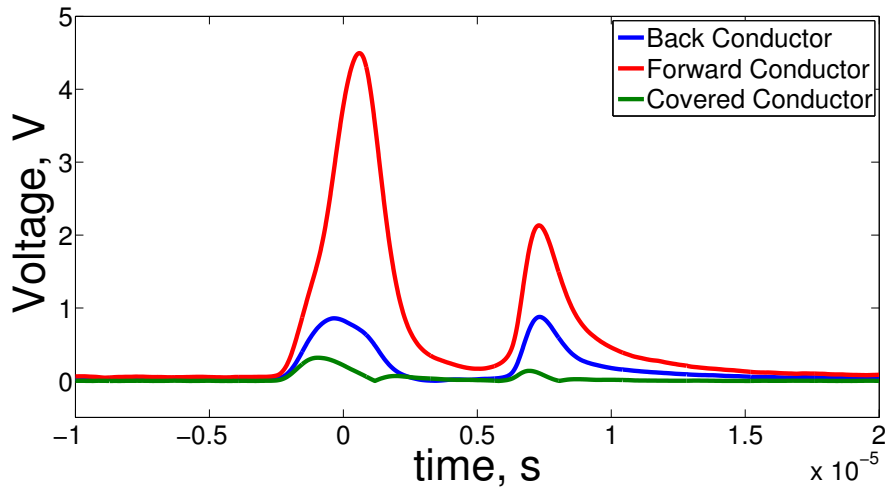
Figure 5.30: Time-of-flight measurements at traveling magnetic field velocity of 12,019 m/s and chamber pressure of 0.3 mTorr.
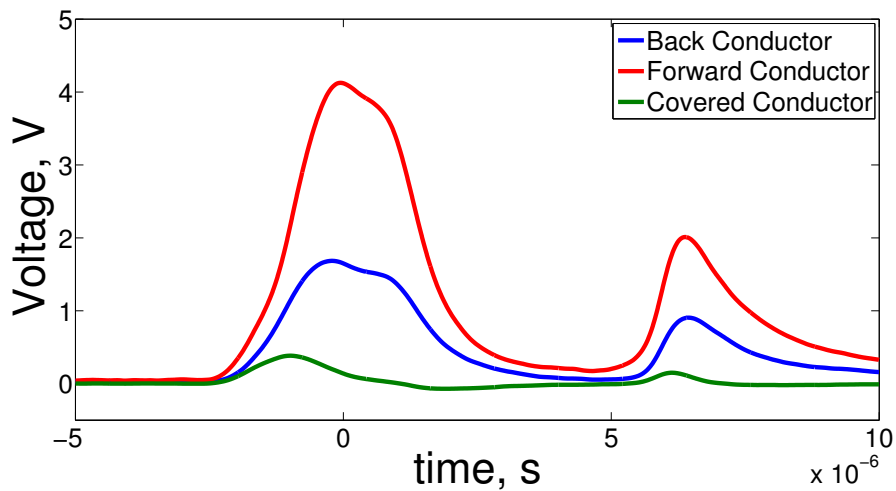
Figure 5.31: Time-of-flight measurements at traveling magnetic field velocity of 12,019 m/s and chamber pressure of 0.35 mTorr.

flow rates there is only a single peak generated by the time-of-flight probe, whereas increasing it leads to two peaks that seem to move farther away from each other.

Taking time-of-flight measurements after setting the accelerator currents time-delays to produce different magnetic field velocities gives us a set of very interesting data. As we can see, a variation in the traveling magnetic
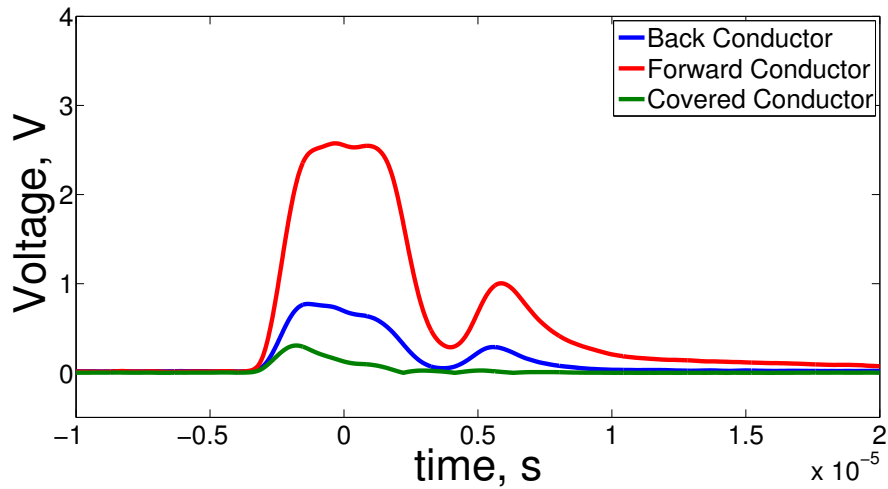
Figure 5.32: Time-of-flight measurements at traveling magnetic field velocity of 8,333 m/s.
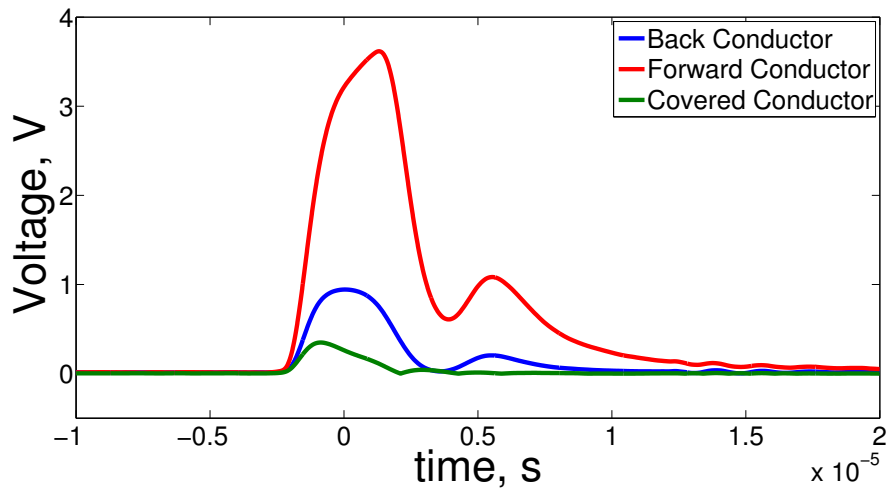
Figure 5.33: Time-of-flight measurements at traveling magnetic field velocity of 12,019 m/s.

field velocity produces a time-of-flight trace with variable width: the lower the velocity the wider the pulse produced by the probe is. A possible explanation ot that phenomenon lies in the fact that to achieve lower magnetic field velocities we need to increase the time delay between consecutive current pulses, and that increases the time it takes to achieve a single complete discharge of the accelerator; that would allow the traveling magnetic field to
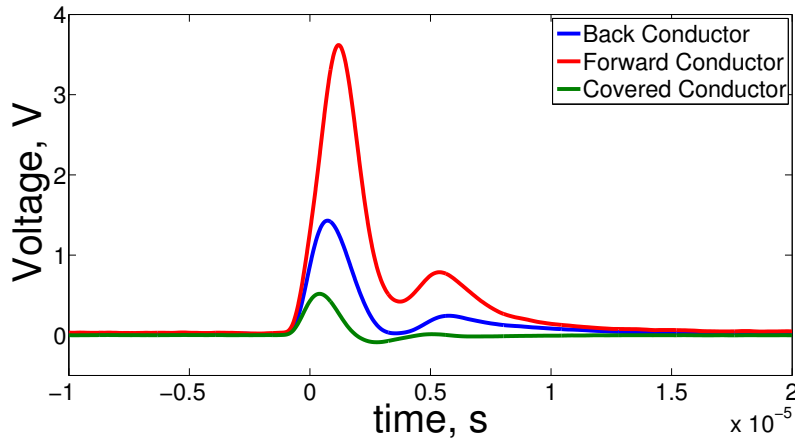
Figure 5.34: Time-of-flight measurements at traveling magnetic field velocity of 25,000 m/s.

interact with a larger portion of plasma (since it is constantly produced by the plasma source) which then interacts with the probe for a longer time. Also note the presence of a small signal from the covered conductor, sign that electromagnetic interference is non-zero, however its intensity leads us to believe it is not the main cause of the probe signal, considering that no such phenomenon occurs when either plasma or accelerator are not operating. In fact,the data without plasma shows the electromagnetic interference contribution to the signal, which is of an order of magnitude smaller than any signal coming from the plasma-magnetic field interaction.
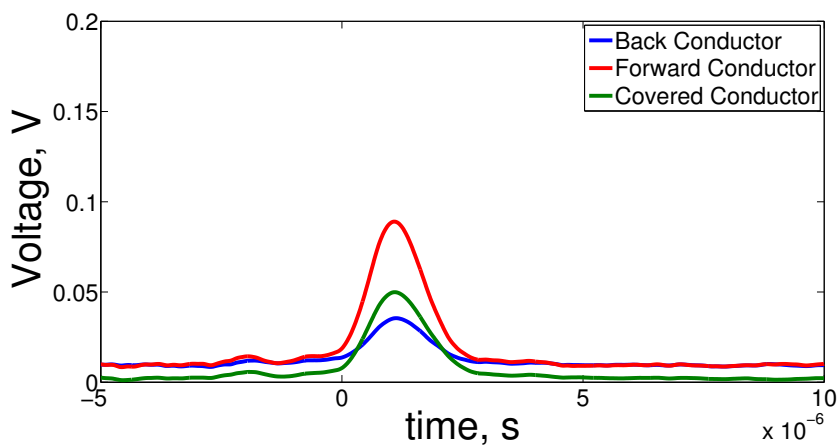
Figure 5.35: Time-of-flight measurements without plasma.

Chapter 6

Conclusion and Future Work

The developement of an electrodeless plasma accelerator based on the principle of traveling magnetic field has been discussed. Such system would theoretically be capable of accelerating a plasma flow up to the same velocity as that of the magnetic field, with all the advantage that an electrodeless system has with respect to more traditional technologies.

A theoretical background has been presented with both a more classical theory that explain the basics of this technology and some new ideas that try to better explain the interaction between plasma and electromagnetic field and how it should lead to an acceleration of the first. After that, the design phase of a compact, low power traveling magnetic field accelerator has been described, with multiple ways to produce such kind of effect presented. Then, in order to test the capabilities of such system to accelerate a plasma flow we built a proof of concept of it and we described all the components used along with the set values for the parameters and a description of the overall apparatus utilized. Finally we presented the results obtained from a different range of measurements performed with different probes in different conditions.

Overall we were able to satisfy the constraints we imposed ourself on the size/aspect ratio of the accelerator (which was just 3.5 cm long with a length-to-diameter aspect ratio of 1.4) and on the power consumption (which at 10 Hz was about 1 W); we were able to detect the generation of a traveling magnetic field and measure its velocity. Once operating coupled to a plasma source, we were able to detect an interaction between the magnetic field and the plasma flow, interaction that was dependant on various parameters such as plasma source power level, propellant mass flow rate, accelerator charging

voltage, and magnetic field velocity. We established such interaction could not be simply explained by electromagnetic noise, thus leading us to the conclusion that some coupling between plasma and the traveling magnetic field occurred.

All those measurements unfortunately did not provide us with uniform values for the plasma velocity; for that reason we cannot asses this effect originates from a magnetic piston phenomenon, which is the speculated working principle of the device.

The results obtained are however promising, and in the future different measurements techniques could be implemented, such as energy analyzers, Laser-Induced-Fluorescence (LIF), or magnetic probes inside the plasma flow, along with different operating conditions and different primary ionization stages. This wide array of diagnostic systems will allow us to provide a final assessment on this innovative propulsion concept.

From the work presented in this thesis a paper which will be presented during the poster session of the 2015 IEPC conference has been written. Such paper is presented in Appendix A.

Acronyms, Symbols, and Constants

Acronyms

I_{sp}	Specific Impulse
PIT	Pulsed Inductive Thruster
RLC	Resistance, Inductance, Capacitance
$MOSFET$	Metal Oxide Semiconductor Field Effect Transistor
DC	Direct Current
RF	Radio Frequency
LIF	Laser Induced Fluorescence
$SPPL$	Stanford Plasma Physics Laboratory
PIC	Particle-In-Cell
TMW	Traveling Magnetic Wave
AC	Alternate Current
LC	Inductance, Capacitance
TTL	Transistor-Transistor Logic
BNC	Bayonet Neill–Concelman
$VASIMR$	Variable Specific Impulse Magnetoplasma Rocket
$FARAD$	Faraday Acceleration with Radio-Frequency Assisted Discharge
AWG	American Wire Gage
FFT	Fast Fourier Transform

Symbols

z	Axial direction
y	Radial direction in Cartesian coordinates
x	Direction perpendicular to z and y
$\vec{B}$	Magnetic field vector
B_z	Axial magnetic field
B_y	Magnetic field in y-direction
B_0	Magnetic field amplitude
σ	Conductivity
λ	Wavelength
v_p	Phase velocity
v_r	Relative velocity
u	Plasma velocity
$\vec{E}$	Electric field vector
E_z	Axial electric field
E_y	Electric field in y-direction
E_x	Electric field in x-direction
$\vec{f}$	Force vector
f_z	Axial force
f_y	Radial force
t	Time
L'	Inductance per unit length
C'	Capacitance per unit length
f	Frequency
$\vec{j}$	Current vector
R	Resistance
L	Inductance
C	Capacitance
Z_0	Characteristic impedance
ζ	Damping coefficient
V_ch	Charging voltage
f_rep	Repetition frequency
η_d	Dynamical efficiency
T	Kinetic energy
W	Work
$\dot{m}$	Propellant mass flow rate
u_f	Final plasma velocity
u_i	Initial plasma velocity

τ	Time interval of quasi-steady operation
B_r	Radial magnetic field
E_θ	Azimuthal electric field
I	Current
r	Radial direction in cylindrical coordinates
a	Coil Radius
K	Complete elliptic integral of first order
E	Complete elliptic integral of second order
k^2	Argument of elliptic integrals
B_θ	Azimuthal magnetic field
$\vec{v}$	Velocity vector
q	Particle charge
m	Charged particle mass
θ	Azimuthal direction in cylindrical coordinates
r_L	Larmor radius
$v_\perp$	Velocity perpendicular to the magnetic field
ω_c	Cyclotron frequency
v_z	Axial velocity
v_y	Velocity in y-direction
v_x	Velocity in x-direction
V_n	Voltage of the n segment of a transmission line
V_{n+1}	Voltage of the $n+1$ segment of a transmission line
I_n	Current of the n segment of a transmission line
I_{n+1}	Current of the $n-1$ segment of a transmission line
Γ_L	Reflection coefficient
$\Delta\phi$	Current phase variation
N_L	Number of inductors
I_p	Current in primary circuit
I_s	Current in secondary circuit
n	Number of turns in Pearson probe
l	Mean path in Pearson probe
A	Effective area of Pearson probe core
K_1, K_2	Calibration constants of B-dot probes

Constants

μ_0 Vacuum magnetic permeability

Bibliography

[1] Oleg V Batishchev. Minihelicon plasma thruster. *Plasma Science, IEEE Transactions on*, 37(8):1563–1571, 2009.

[2] Brian E Beal and Alec D Gallimore. Energy analysis of a hall thruster cluster. *Ann Arbor*, 1001:48109, 2003.

[3] JW Berkery and EY Choueiri. Characterization of current sheet evolution in a pulsed electromagnetic accelerator. In *28th International Electric Propulsion Conference, Toulouse, France*, 2003.

[4] David Biggs, Sam Avery, Luke Raymond, Wei Liang, Nicolas Gascon, Andrea Lucca Fabris, Juan Rivas-Davila, and Mark A. Cappelli. A compact helicon thruster for cubesat applications. *Proceedings of the 34th International Electric Propulsion Conference. IEPC-2013-b-244.*, 2015.

[5] Jeremiah J Boerner. *Computational simulation of Faraday probe measurements*. ProQuest, 2008.

[6] OV Braginskii, AN Vasil'eva, and AS Kovalev. Helicon plasma source. *Russian Microelectronics*, 31(6):341–345, 2002.

[7] Jerome J Brainerd and Al Reisz. Electrodeless experimental thruster. In *SPACE, PROPULSION & ENERGY SCIENCES INTERNATIONAL FORUM: SPESIF-2009*, volume 1103, pages 126–132. AIP Publishing, 2009.

[8] D Gregory Chavers, Chris Dobson, Jonathan Jones, Michael Lee, Adam Martin, Judith Gregory, Jim Cecil, Roger D Bengtson, Boris Breizman, Alexey Arefiev, et al. Status of magnetic nozzle and plasma detachment experiment. In *SPACE TECH. & APPLIC. INT. FORUM-STAIF 2006: 10th Conf Thermophys Applic Microgravity; 23rd Symp Space Nucl Pwr*

& Propulsion; 4th Conf Human/Robotic Tech & Nat'l Vision for Space Explor.; 4th Symp Space Coloniz.; 3rd Symp on New Frontiers & Future Concepts, volume 813, pages 465–473. AIP Publishing, 2006.

[9] Francis F Chen. Experiments on helicon plasma sources. *Journal of Vacuum Science & Technology A*, 10(4):1389–1401, 1992.

[10] Francis F Chen. Helicon plasma sources. *High Density Plasma Sources*, pages 1–75, 1995.

[11] Francis F Chen and Rod W Boswell. Helicons-the past decade. *Plasma Science, IEEE Transactions on*, 25(6):1245–1257, 1997.

[12] Francis F Chen and Schweickhard E Von Goeler. Introduction to plasma physics and controlled fusion volume 1: Plasma physics. *Physics Today*, 38(5):20, 2008.

[13] Edgar Choueiri, Thomas Markusic, John Berkery, and James Cooley. Physics and dynamics of current sheets in pulsed plasma thrusters. Technical report, DTIC Document, 2002.

[14] Edgar Y Choueiri and Kurt A Polzin. Faraday acceleration with radio-frequency assisted discharge. *Journal of propulsion and power*, 22(3):611–619, 2006.

[15] EE Covert, CW Haldeman, and JP Sullivan. A variable phase velocity traveling wave pump. *AIAA Journal*, 9(7):1389–1395, 1971.

[16] Cree, Inc. *Silicon Carbide Power MOSFET C2M MOSFET Technology*, 2014. Rev. A.

[17] FR Chang Díaz, JP Squire, AV Ilin, GE McCaskill, TX Nguyen, DS Winter, AJ Petro, GW Goebel, L Cassady, KA Stokke, et al. Development of the vasimr^{TM} engine, the. In *International Conference of Electromagnetics in Advanced Space Applications*, 1999.

[18] Mircea Dulau and Laszlo David. Modeling and simulation of electron's trajectory inside of electron beam gun. *Journal of Control Engineering and Applied Informatics*, 9(1):27–32, 2007.

[19] G Emsellem. Electrodeless plasma thruster design characteristics and performances. In *4th International Spacecraft Propulsion Conference*, volume 555, page 124, 2004.

[20] CL Enloe. High-resolution retarding potential analyzer. *Review of scientific instruments*, 65(2):507–508, 1994.

[21] FC Fehsenfeld, KM Evenson, and HPa Broida. Microwave discharge cavities operating at 2450 mhz. *Review of scientific Instruments*, 36(3):294–298, 1965.

[22] N Gascon, M Dudeck, and S Barral. Wall material effects in stationary plasma thrusters. i. parametric studies of an spt-100. *Physics of Plasmas (1994-present)*, 10(10):4123–4136, 2003.

[23] L Heflinger, S Ridgway, and A Schaffer. Transverse traveling wave plasma engine. *AIAA Journal*, 3(6):1028–1033, 1965.

[24] Richard R Hofer, Mitchell LR Walker, and Alec D Gallimore. A comparison of nude and collimated faraday probes for use with hall thrusters. In *27th International Electric Propulsion Conference*, pages 15–19, 2001.

[25] W Andrew Hoskins, AJ Kelly, and RG Jahn. Asymmetric discharge patterns in the mpd thruster. In *AIAA, DGLR, and JSASS, International Electric Propulsion Conference, 21 st, Orlando, FL*, page 1990, 1990.

[26] Ivana Hrbud, Michael LaPointe, Robert Vondra, Ralph Lovberg, C Lee Dailey, and Charles Schafer. Status of pulsed inductive thruster research. 2002.

[27] Robert G Jahn. *Physics of electric propulsion*. Courier Corporation, 2012.

[28] RE Jones and RW Palmer. Experimental investigation of a variable-length constant-velocity traveling magnetic wave plasma accelerator. 1967.

[29] Glenn C Light. Magnetic insulation experiments with a traveling magnetic piston plasma accelerator. Technical report, DTIC Document, 1963.

[30] RH Lovberg and CL Dailey. Large inductive thruster performance measurement. *AIAA Journal*, 20(7):971–977, 1982.

[31] Andrea Lucca Fabris and Mark A. Cappelli. Traveling magnetic field plasma accelerator. *Proceedings of the 33rd International Electric Propulsion Conference. IEPC-2013-086.*, 2013.

[32] Thomas Edward Markusic. *Current sheet canting in pulsed electromagnetic accelerators.* 2002.

[33] Daniel Martinez and Eduardo Ahedo. Plasma-wave interaction in a helicon thruster. *Proceedings of the 32nd International Electric Propulsion Conference. IEPC-2011-047.*, 2011.

[34] Lucas A Morton. *Calibration of a Magnetic Field Probe as a Diagnostic for Laser-Produced Plasma.* PhD thesis, University of California, Los Angeles, 2010.

[35] Ryosuke Nomura, Naofumi Ohnishi, and Hiroyuki Nishida. Pic simulation of electrodeless plasma thruster with rotating electric field. In *28TH INTERNATIONAL SYMPOSIUM ON RAREFIED GAS DYNAMICS 2012*, volume 1501, pages 1431–1436. AIP Publishing, 2012.

[36] RA Pahl, Joshua L Rovey, and David J Pommerenke. Calibration of magnetic field probes at relevant magnitudes. In *Pulsed Power Conference (PPC), 2013 19th IEEE*, pages 1–6. IEEE, 2013.

[37] AS Penfold, GR Seemann, and JA Thornton. Experimental study of a traveling-wave accelerator. *AIAA Journal*, 4(10):1870–1872, 1966.

[38] R Piejak, V Godyak, and B Alexandrovich. The electric field and current density in a low-pressure inductive discharge measured with different b-dot probes. *Journal of applied physics*, 81(8):3416–3421, 1997.

[39] CA Romero-Talamás, PM Bellan, and SC Hsu. Multielement magnetic probe using commercial chip inductors. *Review of scientific instruments*, 75(8):2664–2667, 2004.

[40] Jerry L Ross. *Probe studies of a Hall thruster at low voltages.* PhD thesis, Michigan Technological University, 2011.

[41] Joshua L Rovey, Mitchell LR Walker, Alec D Gallimore, and Peter Y Peterson. Magnetically filtered faraday probe for measuring the ion current density profile of a hall thruster. *Review of Scientific Instruments*, 77(1):013503, 2006.

[42] James C Simpson, John E Lane, Christopher D Immer, and Robert C Youngquist. Simple analytic expressions for the magnetic field of a circular current loop. 2001.

[43] Emmanuelle Sommier, Michelle K Scharfe, Nicolas Gascon, Mark A Cappelli, and Eduardo Fernandez. Simulating plasma-induced hall thruster wall erosion with a two-dimensional hybrid model. *Plasma Science, IEEE Transactions on*, 35(5):1379–1387, 2007.

[44] JP Squire, FR Chang-Díaz, VT Jacobson, GE McCaskill, RD Bengtson, and RH Goulding. Helicon plasma injector and ion cyclotron acceleration development in the vasimr experiment. In *36th AIAA/AS-ME/SAE/ASEE Joint Propulsion Conference Proceedings*, pages 17–19, 2000.

[45] RN Szente, RJ Munz, and MG Drouet. Electrode erosion in plasma torches. *Plasma chemistry and plasma processing*, 12(3):327–343, 1992.

[46] Chris Waters. Current transformers provide accurate, isolated measurements. *Power conversion & intelligent motion*, (12), 1986.

[47] TE Weber, JT Slough, and D Kirtley. The electrodeless lorentz force (elf) thruster experimental facility. *Review of Scientific Instruments*, 83(11):113509, 2012.

Appendix A

Experimental Setup for the Development of a Traveling Magnetic Field Plasma Accelerator

Paper presented during the poster session of the 34th International Electric Propulsion Conference (Hyogo-Kobe, Japan, July 4-10, 2015).

Experimental Setup for the Development of a Traveling Magnetic Field Plasma Accelerator

IEPC-2015-442/ISTS-2015-b-442

Simone Feraboli,[*] Andrea Lucca Fabris[†] and Mark A. Cappelli[‡]
Stanford University, Stanford, CA, 94305, USA

This paper describes the experimental setup developed to study a traveling magnetic field plasma accelerator. This system represents the second stage of a dual-stage electrodeless propulsion system in which the plasma produced by a primary ionization source is accelerated by means of a traveling magnetic field. Previous 1D Particle-In-Cell simulations showed that the electron dynamics is directly affected by the propagating magnetic field; under certain conditions this interaction generates a space charge and an electric field at the magnetic front that accelerates ions. A proof-of-concept system has been designed and built based on an array of time-delayed pulsed discharges to produce the traveling magnetic field and it has been tested coupled with independent helicon or microwave plasma sources. The experimental setup includes current probes, magnetic field probes and a time-of-flight probe in order to capture possible plasma-traveling magnetic field interactions.

Nomenclature

PIT	=	Pulsed Inductive Thruster
I_{sp}	=	Specific impulse
$MOSFET$	=	Metal Oxide Semiconductor Field Effect Transistor
z	=	Axial Direction
DC	=	Direct Current
f	=	Frequency
R	=	Resistance
L	=	Inductance
C	=	Capacitance
ζ	=	Damping Coefficient
RF	=	Radio Frequency

---

[*]Visiting Student Researcher, Mechanical Engineering Department, simonef@stanford.edu.
[†]Postdoctoral Research Fellow, Mechanical Engineering Department, lfandrea@stanford.edu.
[‡]Professor, Mechanical Engineering Department, cap@stanford.edu.

I. Introduction

Iɴ standard electric propulsion systems one of the main lifetime-limiting process originates from the erosion of the acceleration grids or electrodes, whose surfaces are exposed to energetic particles and are subject to high temperature conditions. For this reason, a lot of emphasis has been put in developing electrodeless propulsion systems. Not relying on electrodes to accelerate the propellant can boost significantly the lifetime of a thruster; an added bonus to this technology is the neutrality of the exhaust flow, which avoids the use of an additional neutralizer.

An example of an electrodeless thruster is the PIT.[2] It mainly consists of a flat spiral coil, with a pulsed current flowing through it; the current is typically generated by discharging a bank of capacitors. Gas is injected in the thruster in pulses synchronized with the current pulses through the coil. The increasing current generates a strong azimuthal electric field that ionizes the gas and induces an azimuthal current in the plasma itself. The current in the plasma and that one in the coil flow in opposite directions, creating a repulsive force that blows the plasma out of the thruster. I_{sp} over 2000 s and efficiencies around 50% have been obtained.

Other alternative solutions have been proposed, such as an electrodeless thruster based on a rotating electric field.[3] In this case the superposition of a rotating electric field and a magnetic field (both axial and radial) is exploited to accelerate the propellant. The plasma produced in a source stage is injected into the thruster and gets an induced rotational motion due to the applied rotating electric field and axial magnetic field; this rotating motion generates an azimuthal current in the plasma, which interacts with the radial component of the magnetic field to push the propellant flow downstream.

Another proposed concept is an electrodeless thruster based on an axially traveling magnetic field.[1,4,5,6,7] This technology is typically arranged in a dual-stage configuration in which a traveling magnetic field accelerates the plasma generated by a primary ionization source. However, in some studies the electric field associated to the time-varying magnetic field was strong enough to ionize the neutral propellant, embedding ionization and acceleration in a single stage. The acceleration mechanism has been previously investigated implementing a particle-in-cell model.[1] The simulations highlight the role of electrons as carriers of the acceleration; indeed the traveling magnetic field directly acts on electron dynamics creating a space charge at the magnetic front and inducing an electric field which accelerates also the ions (indirect effect on the ion dynamics). The typical hardware configuration is made of coils with phase shifted currents to generate a magnetic field that propagates downstream in the axial direction. Multiple studies were carried out in the '60s and '70s about accelerating plasma with a propagating magnetic field and demonstrated the effectiveness of the acceleration concept. Most studies however relied on huge amounts of power to produce a high enough level of current in the coils to generate a strong magnetic field in the accelerator channel.

The goal of this work is to design a traveling magnetic field accelerator that operates in the low power range. A design guideline is the limitation of wall losses increasing the aspect ratio diameter/length of the accelerator cylindrical channel in comparison with previous prototypes[1]. The accelerator is based on time-delayed capacitor discharges in RLC circuits which are able to produce a traveling magnetic field with velocities up to 30,000 m/s and strengths up to 150 G. The developed system is able to work in constant velocity mode or can provide an increase of the traveling velocity along the accelerator channel.

II. Paper Outline

This paper is organized as follows. First, a general description of the setup is presented along with the key parameters of the system and its operational features. Then, after a brief description of the diagnostics, we present and discuss some preliminary results obtained in different configurations, and we conclude with ideas that could be applied in the future to carry on and improve the work.

III. Accelerator Characteristics

The accelerator has been designed and built for pulsed mode operation. It consists of 7 independent RLC circuits that generate time-delayed current pulses to achieve an overall traveling magnetic pulse; the internal diameter of the accelerator is 2.5 cm and the total length is 3.5 cm. Each coil is made of 4 windings of 2 mm diameter copper wire arranged in 2 layers with 2 turns each, with an inductance of 0.6 µH. The current pulses are produced by discharging two 22 nF capacitors in parallel, equivalent to 44 nF for each

circuit. To damp the oscillations and produce a single current pulse, a 5 Ω resistor has been introduced in series to the other components. These parameters have been selected following a design phase based on the classical equations describing the physics of RLC circuits. In particular:

$$2\pi f = \frac{1}{\sqrt{LC}} \tag{1}$$

$$\zeta = \frac{R}{2}\sqrt{\frac{C}{L}} = 4\pi f L \tag{2}$$

where f is the natural oscillation frequency and ζ the damping coefficient. The design phase includes a trade-off analysis to satisfy the requirements on: 1) magnetic field strength; 2) traveling velocity range; 3) pulse width; 4) accelerator channel geometry (in terms of aspect ratio); 5) energy/pulse ratio and repetition rate of the pulses (giving the power consumption). Such a process has been carried out with the support of Matlab and Simulink models. The developed single circuits present a natural frequency of 1 MHz and a damping coefficient $\zeta = 0.83$.

MOSFETs have been embedded in the circuits to control the charge and discharge of the capacitors, whereas solid state relays are used to open and close the connection between the capacitors and the power supply. A simple schematic of a circuit is represented in Fig. 1a, while Fig. 1b shows the arrangement of the components within the circuit.
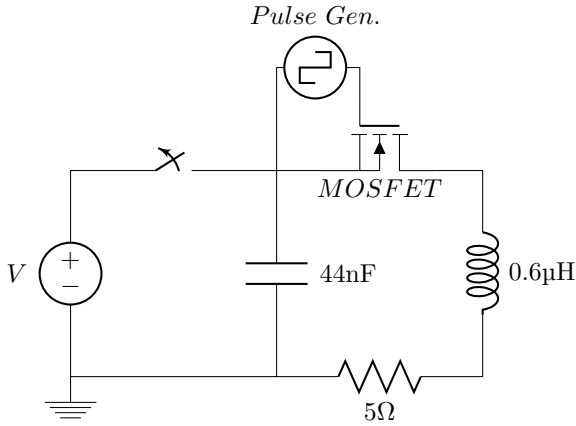
(a) Single circuit schematic.
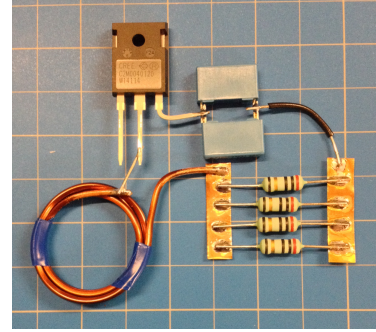
(b) Picture of a single circuit.

A. Pulsed Mode Operation

The capacitors are charged by a 10 mA high voltage DC power supply at a maximum voltage of 800 V, giving a pulse energy of 0.014 J for single circuit or 0.098 J overall; a power level of 9.8 W is obtained at a repetition rate of 100 Hz. Solid state relays are incorporated between the power supply and the capacitors and are controlled by a Stanford Research System DG535 pulse generator (A) which opens and closes the line at a set frequency (i.e. the traveling magnetic pulse repetition frequency). The same pulse generator triggers two additional pulse generators (B and C) which operate the MOSFETs, allowing to close the RLC circuits only when the power supply has been disconnected; this operational sequence is needed to avoid any influence of the power supply on the current pulses generated by discharging the capacitors through the coils. Each pulse generator (B and C) may pilot up to four MOSFETs, closing each circuit at the proper time-delay from the trigger. The velocity of the traveling magnetic pulse is directly dependent on the time delay between the activations of the MOSFETs embedded in two consecutive circuits; the possibility to set the time-delays on the pulse generators allows a flexible determination of the magnetic field propagating velocity. The upper boundary for the velocity is 30,000 m/s, however the accelerator has been operated mostly at a magnetic pulse velocity of about 13,000 m/s, with some tests done at different velocities ranging from 5,000 m/s to 25,000 m/s. The tests have been conducted at different repetition rates, however we mainly operate at 5 Hz in order to allow the power supply to fully charge the capacitors before discharging them. Two different primary ionization stages have been employed in the experiments: one is a helicon

source, continuously operated in a power range from 3 to 35 W on argon; the second source is a 2.45 GHz Evanson microwave cavity operated at 40 W, again on argon. The system consists of a quartz tube with two expansion regions: the tube diameter presents two step-changes from 1.25 cm to 2.5 cm and from 2.5 cm to 5 cm. The plasma sources require a diameter of 1.25 cm, the accelerator is located around the 2.5 cm region, and finally the tube is connected to the vacuum chamber through a 5 cm port. The tube is mounted outside the vacuum chamber, with the accelerator placed about 2 cm after the first expansion. The vacuum chamber is a 0.6 m diameter, 1.2 m length stainless steel chamber, pumped down to a base pressure level of 10^{-6} Torr when any mass flow is not injected, or $10^{-4} - 10^{-5}$ Torr during the thruster operation; these pressure levels are achieved by a single 50 cm diameter cryopump; the initial rough vacuum is obtained through a mechanical pump and a blower. Pictures of the setup are presented in Fig. 3.
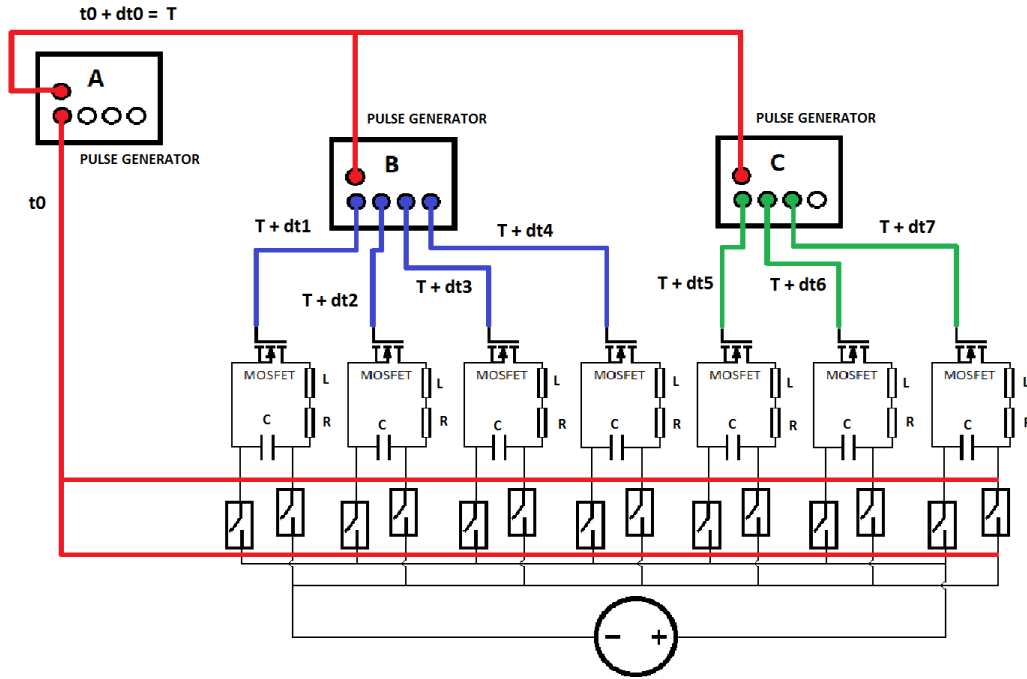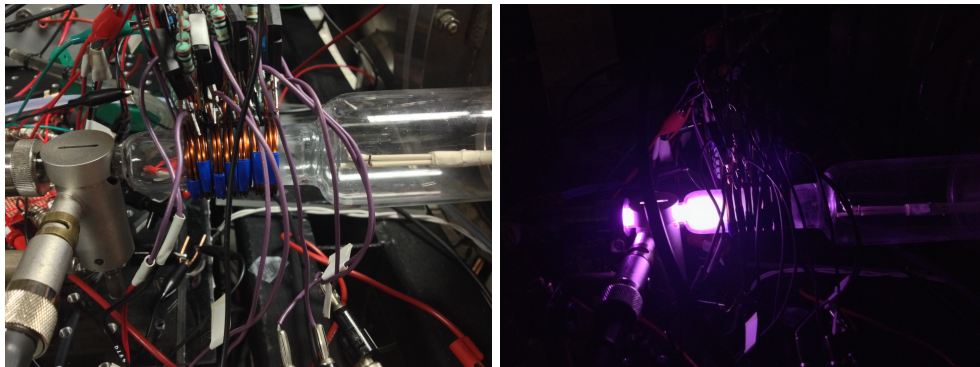

Figure 2: Simplified system schematic.

Figure 3: Pictures of the setup with the microwave plasma source.

B. Diagnostics

In order to determine the presence of a traveling magnetic pulse within the accelerator, two B-dot probes have been built. Each one consists of a single layer of 30 turns of 32 AWG wire, with an inner diameter of 1.2 mm; both have been calibrated with the uniform magnetic field of a solenoid, applying a similar approach as that presented in Ref. 8. The two probes have been placed at a known distance inside the accelerator channel in absence of plasma; the magnetic pulse velocity is then calculated by determining the time delay between the peaks measured by the two probes. Finally, time-resolved measurements of the magnetic field at multiple distances (every 3 mm along the length of the accelerator) allow the reconstruction of the magnetic field spatial evolution.

Pearson probes have been used to measure the current flowing through the first and last circuits to check the coherence of the time delays with the settings on the pulse generators; all circuits have also been tested before and after the assembly in the final array to verify their capability of generating the expected current pulses.

A time-of-flight probe has been used in order to detect any interaction between the traveling magnetic pulse and the plasma. The probe consists of two copper conductors placed 1.46 cm apart; the purpose is estimating the velocity of the plasma flow simply by detecting the time delay of the current peaks at the conductors spaced by a known distance. The probe includes also a third conductor shielded from the plasma flow by means of a ceramic case in order to detect whether the signals produced by the unshielded conductors come from a real interaction with the plasma sheet or just from electromagnetic interference. Measurements have been performed at different time scales, in order to detect both the effect of a single burst and the effect of multiple magnetic pulses discharged at the set frequency. The effect of different voltage levels (i.e. of the energy per pulse in each single circuit) has been also explored.

IV. Preliminary Experimental Investigation

The first measured parameter has been the current through the coils in order to verify its agreement, both in terms of intensity and pulse width, with the design profile and the capability of the system to properly time-delay subsequent pulses. The results obtained from these measurements have been used as input parameters for numerical simulations of the magnetic field produced within the accelerator; we have then compared the measured values of the field with the simulated ones to demonstrate the agreement between the predicted magnetic field and that generated by the experimental setup.
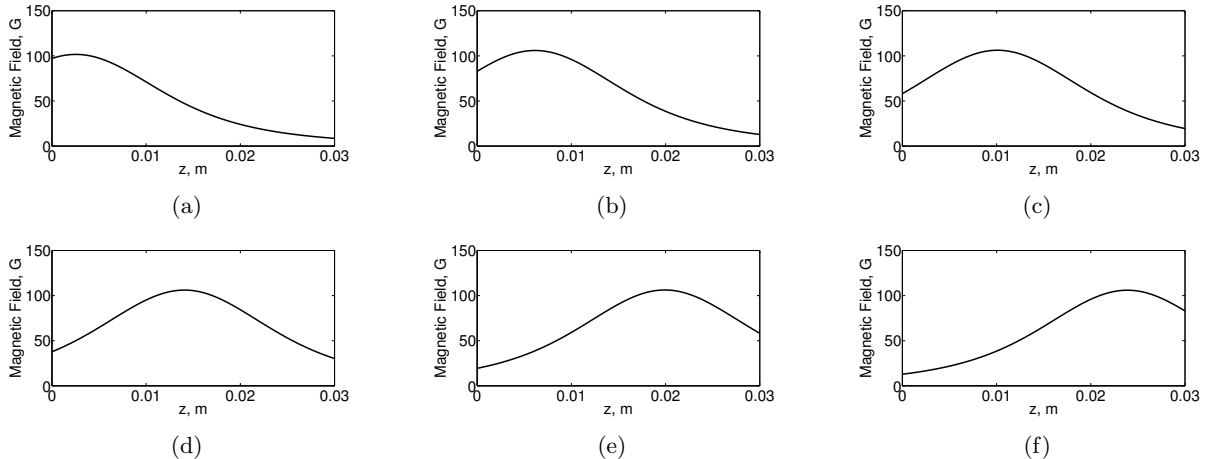
Figure 4: 1D magnetic field simulation at different time instants: a) t_0 µs, b) $t_0 + 0.5$ µs, c) $t_0 + 1$ µs, d) $t_0 + 1.5$ µs, e) $t_0 + 2.2$ µs, f) $t_0 + 2.5$ µs.

The following step involves capturing the time-evolution of the magnetic field at ten different locations inside the accelerator; this set of measurements provides enough resolution to reconstruct the spatial distribution of the magnetic field at different times. Fig. 4 and 5 show the measured field is in agreement with that obtained through the numerical simulations. The measurements demonstrate the accelerator effectively
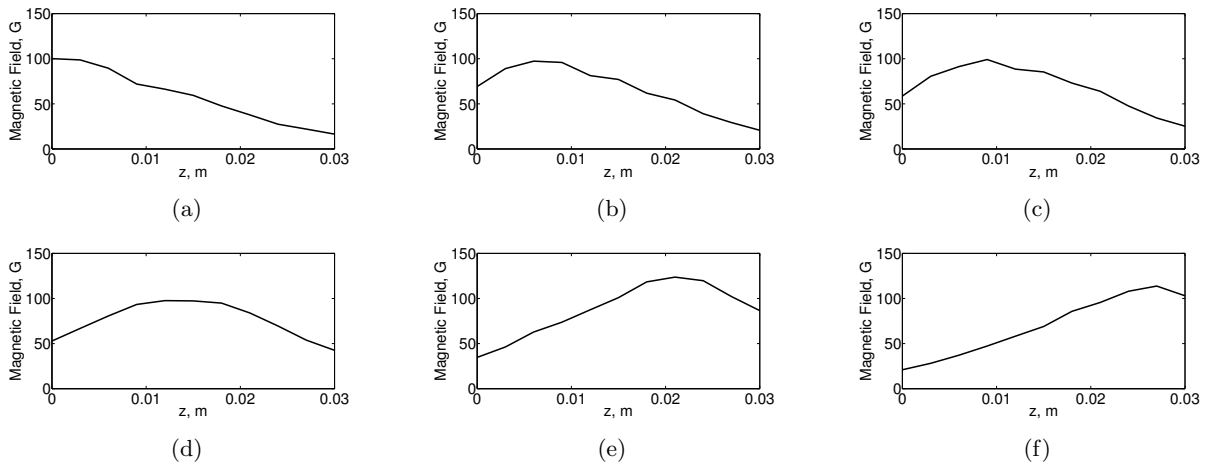
Figure 5: 1D magnetic field measurement at different time instants: a) t_0, b) $t_0 + 1.3$ µs, c) $t_0 + 1.5$ µs, d) $t_0 + 1.9$ µs, e) $t_0 + 2.5$ µs, f) $t_0 + 2.9$ µs.

produces a magnetic pulse traveling along its length.

Additional tests have been performed to verify the coherence of the generated magnetic field velocity with the settings of the accelerator; we have tested different velocities (see Fig. 6) and we have determined that the measured velocities differ from the theoretical ones by less than 11%, an acceptable discrepancy for our purposes which has roots in the errors on the position of the magnetic probe as well as some fluctuations of the delay between two consecutive current pulses.
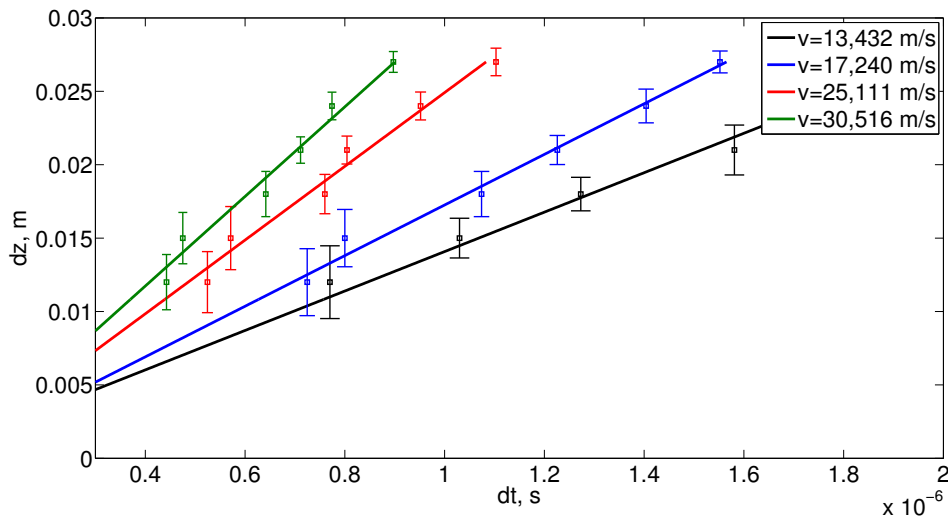
Figure 6: Magnetic field at different velocities.

After all these tests were conducted in absence of plasma, the investigation then focused on the interaction between the generated magnetic field and a plasma flow. Time-of-flight probe measurements have been carried out in various configurations and data have been collected with both the plasma and the accelerator operating, only the plasma operating, and only the accelerator operating. This procedure is aimed to isolate the signal generated by plasma-field interactions from electromagnetic noise. In particular, we aim to: 1) detect a plasma-field interaction, 2) discriminate the signal originated by a propagating plasma sheet from electromagentic noise, 3) understand the nature of the plasma field interaction (if present) seeking evidence of a "magnetic piston" effect.

During the tests, an effect of the pulsed magnetic field can be witnessed visually by looking at the plasma flow, which appears pulsating as soon as the accelerator is turned on, whereas it appears quiescent when the accelerator is not operating. After capturing a video of the experiment, we have analyzed the different frames and indeed we can observe bursts of more intense plasma synchronized with the repetition rate of the discharges in the accelerator (in the case of Fig. 7 the repetition rate is 5 Hz).

(a)

(b)

(c)

(d)

(e)

(f)
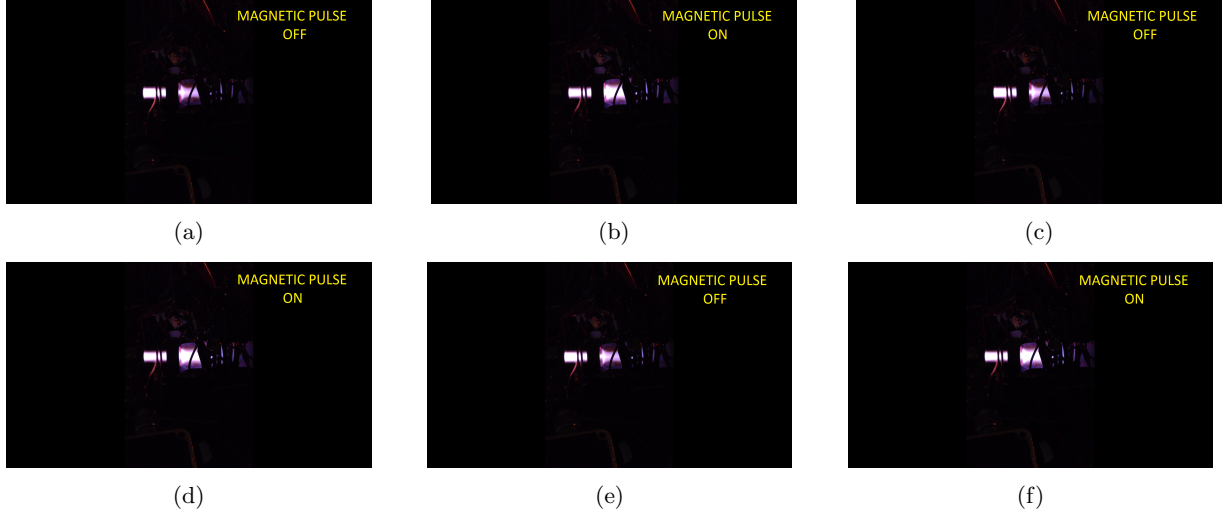
Figure 7: Magnetic field at different time instants: a) t_0, b) $t_0 + 0.1$ s, c) $t_0 + 0.2$ s, d) $t_0 + 0.3$ s, e) $t_0 + 0.4$ s, f) $t_0 + 0.5$ s.

Fig. 8 and 9 illustrate the time-of-flight traces using the helicon source and the microwave cavity as the primary ionization stage, respectively. The time-of-flight probe is located inside the quartz tube, at a distance of about 4 cm from the end of the accelerator. From the collected data we can outline some key aspects: although some electromagnetic interference is present (the signal without plasma shows such phenomenon), it is much weaker than the signal obtained with plasma operating. As expected, the electromagnetic interference produced by the accelerator in absence of plasma is observed by all the electrodes, including the encased one. Its intensity decreases as the distance from the accelerator end increases, independently by the electrode being encased or exposed. On the other hand, when the plasma is injected, the strength of the peaks observed by the uncovered electrodes is much stronger in comparison with that detected by the encased electrode. This observation suggests that such an effect is not merely an increase of the electromagnetic interference due to the plasma-circuit coupling, but there is an overlapping plasma contribution. Moreover, the analysis of the time-of-flight profiles under certain operating conditions highlights the presence of multiple peaks on the exposed electrodes traces that are completely absent on the encased electrode trace (Fig. 8). Also, recall that these effects take place only when the plasma source is operating. These characteristics demonstrate an interaction of the traveling magnetic field with the plasma, however the observed multiple features and the measured delay-times between peaks are unexpected and in contrast with the theoretical predictions; as a consequence, the experimental results do not allow to provide a final assessment on the nature of the interaction, that may not be an effective magnetic piston (an alternative mechanism may be a fluctuation in the plasma source induced by the magnetic pulse). Additional experiments with different probes and different operating conditions (energy/pulse, propellant mass, plasma sources with enhanced ionization), along with theoretical studies, are needed to demonstrate the proposed acceleration concept.

V.   Conclusions and Future Work

In this paper we present the development of a compact, low power traveling magnetic field accelerator. The system is intended to be used as the plasma accelerator in a dual stage electrodeless propulsion system to accelerate the plasma produced by a primary ionization source. We show the results of the design phase and how the performance of the built system is in agreement with that simulated. In particular, the developed system is able to satisfy the design requirements in terms of: magnetic field strength, magnetic pulse width

(a)

(b)

(c)
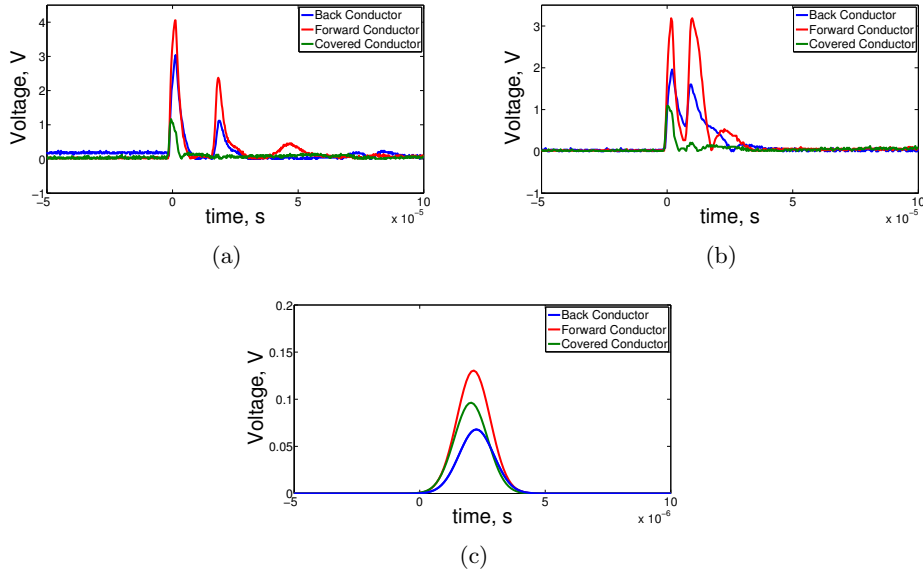
Figure 8: Time-of-flight probe data using the helicon source as the primary ionization stage: a) 0.05 mTorr 10 W, b) 0.05 mTorr 15 W, c) no plasma.

(a)

(b)

(c)
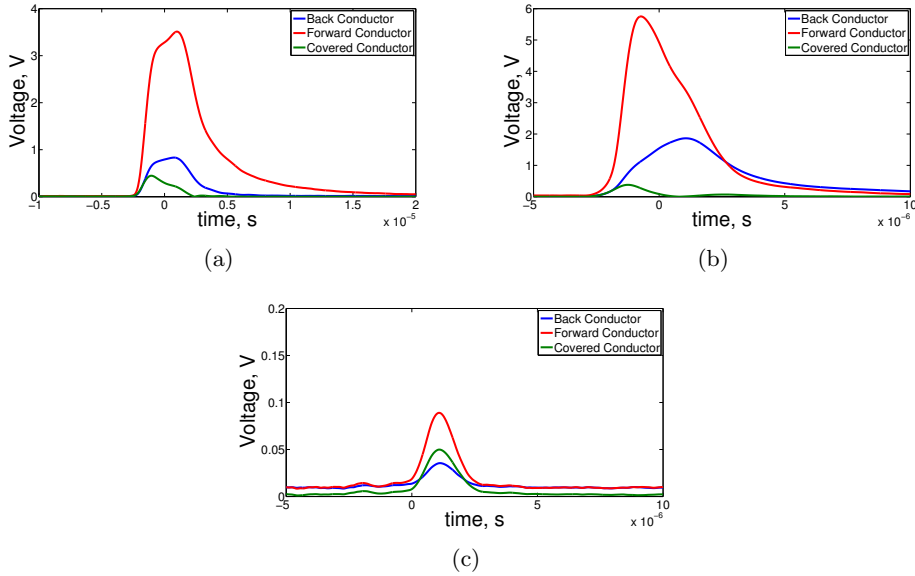
Figure 9: Time-of-flight probe data using the microwave source as the primary ionization stage: a) 0.2 mTorr 30W, b) 0.4 mTorr 10W, c) no plasma.

and traveling velocity, geometry (in terms of system aspect ratio), power consumption. The system consists of an array of coils with progressively delayed currents to generate an axially-propagating pulsed magnetic field. Current probes and B-dot probes are used to characterized the time and space evolution of the magnetic field profile at different propagating velocities.

We have started a preliminary experimental campaign, aiming to detect an interaction between the accelerator and a plasma flow. A microwave source or a helicon source are used as the primary ionization stage. We observe an interaction between the generated pulsed magnetic field and the plasma, however the collected measurements do not allow to asses such interaction is the result of a magnetic piston effect.

Future investigations will explore different operating conditions, different primary ionization stages and the use of different diagnostics systems (magnetic probes inside the plasma flow, energy analyzers, Faraday probe).

References

[1] Lucca Fabris, A., and Cappelli, M. A.,"Traveling Magnetic Field Plasma Accelerator," Proceedings of the 33rd International Electric Propulsion Conference, Washington, D.C., USA, October 6-10, 2013, IEPC-2013-86.

[2] Hrbud, I., LaPointe, M., Vondra, R., Dailey, C. L., and Lovberg, R., "Status Of Pulsed Inductive Thruster Research," Space Technology and Applications International Forum, 2002.

[3] Nomura, R., Ohnishi, N., Vondra, R., and Nishida, H., "PIC Simulation of Electrodeless Plasma Thruster with Rotating Electric Field," 28th International Symposium on Rarefied Gas Dynamics, 2012.

[4] Seeman, G. R., Thornton, J. A., and Penfold, A. S., "Experimental Study of a Traveling- Wave Accelerator," AIAA Journal, Vol. 4, No. 1,Oct. 1966, pp. 1870-1872.

[5] Palmer, R. W., and Jones, R. E., "Experimental Investigation of a Variable-Length Constant-Velocity Traveling Magnetic Wave Plasma Accelerator," NASA TN D-4205, Oct. 1967.

[6] Heflinger, L., Ridgway, S., and Schaffer, A., "Transverse Traveling Wave Plasma Engine," AIAA Journal, Vol. 3, No. 6,Jun. 1965, pp. 1028-1033.

[7] Haldeman, C. W., Sullivan, J. P., and Covert, E. E., "A Variable Phase Velocity Traveling Wave Pump," AIAA Journal, Vol. 9, No. 7,Jul. 1971, pp. 1389-1395.

[8] Hoskins, W. A., "Asymmertic Discharge Patterns in the MPD Thruster," M.Sc. Thesis,Department of Mechanical and Aerospace Engineering, Princeton Univ., Princeton, NJ, 1990.

Appendix B

The Matlab code developed to simulate the traveling magnetic field, the induced electric field, and the motion of charged particles in the accelerator are presented.

Magnetic Field Code

```matlab
function [Brc,Bth,Bz] = magnetic_field_current_loop(r,z
    ,r_p,z_p,a,I0)

Bz=zeros(size(z));
Brc=zeros(size(z));


global u0 %permeability of free space is a global
    variable

for pp=1:length(z_p)

    rc=sqrt((r-r_p).^2);
    m=(4.*a.*rc).*(((rc+a).^2)+((z-z_p(pp)).^2)).^(-1);
        %This is a parameter for calculating the
        Elliptical integrals
    [K,E] = ellipke(m);

    kofkc=K;
    eofkc=E;

```

```
18        Brc_p=(u0.*I0./(2.*pi.*rc)).*(z-z_p(pp)).*(((rc+a)
              .^2)+((z-z_p(pp)).^2)).^(-.5)).*(-kofkc+eofkc
              .*((rc.^2+a.^2+(z-z_p(pp)).^2)./(((rc-a).^2)+((z
              -z_p(pp)).^2)))); %radial component of B%
19        Bz_p=(u0.*I0./(2.*pi)).*((((rc+a).^2)+((z-z_p(pp))
              .^2)).^(-.5)).*(kofkc-eofkc.*((rc.^2-a.^2+(z-z_p
              (pp)).^2)./(((rc-a).^2)+((z-z_p(pp)).^2)))); %
              axial component of B
20
21        Brc_p(isnan(Bz_p)) = 0 ;
22        Bz_p(isnan(Bz_p)) = 0 ;
23
24        Bz=Bz+Bz_p*2;
25        Brc=Brc+Brc_p*2;
26
27    end
28
29    Bth=zeros(size(z));
30
31    end
```

Electric Field Code

```
1  function [Er,Ethn,Ez] = electric_field(r,z,dt,dr,Bzin,
       Bzn)
2
3  global v_phase
4  global L
5
6  Bzo=Bzin;
7
8  dB=(Bzn-Bzo)./dt;
9  dB_dr=2*dr.*dB;
10  for kk=1:size(Bzn,1)
11      for nn=0:(size(Bzn,2)-1)
12          if nn==0
13              Ethn(kk,nn+1)=0;
14          elseif nn==1
15              Ethn(kk,nn+2)=Ethn(kk,nn)-dB_dr(kk,nn)/2;
16          else
17          Ethn(kk,nn+1)=Ethn(kk,nn-1)-dB_dr(kk,nn);
18          Bzo=Bzn;
19          end
20      end
21  end
22
23  Er=zeros(size(z)); % approximation
24  Ez=zeros(size(z)); % approximation
25
26  end
```

ODE Code

```
1  function odef=odefunction(t,y)
2
3  global a
4  global r_p
5  global q
6  global m
7  global dt
8  global dr
9  global r
10 global z
11 global I1
12 global I2
13 global I3
14 global I4
15 global I5
16 global I6
17 global I7
18 global time
19 global z_p1
20 global z_p2
21 global z_p3
22 global z_p4
23 global z_p5
24 global z_p6
25 global z_p7
26
27 It1=interp1(time,I1,t);
28 It2=interp1(time,I2,t);
29 It3=interp1(time,I3,t);
30 It4=interp1(time,I4,t);
31 It5=interp1(time,I5,t);
32 It6=interp1(time,I6,t);
33 It7=interp1(time,I7,t);
34
35 [Brc1,Bth1,Bz1] = magnetic_field_current_loop(r,z,r_p,
      z_p1,a,It1);
36 [Brc2,Bth2,Bz2] = magnetic_field_current_loop(r,z,r_p,
      z_p2,a,It2);
```

114

```
37  [ Brc3 , Bth3 , Bz3 ]  =  m a g n e t i c _ f i e l d _ c u r r e n t _ l o o p ( r , z , r_p ,
        z_p3 , a , I t 3 ) ;
38  [ Brc4 , Bth5 , Bz4 ]  =  m a g n e t i c _ f i e l d _ c u r r e n t _ l o o p ( r , z , r_p ,
        z_p4 , a , I t 4 ) ;
39  [ Brc5 , Bth5 , Bz5 ]  =  m a g n e t i c _ f i e l d _ c u r r e n t _ l o o p ( r , z , r_p ,
        z_p5 , a , I t 5 ) ;
40  [ Brc6 , Bth6 , Bz6 ]  =  m a g n e t i c _ f i e l d _ c u r r e n t _ l o o p ( r , z , r_p ,
        z_p6 , a , I t 6 ) ;
41  [ Brc7 , Bth7 , Bz7 ]  =  m a g n e t i c _ f i e l d _ c u r r e n t _ l o o p ( r , z , r_p ,
        z_p7 , a , I t 7 ) ;
42
43  Brc=2*( Brc1+Brc2+Brc3+Brc4+Brc5+Brc6+Brc7 ) *10^4;
44  Bz=2*( Bz1+Bz2+Bz3+Bz4+Bz5+Bz6+Bz7 ) *10^4;
45
46  Itn1=interp1 ( time , I1 , t+dt ) ;
47  Itn2=interp1 ( time , I2 , t+dt ) ;
48  Itn3=interp1 ( time , I3 , t+dt ) ;
49  Itn4=interp1 ( time , I4 , t+dt ) ;
50  Itn5=interp1 ( time , I5 , t+dt ) ;
51  Itn6=interp1 ( time , I6 , t+dt ) ;
52  Itn7=interp1 ( time , I7 , t+dt ) ;
53
54  [ Brcn1 , Bthn1 , Bzn1 ]  =  m a g n e t i c _ f i e l d _ c u r r e n t _ l o o p ( r , z ,
        r_p , z_p1 , a , I t n 1 ) ;
55  [ Brcn2 , Bthn2 , Bzn2 ]  =  m a g n e t i c _ f i e l d _ c u r r e n t _ l o o p ( r , z ,
        r_p , z_p2 , a , I t n 2 ) ;
56  [ Brcn3 , Bthn3 , Bzn3 ]  =  m a g n e t i c _ f i e l d _ c u r r e n t _ l o o p ( r , z ,
        r_p , z_p3 , a , I t n 3 ) ;
57  [ Brcn4 , Bthn5 , Bzn4 ]  =  m a g n e t i c _ f i e l d _ c u r r e n t _ l o o p ( r , z ,
        r_p , z_p4 , a , I t n 4 ) ;
58  [ Brcn5 , Bthn5 , Bzn5 ]  =  m a g n e t i c _ f i e l d _ c u r r e n t _ l o o p ( r , z ,
        r_p , z_p5 , a , I t n 5 ) ;
59  [ Brcn6 , Bthn6 , Bzn6 ]  =  m a g n e t i c _ f i e l d _ c u r r e n t _ l o o p ( r , z ,
        r_p , z_p6 , a , I t n 6 ) ;
60  [ Brcn7 , Bthn7 , Bzn7 ]  =  m a g n e t i c _ f i e l d _ c u r r e n t _ l o o p ( r , z ,
        r_p , z_p7 , a , I t n 7 ) ;
61
62  Bzn=2*( Bzn1+Bzn2+Bzn3+Bzn4+Bzn5+Bzn6+Bzn7 ) *10^4;
63
64  Bzo=Bz ;
65  [ Er , Eth , Ez ]  =  e l e c t r i c _ f i e l d ( r , z , dt , dr , Bzo , Bzn ) ;
```

```
66
67  B=[interp2(r,z,Brc,y(1),y(3));0;(interp2(r,z,Bz,y(1),y
        (3)))]; % interpolation to get magnetic field at a
        specific point
68  E=[0;interp2(r,z,Eth,y(1),y(3));0]; % interpolation to
        get electric field at a specific point
69
70  odef =  [y(4:6);y(1).*(y(5).^2)+(q/m).*(y(1).*y(5).*B
        (3));(q./(y(1).*m)).*(E(2)+(y(6).*B(1)-y(4).*B(3)))
        -(2./y(1)).*y(4).*y(5);-(q/m).*y(1).*y(5).*B(1)];
71
72  end
```

Particle Trajectory Simulation Code

```matlab
1   clear all
2   clc
3   close all
4
5   global u0
6   global a
7   global r_p
8   global th_p
9   global L
10  global q
11  global m
12  global dt
13  global dr
14  global r
15  global z
16  global I1
17  global I2
18  global I3
19  global I4
20  global I5
21  global I6
22  global I7
23  global time
24  global z_p1
25  global z_p2
26  global z_p3
27  global z_p4
28  global z_p5
29  global z_p6
30  global z_p7
31  [r,z]=meshgrid(linspace(0,0.011,100),linspace
        (0,0.035,100));
32
33  u0=4*pi*1e-7;
34  a=0.0127; %Coil radius in m
35  r_p=0;
36  th_p=0;
37  L=0.035;
```

```matlab
38  q=1.6e-19;
39  %m=9.1e-31; % electron mass
40  m=6.64e-26; %Ar ion mass
41  dr=r(1,2)-r(1,1);
42  time=linspace(0,6e-6,500);
43  dt=1e-12;
44  amplitude=45;
45  width=3e-7;
46  tpeak1=1e-6;
47  tpeak2=1.45e-6;
48  tpeak3=1.9e-6;
49  tpeak4=2.35e-6;
50  tpeak5=2.8e-6;
51  tpeak6=3.25e-6;
52  tpeak7=3.7e-6;
53
54  I1=amplitude*gaussmf(time,[width tpeak1]);
55  I2=amplitude*gaussmf(time,[width tpeak2]);
56  I3=amplitude*gaussmf(time,[width tpeak3]);
57  I4=amplitude*gaussmf(time,[width tpeak4]);
58  I5=amplitude*gaussmf(time,[width tpeak5]);
59  I6=amplitude*gaussmf(time,[width tpeak6]);
60  I7=amplitude*gaussmf(time,[width tpeak7]);
61
62  z_p1=0.00;
63  z_p2=0.005;
64  z_p3=0.01;
65  z_p4=0.015;
66  z_p5=0.02;
67  z_p6=0.025;
68  z_p7=0.03;
69
70  tspan=[0 1e-6];
71
72  r0=[0.001;0.0;0.001]; % initial position [r;theta;z] (m
        )
73  v0=[10;10;9000]; % initial velocity [v_r;v_theta;v_z] (
        m/s)
74  in_cond = [r0;v0];
75
76  [t,y] = ode23(@(t,y) odefunction(t,y),tspan,in_cond);
```

118

```matlab
77
78 % plot particle axial velocity
79 figure(2)
80 plot(t,y(:,6),'k','linewidth',5);
81 set(gca,'FontSize',50)
82 xlhand = get(gca,'xlabel')
83 set(xlhand,'string','Time, s','fontsize',50)
84 ylhand = get(gca,'ylabel')
85 set(ylhand,'string','v_z, m/s','fontsize',50)
86
87 % plot circles delimiting the accelerator edges
88 center=[0 0 0];
89 center2=[0 0 0.035];
90 radius=0.011;
91 angle=0:0.001:2*pi;
92 normal=[0 0 1];
93 v=null(normal);
94 points=repmat(center',1,size(angle,2))+radius*(v(:,1)*
       cos(angle)+v(:,2)*sin(angle));
95 points2=repmat(center2',1,size(angle,2))+radius*(v(:,1)
       *cos(angle)+v(:,2)*sin(angle));
96 figure(1)
97 plot3(points(1,:),points(2,:),points(3,:),'r','
       linewidth',3);
98 hold on
99 plot3(points2(1,:),points2(2,:),points2(3,:),'r','
       linewidth',3);
100 hold on
101
102 % plot particle trajectory
103 plot3(y(:,1).*cos(y(:,2)),y(:,1).*sin(y(:,2)),y(:,3),'k
       ','linewidth',2);
104
105 hold on
106
107 xlabel('x, m')
108 ylabel('y, m')
109 zlabel('z, m')
110
111 set(gca,'FontSize',30)
112 xlhand = get(gca,'xlabel')
```

119

```
113  set(xlhand,'string','x, m','fontsize',30)
114  ylhand = get(gca,'ylabel')
115  set(ylhand,'string','y, m','fontsize',30)
116  zlhand = get(gca,'zlabel')
117  set(zlhand,'string','z, m','fontsize',30)
118
119  view(0,90);
```